EPFL

Thèse n° 10 215

Development of microlens-enhanced SiPMs for a radiation-hard scintillating fibre tracker at LHCb

Présentée le 28 avril 2023

Faculté des sciences de base
Laboratoire de physique des hautes énergies OS
Programme doctoral en physique

pour l'obtention du grade de Docteur ès Sciences

par

Carina TRIPPL

Acceptée sur proposition du jury

Prof. J. H. Dil, président du jury
Prof. O. Schneider, Dr G. Haefeli, directeurs de thèse
Dr B. Leverington, rapporteur
Dr D. Gascón, rapporteur
Dr V. Lamirand, rapporteur

École polytechnique fédérale de Lausanne

2023

Do the best you can until you know better.
Then when you know better, do better.
— Maya Angelou

Acknowledgements

This work would not have been possible without the help of so many people. First of all, I would like to thank my supervisor, Olivier Schneider, for providing me with the possibility to do my PhD at LPHE. I appreciate all the advice and help you have given me during the last four years.

The second thank you goes to my co-supervisor Guido Häfeli. After a somewhat "rocky" start in the first year of my PhD, I believe I am allowed to say that in the end we made it work. You have given me a lot of your time and advice over the last years, and I could not have come this far without your help.

I am also deeply grateful to Stefano Merzi and Alberto Gola. Thank you for the continuous help and support of this project. Giving me the opportunity to learn from you at FBK has really inspired me to continue along this path. Your warm welcome and continued support, even after I returned to EPFL, has been one of my highlights of this PhD. I would also like to thank the whole group for welcoming me into your midsts. I loved our (well mainly yours) daily passionate lunch discussions about food, drinks, TVs and cars.

A big thank you to Frédéric Zanella for the many fruitful discussions and the advice he provided. It was a pleasure working with and learning from you!

Of course I could not have performed a single measurement at LPHE without the help of the electronics and mechanical workshops. I am especially grateful to Alain Pinard, Florian Bernard, Raymond Frei and Nicolas Auberson for their incredible patience with my many (ever changing) requests.

My deepest gratitude goes to Esther and Corinne, who have always been available to help me with any problem I faced. You two are truly the heart and soul of our lab.

Acknowledgements

This work would not have been possible without the constant support of Ettore, Maria Elena and Ana Bárbara. You three have witnessed me at all the different stages of my PhD (either at LPHE or outside), and you were always present with help, advice and a lot of fun. Thank you for everything.

These four years would not have been so enjoyable without my many amazing colleagues. Sara, my partner in crime at LPHE, you have supported me since the day you've arrived, and I could not have hoped to find a better friend. Marie, Surapat (can I call you Arm now?) and Fede, thank you for being the best office mates I could have asked for. You three have always been able to lighten my mood, be it with hilarious jokes, delicious food, the daily chocolate or our discussions about everything and nothing. Thank you Serhii and Alison, for sharing more than one beer with me and being there for me when I needed you. Thank you to all the previous and current members of the "Who Cares" for welcoming me back into the world of music. Thank you to everybody else in the lab who has made these four years so enjoyable. I will miss you all!

To my friends from home: I could not have done it without you. Nathalie, Christina, Sigrid, Marlene and Antonio - your friendship means the world to me.
To Eva: you have lent me your "sword, bow and axe" to help me fight all my battles since our time in Weymouth. The same way that Frodo couldn't have done it without Sam, I couldn't have achieved anything without you.
To Helena: you have become my family away from home. I will always cherish the time we've spent in our wonderful colocation, and your ability to make me laugh for hours - even during a lockdown.
To the Simplemont-Gang: UNO has never been so fun, and pizza and beers have never tasted so good.

Pablo, thank you for being my calm in the storm. Dancing, hiking, eating - everything is better with you by my side.

And finally the biggest thank you goes to my family. Danke Mama für Deine Geduld. Du hast mir immer den Rücken frei gehalten und mich ermutigt das zu machen, was ich machen will. Danke Papa für Deine Unterstützung und deinen Enthusiasmus für meine Arbeit. Ohne Dich hätte ich es nicht so weit gebracht. Und danke an die beste Schwester und die liebste Nichte der Welt. Ihr zwei seid mein Sonnenschein.

Vevey, April 16, 2023 Carina Trippl

Abstract

The LHCb experiment at CERN's Large Hadron Collider (LHC) is currently taking data with a newly developed Scintillating Fibre (SciFi) Tracker read out with multichannel silicon photomultipliers (SiPMs). The innermost fibre modules, exposed to the highest radiation, will need to be exchanged at the end of the current run, as part of Upgrade Ib (2026–2028). For this consolidation work and in view of Upgrade II (2032–2034) this thesis work focusses on the development of microlens-enhanced SiPMs with increased photon detection efficiency (PDE). A simulation study comparing the expected increase in light detection between SiPMs without and with microlenses has been conducted to guide possible implementations, and has been validated by a simulation based on a commercial software. Microlenses have been deposited on available, non-customised SiPMs. The light yield of a short fibre mat has been measured and the results of different SiPM surfaces compared. For microlens-enhanced SiPMs with a fill factor of 50.0%, an improvement of 32% at a low overvoltage of $\Delta V = 1\,\mathrm{V}$ over SiPMs with a residual layer is seen. This increase drops to 19% at a higher overvoltage of $\Delta V = 4\,\mathrm{V}$. For SiPMs with a larger fill factor of 82.4% no significant difference is observed. For Upgrade II, cryogenic cooling is foreseen to mitigate radiation-induced ageing effects. Irradiated detectors with an advanced technology have been tested, and a reduction in dark count rate of five orders of magnitude between operation temperatures of –40 °C and –196 °C (liquid nitrogen) has been measured. Customised SiPMs, combining a high PDE and low crosstalk probability in the cryogenic technology have been produced and initial promising results are presented.

Keywords: LHCb experiment, Scintillating Fibre (SciFi) Tracker, silicon photomultiplier arrays (SiPMs), microlenses, light yield, photon detection efficiency (PDE), radiation-induced ageing effects, cryogenic cooling.

Zusammenfassung

Das LHCb-Experiment am LHC (CERN) nimmt derzeit Daten mit einem neu entwickelten Szintillator-Fasertracker (SciFi Tracker), der von Mehrkanal-Silizium-Photomultiplikatoren (SiPMs) ausgelesen wird. Die innersten Fasermodule, die der höchsten Strahlung ausgesetzt sind, werden zur Konsolidierung in Upgrade Ib (2026–2028) ausgetauscht. Diese Doktorarbeit konzentriert sich auf die Entwicklung von mikrolinsenverstärkten SiPMs zur Steigerung ihrer Photonendetektionseffizienz (PDE). Diese SiPMs kommen für den Ersatz der SiPMs der auszutauschenden Module in Upgrade 1b und im Hinblick auf Upgrade II (2032–2034) in Frage. Eine Simulationsstudie, um die mögliche Verbesserung der Lichtdetektion zwischen einem Detektor ohne und einem mit Mikrolinsen zu vergleichen, wurde implementiert und mit einer kommerziellen Simulationssoftware validiert. Mikrolinsen wurden auf verfügbaren, nicht kundenspezifischen SiPMs platziert. Die Lichtausbeute einer kurzen Fasermatte wurde gemessen und die Ergebnisse verschiedener Oberflächen verglichen. Für mikrolinsenverstärkte SiPMs mit einem Füllfaktor von 50.0% ist eine Verbesserung von 32% bei einer niedrigen Überspannung von $\Delta V = 1\,\mathrm{V}$ gegenüber SiPMs ohne Mikrolinsen (mit ebener Polymerschicht) zu sehen. Bei einer höheren Überspannung von $\Delta V = 4\,\mathrm{V}$ sinkt diese Verbesserung auf 19%. Bei SiPMs mit einem größeren Füllfaktor von 82.4% wurde kein signifikanter Unterschied beobachtet. Für Upgrade II ist kryogene Kühlung vorgesehen, um strahlungsinduzierte Alterungseffekte abzuschwächen. Bestrahlte Detektoren mit fortschrittlicher Technologie wurden getestet, und eine Verringerung der Dunkel-Zählrate um fünf Größenordnungen zwischen Betriebstemperaturen von –40 °C und –196 °C (Flüssigstickstofftemperatur) wurde gemessen. Kundenspezifische SiPMs, die eine hohe PDE und eine niedrige Crosstalk-Wahrscheinlichkeit mit der Tieftemperaturtechnologie kombinieren, wurden hergestellt. Die ersten vielversprechenden Ergebnisse werden präsentiert.

Schlüsselwörter: LHCb-Experiment, Szintillator-Fasertracker (SciFi Tracker), Silizium-Photomultiplikatoren (SiPMs), Mikrolinsen, Lichtausbeute, Photonendetektionseffizienz (PDE), strahlungsinduzierte Alterungseffekte, kryogene Kühlung.

Résumé

L'expérience LHCb située au Grand Collisionneur de Hadrons (LHC) au CERN acquiert actuellement des données avec un trajectographe à fibres scintillantes (SciFi) nouvellement développé, lu par des photomultiplicateurs multicanaux en silicium (SiPM). Les modules de fibres les plus internes, recevant le rayonnement le plus élevé, seront échangés lors de la prochaine mise à jour de l'expérience (Upgrade Ib, 2026–2028). Dans le cadre du remplacement des SiPMs de ces modules et en vue d'une mise à jour encore plus importante (Upgrade II ,2032–2034), ce travail de thèse porte sur le développement de SiPMs améliorés par des microlentilles pour augmenter leur efficacité de détection des photons (PDE). Une étude de simulation comparant l'augmentation attendue de la détection de lumière entre des détecteurs sans et avec microlentilles a été mise en place pour déterminer les implémentations possibles, et a été validée par une simulation basée sur un logiciel commercial. Des microlentilles ont été déposées sur des SiPM disponibles et non personnalisés. Le rendement lumineux d'un module de fibres courtes a été mesuré et les résultats de différents surfaces comparés. Pour les SiPM équipés de microlentilles avec un facteur de remplissage de 50.0%, une amélioration de 32% à une faible surtension $\Delta V = 1\,\mathrm{V}$ par rapport aux SiPM sans microlentilles (avec une couche de polymère) est observée. Cette amélioration tombe à 19% à une forte surtension de $\Delta V = 4\,\mathrm{V}$. Pour les SiPM avec un facteur de remplissage de 82.4%, aucune différence significative n'est observée. Pour l'Upgrade II, un refroidissement cryogénique est prévu pour atténuer les effets dus à l'irradiation. Des détecteurs avec une technologie avancée ont été irradiés et testés, et une réduction du taux de comptage d'obscurité de cinq ordres de grandeur entre des températures de fonctionnement de –40 °C et de –196 °C (azote liquide) a été mesurée. Des SiPM personnalisés, combinant une haute PDE et une faible probabilité de diaphonie dans la technologie cryogénique ont été produits et les premiers résultats prometteurs sont présentés.

Mots clés : expérience LHCb, tracker à fibre scintillante (SciFi), photomultiplicateurs en silicium (SiPM), microlentilles, rendement lumineux, efficacité de détection de photons (PDE), effets dus à l'irradiation, refroidissement cryogénique.

Contents

Acknowledgements i

Abstract (English/Français/Deutsch) iii

Introduction 1

1 LHCb experiment 3
- 1.1 Physics goals of LHCb . . . 5
- 1.2 LHCb detector for Run 3 . . . 7
  - 1.2.1 Trigger in Run 3 . . . 10
- 1.3 Radiation environment . . . 12
- 1.4 Future upgrades of the LHCb detector . . . 15
  - 1.4.1 Upgrade Ib . . . 15
  - 1.4.2 Upgrade II . . . 16

2 Photodetectors 19
- 2.1 Overview of photodetectors . . . 20
- 2.2 Photomultiplier tubes . . . 22
- 2.3 Semiconductors . . . 23
  - 2.3.1 p-n junction . . . 24
  - 2.3.2 PIN-diode . . . 27
  - 2.3.3 Avalanche photodiode . . . 28
- 2.4 Silicon photomultipliers . . . 29
  - 2.4.1 Gain . . . 33
  - 2.4.2 Photon detection efficiency . . . 34
  - 2.4.3 Noise in a SiPM . . . 35
  - 2.4.4 Timing performance . . . 39
  - 2.4.5 Radiation damage of SiPMs . . . 40
  - 2.4.6 Implications on future SiPM developments . . . 42

3 Scintillating Fibre Tracker for LHCb **45**
3.1 Requirements and implementation . . . 45
3.2 Tracker design and technology . . . 46
3.2.1 Working principle . . . 47
3.3 Scintillating fibres . . . 48
3.4 SiPMs . . . 50
3.5 Readout electronics . . . 52
3.6 SciFi Tracker modules . . . 54
3.7 Radiation damage of the SciFi Tracker . . . 55
3.8 Other applications . . . 57

4 Simulation study of microlens-enhanced SiPMs **59**
4.1 Light propagation through the optical interface . . . 59
4.2 Scintillating fibre exit angle distribution . . . 61
4.2.1 Simulation of the fibre exit angle distribution . . . 61
4.2.2 Measurement of the exit angle distribution . . . 63
4.2.3 Comparison of simulation and measurement . . . 65
4.3 Microlens arrangement . . . 66
4.4 Microlens simulation . . . 68
4.5 Simulation results . . . 71
4.5.1 Impact of the lens radius . . . 72
4.5.2 Impact of the residual height . . . 74
4.5.3 Simulation outcome . . . 76
4.6 Best projection for future implementations . . . 77

5 Implementation and testing of microlens-enhanced SiPMs **79**
5.1 Characterisation of FBK2019-10ch SiPMs . . . 80
5.1.1 Correlated noise determination . . . 80
5.1.2 Measurement of the photon detection efficiency . . . 82
5.2 Microlens production . . . 84
5.2.1 Microlens design . . . 85
5.2.2 Packaging and optical coupling . . . 88
5.3 Testing of the radiation hardness of the microlens material . . . 89
5.4 Light yield measurement setup and method . . . 91
5.4.1 Measurement setup . . . 91
5.4.2 Data analysis . . . 92
5.5 First prototype iteration . . . 96
5.5.1 Light yield of the first prototypes . . . 98

5.6 Second prototype iteration 100
5.6.1 Light yield of samples with 50.0% geometrical fill factor 100
5.6.2 Change in cluster size 103
5.6.3 Coupling tests of samples with 50.0% geometrical fill factor 104
5.6.4 Light yield of samples with 82.4% geometrical fill factor 106

6 SciFi technology development for Upgrade II **109**
6.1 SciFi Tracker with timing information 110
6.2 Cryogenic SiPM operation 113
6.2.1 Fluence dependence of V_{BD} and of the activation energy 115
6.2.2 Fluence and temperature dependence of DCR 117
6.2.3 Fluence and temperature dependence of gain and correlated noise . . . 119
6.3 FBK2022 customised SiPM arrays 120

Conclusion and outlook **125**

A First measurement of the scintillating fibre exit angle distribution **127**

Bibliography **129**

Curriculum Vitae **141**

Introduction

The Large Hadron Collider beauty (LHCb) experiment is one of the big experiments at CERN's LHC. It has been built to measure the parameters of CP violation of beauty (b) and charm (c) hadrons, to study rare decays and to search for new physics phenomena. The LHCb detector is built with state-of-the-art technology needed for exploiting the huge production of heavy-quark hadrons, and achieving the highest precision on observables of interest. The detector has undergone a major upgrade during the 2019–2021 machine shutdown period, and Run 3 data taking has started in 2022. One of the novel subdetectors is the Scintillating Fibre (SciFi) Tracker, a tracking detector made of scintillating fibres with a silicon photomultiplier (SiPM) readout, covering an active detector area of $340\,\mathrm{m}^2$. It is the first time that the SciFi technology has been implemented in a high-radiation environment and at such a large scale and high granularity.

The tracker has to withstand the challenging radiation environment caused by the hadron collisions. Even though the SiPMs are placed outside the acceptance region, they will experience a neutron fluence of 4.1×10^{11} 1 MeV $n_{\mathrm{eq}}/\mathrm{cm}^2$ after an integrated luminosity of 50 fb^{-1}. In the current SciFi implementation, several measures, such as SiPM cooling to $-40\,^{\circ}\mathrm{C}$, an efficient noise rejection system, optimised detector design and neutron shielding, are taken to ensure the required detector performance.

Eventually, after the second major upgrade of the LHCb detector (Upgrade II scheduled in 2032–2034), the rate of proton-proton collisions will increase in order to improve the statistics and thus the precision of the measurements, leading to a dramatic increase in the detector's occupancy and radiation damage. The radiation will also cause a strong decrease in the light yield of the SciFi modules. Therefore, new technologies are needed to bring the detector into this new era. Within the scope of this thesis, I have performed R&D to improve the photodetector's efficiency by implementing microlenses on the SiPMs, and I studied the effect of cryogenic cooling on irradiated devices. Additionally, I have taken part in a testbeam campaign to evaluate the timing performance of short fibre modules, in view of improving the tracking performance.

An overview of the LHC and the LHCb detector is given in Chapter 1. Chapter 2 provides an introduction to photodetectors, with a focus on the SiPM technology. The current implementation of the SciFi Tracker and its working principle are introduced in Chapter 3.

The microlens implementation is divided into two distinct work packages: in a first step, a dedicated ray-tracing simulation based on the ROOT framework [1] (C++) has been performed to evaluate the expected increase in photon detection efficiency of a detector with microlenses compared to a detector with a flat residual layer. It has been used to optimise the different microlens parameters by modelling the SiPM geometry (dead and inefficient areas) and the angular distribution of the photons at the exit of the fibres. The parameter space has been adapted to the possible implementation imposed by the SiPM technology. The simulation study is described in Chapter 4.

The second work package consists of the implementation of microlenses, as presented in Chapter 5. Two campaigns with test samples* provided by the manufacturer *Fondazione Bruno Kessler* (FBK) [2] have been performed, and microlenses have been implemented on two pixel geometries (with geometrical fill factors of 50.0% and of 82.4%) in two iterations. For both iterations, the light yield of a short fibre module has been measured and the results of different SiPM surfaces (microlenses, flat residual layer and bare SiO_2 anti-reflective coating) have been compared. Additionally, the radiation hardness of the microlens material has been validated for ten times the expected total ionising dose for future LHCb upgrades.

In Chapter 6, the developments of the SciFi technology for Upgrade II are described. In collaboration with FBK, cryogenic cooling has been evaluated for irradiated samples and promises a radical change in the dark count rate (DCR) of the SiPM. With the availability of advanced SiPM technologies by FBK, new customised SiPM arrays have been produced. These SiPMs have excellent crosstalk characteristics, and allow the operation at high overvoltage to achieve a PDE above 60%. Additionally, they can be used in cryogenic applications.

The geometry of these samples is compatible with the one of the currently employed SiPMs manufactured by *Hamamatsu Photonics K.K.* (Hamamatsu) [3], so that a possible exchange of the most irradiated modules of the SciFi Tracker is possible after Run 3 in Upgrade Ib (2026–2028). These new modules could use new customised SiPMs equipped with microlenses.

Finally, to achieve an efficient tracking even with an increased occupancy, a SciFi Tracker with timing information is envisioned. A dedicated telescope has been constructed and characterised, and its efficiency and timing resolution measured.

*These test samples are not specifically developed for the LHCb SciFi Tracker.

1 LHCb experiment

CERN's Large Hadron Collider (LHC) is the world's biggest accelerator and storage ring with a circumference of 27 km. The tunnel, that houses the LHC, is approximately 100 m below ground at the border region between France and Switzerland. A massive complex of an ion source, pre-accelerators and accelerators, as shown in Fig. 1.1, injects particles into the LHC ring, where they are circulated in opposite directions and accelerated to nearly the speed of light. The beams are divided into up to 2808 bunches of approximately 1.8×10^{11} protons with a bunch crossing frequency of 40 MHz. At four interaction points the two proton beams produce head-on collisions at an unprecedented center-of-mass energy of $\sqrt{s} = 13.6$ TeV. Even though the so-called proton runs dominate the accelerator schedule, also lead and xenon ions are accelerated during several weeks of the year with up to $\sqrt{s} = 5.5$ TeV.

The collisions are recorded by nine different experiments. The detectors of the four large-scale experiments ATLAS [5], CMS [6], ALICE [7] and LHCb [8] are installed in caverns at the four main interaction points, illustrated in Fig. 1.2. ATLAS and CMS are general purpose experiments, ALICE is specialised to study the quark-gluon plasma in heavy-ion collisions, and LHCb is dedicated to measure rare decays and CP-violation parameters to explain the matter-antimatter asymmetry. This experiment is described in more detail later in this chapter. Additionally, five dedicated experiments, TOTEM [9], LHCf [10], MoEDAL-MAPP [11], FASER [12] and SND@LHC [13], study particles produced at the main interaction points mostly in the very forward direction at unprecedented energy ranges and particle fluences.

The *Large Hadron Collider beauty* (LHCb) experiment is a single-arm forward spectrometer specialised to detect the decay products of hadrons containing beauty (b) and charm (c) quarks. The first version of the detector was successfully operated from 2009 until 2018. Groundbreaking discoveries, like the first pentaquark [15] or the thus far largest CP asymmetry measured in the $B^{\mp} \to D[K^{\pm}\pi^{\mp}\pi^{\mp}\pi^{\pm}]\, h^{\mp}$ decay [16], resulted in over 600 publications in peer-reviewed journals. During the second Long Shutdown (LS2) (2018–2021) a major detector upgrade was installed and is in operation since spring 2022.

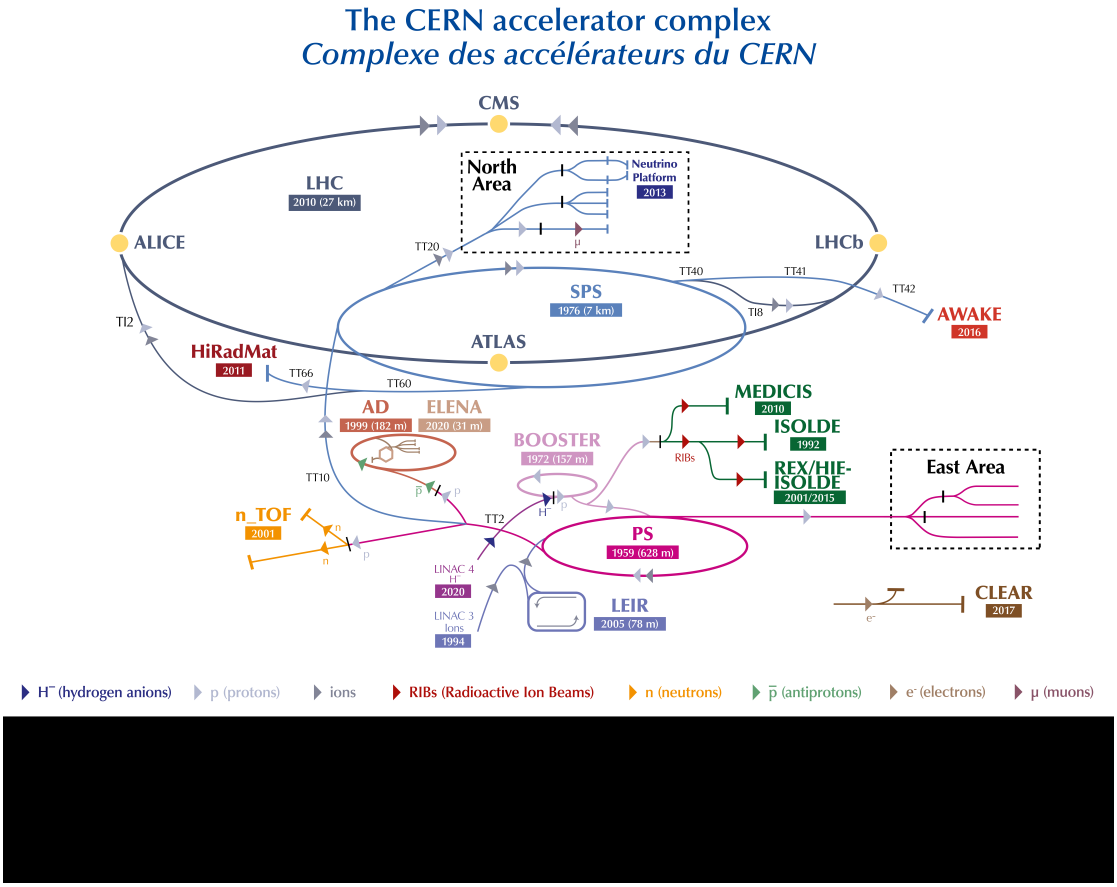

Figure 1.1 – The accelerator complex providing high-energy protons to the LHC experiments. Negative hydrogen ions get accelerated at LINAC4 to 160 MeV before they are stripped off their electrons and enter the Proton Synchrotron Booster (PSB). The remaining protons enter the Proton Synchrotron (PS) with 2 GeV of energy and are accelerated to 26 GeV before continuing to the Super Proton Synchrotron (SPS). Here the protons acquire an energy of 450 GeV before they finally enter the LHC, where they are accelerated to 6.8 TeV. *Picture taken from Ref. [4].*

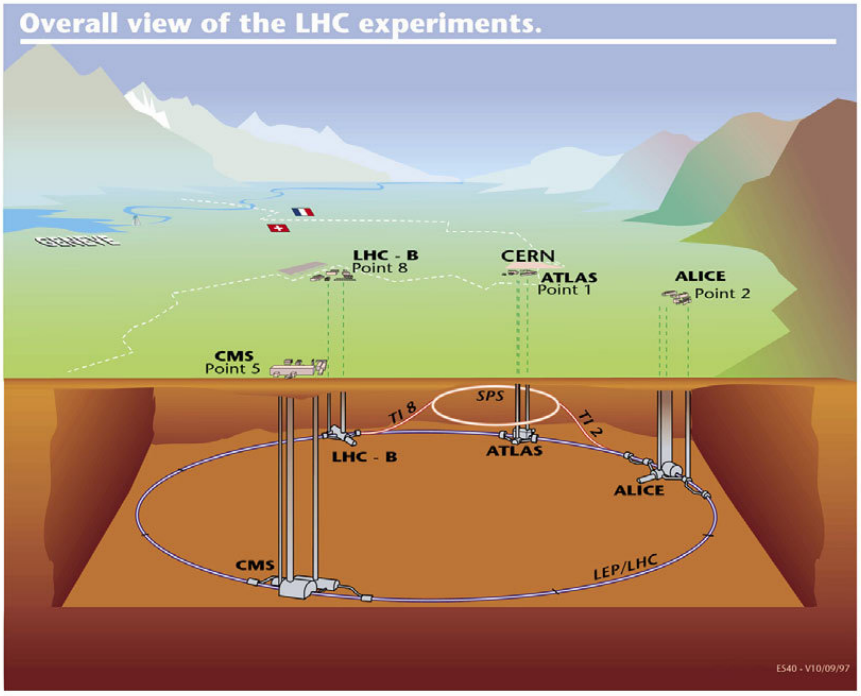

Figure 1.2 – The four interaction points at the LHC at CERN. *Picture taken from Ref. [14].*

1.1 Physics goals of LHCb

The Standard Model (SM) of particle physics is a theoretical model which describes the three fundamental forces, i.e. the electromagnetic, weak and strong forces, as well as the elementary particles that make up the known part of our universe. The discovery of the Higgs boson in 2012 at CERN [17, 18] answered the last missing puzzle of the theory, namely the origin of the particles' masses. However, there are still many observations that cannot be explained with this fundamental theory. Searches for physics beyond the SM are essential in the physics programme of many experiments, in particular the LHCb experiment. Some of the unexplained phenomena are [19]:

- **Dark matter and dark energy:** The observable matter in the universe accounts for only 5% of the total energy. The rest is divided into approximately 27% of dark matter, detected via its gravitational effects on galaxies and stars, and 68% of dark energy, responsible for the expansion of the universe. Following the current cosmological models, this leaves us in the state where 95% of the content of the universe is unexplained. [20]

- **Neutrino masses:** Neutrinos are neutral, fundamental particles interacting via the weak force. Even though electron, muon and tau neutrinos are considered massless in the SM, the observed neutrino flavour oscillations prove that they must have mass [21]. Measuring their properties is an important physics goal addressed by many dedicated neutrino experiments, such as SND@LHC [13], FASERν [22], IceCube [23] or Super-Kamiokande [24].

- **Gravity within the SM:** The universe is governed by the laws of four fundamental interactions. However, only three of them are incorporated into the description of the SM. The missing one, gravity, is described by the general theory of relativity published by A. Einstein in 1915 [25]. It describes the universe with a four-dimensional, curved space-time, in contrast to the theory of the SM which relies on quantum mechanics to describe the elementary forces and particles. Until now a unification of the two theories has not been successful.

- **Baryon asymmetry:** The Big Bang theory explains the creation of the universe about 14 billion years ago, and predicts that equal amounts of matter and antimatter were produced. The universe however is predominantly made up of matter, and up to now no large amount of antimatter has been detected. This leads to the question of the origin and the magnitude of this symmetry breaking. [26]

The LHCb experiment [27] has been designed with an emphasis on studying the parameters of CP violation*, which could explain the matter-antimatter asymmetry. The large production rate of b and c hadrons from proton-proton collisions in the LHC offers the unique opportunity to study heavy flavour physics. As both, b and $\overline{b}$ quarks, are dominantly produced in the same forward or backward cone, which is shown in Fig. 1.3, LHCb has been designed as a single-arm forward spectrometer covering a pseudo-rapidity range of $2 < \eta < 5$. Since its beginning, LHCb has evolved from a dedicated heavy flavour physics to a general purpose experiment, studying not only hadrons containing beauty or charm quarks but also performing rare kaon decay measurements, studying heavy bosons, as well as searching directly for new particles. [28]

Even though LHCb has produced significant results from the first two data-taking periods (Run 1 from 2010 to 2012 and Run 2 from 2015 to 2018) there are still many mysteries left to uncover. Additionally, many of these obtained results are limited in their precision by statistics, calling for more data. Therefore, the detector was upgraded [29] for the current data-taking period Run 3 from 2022–2025, allowing the operation of the experiment at higher instantaneous luminosity. The upgraded detector features a readout system that can acquire

*CP stands for charge conjugation (C) and parity (P).

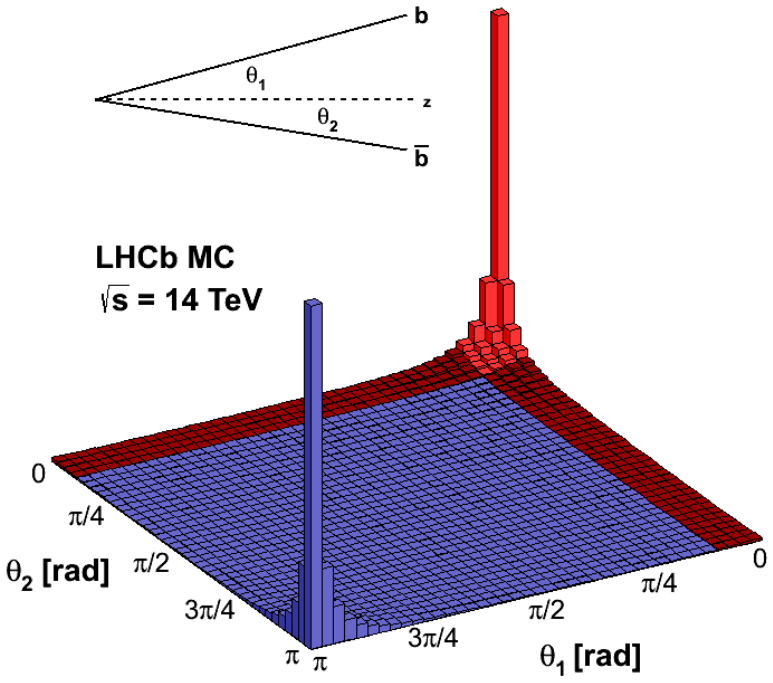

Figure 1.3 – The angular distribution of $b\bar{b}$ production from proton-proton collisions at $\sqrt{s} = 14$ TeV. The red area highlights the coverage of LHCb. *Picture taken from Ref. [30].*

the full data of the proton-proton interactions, opening the door to a software-based event selection with higher efficiency and a reduction of the statistical uncertainties.

1.2 LHCb detector for Run 3

An important parameter to describe the performance of a collider is the *instantaneous luminosity* $\mathscr{L}$. It is the proportionality factor between the cross section of a physics process σ_{event} and the number of interactions that have happened per unit time $d\text{N}/d\text{t}$:

$$\frac{d\text{N}}{d\text{t}} = \mathscr{L} \cdot \sigma_{\text{event}}\,. \tag{1.1}$$

If the luminosity is integrated over time, it is called *integrated luminosity*. It is proportional to the total number of events collected during this time. The integrated luminosity is measured in fb^{-1}.

The LHC can provide an instantaneous luminosity of almost 2×10^{34} cm^{-2}s^{-1} in Run 3. In the previous data-taking periods, LHCb tuned the instantaneous luminosity to have a collision rate between 1.1 and 2.5 visible proton-proton interaction per bunch crossing, collecting data at an instantaneous luminosity of $\mathscr{L} = 1.5 \times 10^{32}$ cm^{-2}s^{-1}. This allowed the collection of a total integrated luminosity of 9 fb^{-1} for Run 1 and 2 together [31]. In Run 3, the instantaneous luminosity at LHCb will significantly increase (approximately ten times) aiming to collect 40 fb^{-1} of data. The expected number of visible proton-proton interactions per bunch crossing is increased to $\mu \geq 5$. [32]

During the Long Shutdown 2 (LS2) (2018–2022) the LHCb detector was upgraded (described e.g. in Ref. [29]) replacing all of its tracking detectors, updating the Ring-Imaging Cherenkov (RICH) detector systems and exchanging all of the readout electronics to cope with the higher rate that is expected in Run 3. The detector, shown in Fig. 1.4, consists of the following subdetectors:

The VELO: The VErtex LOcator (VELO) is the detector closest to the interaction point. It surrounds the beam at a distance of 5.1 mm for precise vertex point measurements. The close distance is achieved by placing the detector modules in a secondary vacuum, and installing only a thin foil to separate the beam vacuum from the VELO one. The silicon strip detectors from Run 1 and 2 have been replaced with silicon pixel detectors to improve the VELO's position resolution and radiation hardness. The sensors with a pixel size of 55 µm × 55 µm are installed on two L-shaped halves, which are mounted on movable stages. These two halves are only closed during beam collisions to reduce the radiation exposure due to the larger beam dimension during injection time. [33]

The RICH detectors: Two Ring-Imaging CHerenkov (RICH) detectors, one upstream and the other downstream of the dipole magnet, use the Cherenkov effect to determine the velocity of charged particles. Combined with momentum measurements of the tracking detectors and the magnetic field, the RICH information allows particle identification (PID), in particular for kaons, pions and protons. The detectors are filled with C_4F_{10} (in the case of the RICH-1) and CF_4 (for the RICH-2) gases, which are adopted to optimise PID resolution in two different momentum ranges. The produced Cherenkov light is reflected and deviated by a dedicated optical system onto a plane of photodetectors, i.e. multi-anode photomultiplier tubes. [34]

The UT: The Upstream Tracker (UT) is a dedicated tracking detector installed in front of the magnet. It is made of silicon strip sensors with a pitch of 95 – 190 µm. The sensors and the integrated front-end electronics are mounted double-sided on supportive staves. The staves are arranged such that they form four detector planes (x-u-v-x). [28]

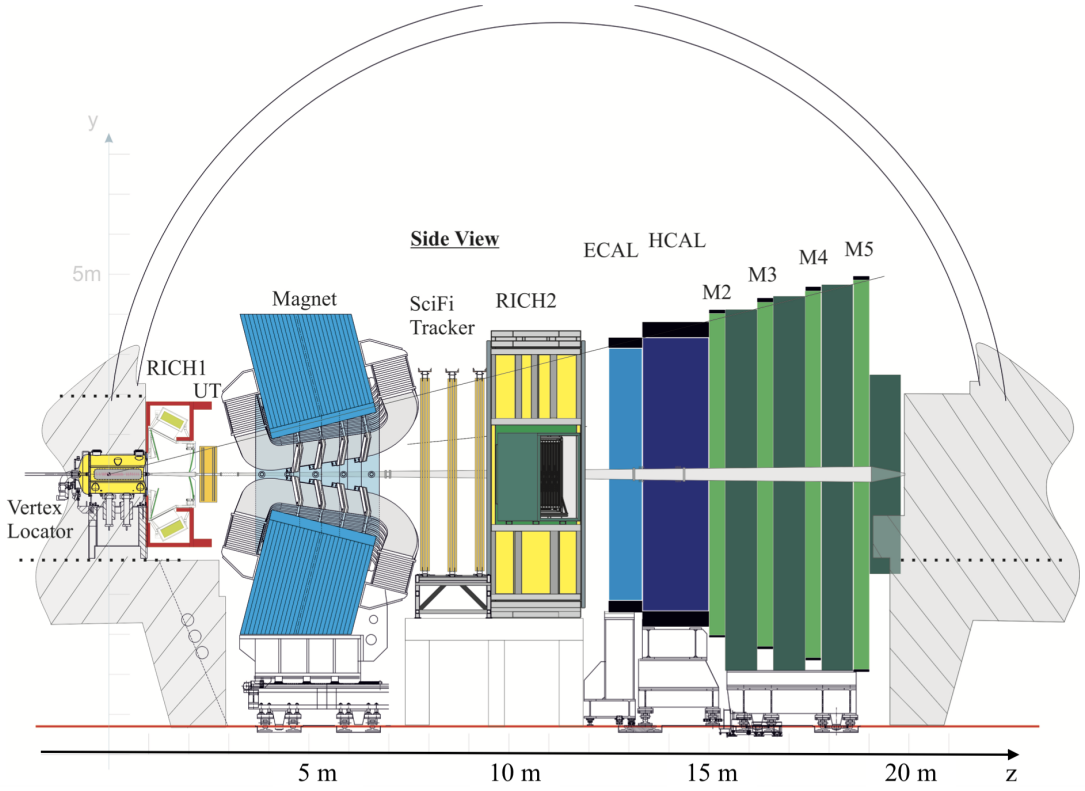

Figure 1.4 – Schematic sideview of the LHCb detector. *Picture taken from Ref. [28].*

The dipole magnet: LHCb's magnet is a warm dipole magnet bending the trajectories of charged particles in the horizontal plane with a bending power of about 4 T·m to determine the particles' momentum. The polarity of the magnet can be inverted to reduce systematic errors in the tracking of the particles. This is especially important as LHCb is performing precision CP-violation measurements. [27]

The SciFi Tracker: The Scintillating Fibre (SciFi) Tracker is placed downstream of the magnet. It is made of scintillating fibres read out by multi-channel silicon photomultiplier arrays (SiPMs) with a channel size of 250 µm. The whole tracker is composed of twelve detection layers grouped into three stations (T1, T2, T3), and covers a total area of 340 m^2. Each detector plane is divided into five or six modules, which are mounted on C-frames that carry additionally to the modules the readout electronics and the other detector infrastructure. The SciFi Tracker is described in more detail in Chapter 3. [28]

The ECAL: The electromagnetic calorimeter (ECAL) measures the energy of electrons, positrons and photons. It is a sampling calorimeter, using a Shashlik technology: scintillating bars and lead absorbers are interleaved in a sandwich structure. Wavelength-shifting fibres are inserted to collect and transport the produced scintillating light towards photomultiplier tubes. With a thickness of 25 radiation lengths all incoming electrons, positrons and photons will deposit their energy in the form of electromagnetic showers. [34]

The HCAL: The hadronic calorimeter (HCAL) follows the same principle as the ECAL, but measures the energy deposits of hadrons such as protons, neutrons, pions and kaons. Instead of lead the HCAL employs iron in between the scintillating blocks. The thickness of the HCAL is 6 nuclear interaction lengths, allowing the hadrons to deposit their energy as hadronic showers. [34]

The muon system: As muons are present in the final states of many interesting decay channels, it is crucial to identify them in the LHCb detector. The muon system is composed of four stations with gas chambers and iron walls. The chambers are multi-wire proportional chambers, detecting the passing muon. [34]

PLUME: A new luminosity detector is installed upstream of the VELO. Probe for LUminosity MEasurement (PLUME) is a dedicated detector system to monitor the instantaneous luminosity and the visible proton-proton interactions per bunch in real time. Photomultiplier tubes are staggered around the beampipe in a hodoscope structure. Particles from the interaction point produce Cherenkov light in quartz tablets coupled to the entrance window of the photodetectors. PLUME employs a direct particle counting technique (yes/no), which is possible due to its small size and the thus small expected occupancy. [35]

1.2.1 Trigger in Run 3

An important feature of the detector for Run 3 is the upgraded trigger system to readout the full data at the bunch crossing frequency of 40 MHz, as described in Ref. [36]. The real-time data acquisition (DAQ) system of LHCb builds events on customised PCIe40 cards based on field-programmable gate arrays (FPGAs). The front-end information is transmitted on optical links and combined by a set of dedicated servers. These so-called event builders combine the event data from all subdetectors and forward them to an event filter farm (EFF). In the EFF the data is reconstructed, and only interesting events are stored permanently. The event selection is done by the High Level Trigger (HLT). In the first stage (HLT1), which runs on Graphical

Processing Units (GPUs), a partial event reconstruction with data from the tracking detectors (VELO, UT and SciFi) is performed. The software trigger processes the expected data rate of 40 Tbit/s [37]. After a first data selection, the full data is reconstructed in the second step of the trigger (HLT2) and interesting events are sent to storage. With HLT1, LHCb is the first high energy physics experiment employing a high-throughput GPU trigger system. The advantage is a highly efficient event selection compared to the hardware trigger from Run 1 and 2.

Momentum measurement and tracking

The momentum of charged particles is measured using their deflection in the magnetic field. The position before and after the dipole magnet is determined by the tracking detectors, and the momentum is calculated using the deflection angle. For short-lived neutral particles, the momentum of the decay products is used, relying on momentum conservation.

Figure 1.5 shows the possible track types in the experiment. In the HLT1, the first event selection is performed on particle tracks with hits in the VELO, UT and the SciFi Tracker. These tracks are called *long tracks* and have the best quality for physics analysis, due to the well defined information of the interaction point and the very high momentum resolution given by the information before and after the magnet. *T tracks* are detected by the SciFi only. They are used as input to reconstruct *downstream tracks*, by adding hits in the UT and the SciFi. Downstream tracks are the daughter tracks of long-lived particles, for which the decay occurs outside the VELO. Particles that are bent by the magnet out of the detector acceptance are reconstructed as *upstream tracks*. Finally, *VELO tracks* are tracks seen only by the VELO, and are usually incorporated at a later stage in long or upstream tracks. [28]

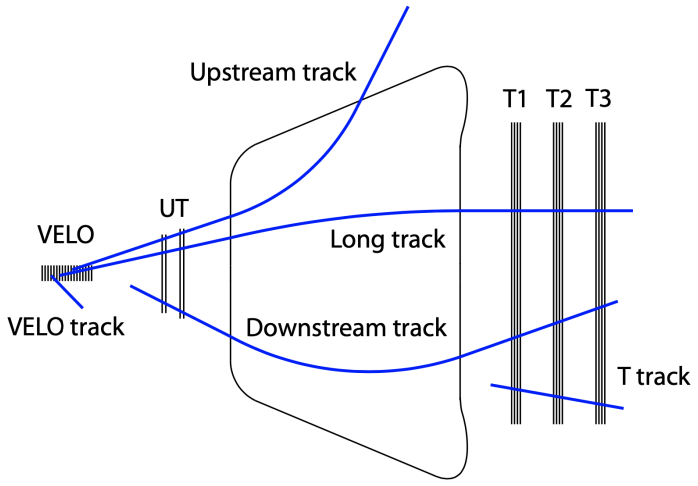

Figure 1.5 – Different track types in the LHCb experiment. *Picture taken from Ref. [28].*

1.3 Radiation environment

In high-energy particle collisions many different particles are produced. Depending on the particle, its energy loss when interacting with matter can either be ionising or non-ionising.

Charged particles produced directly at the collision or as secondary decay products deposit energy in matter via Coulomb interactions with electrons, by excitation and ionisation of the atom [38]. Photons with sufficient energies (above the UV spectrum) can also cause ionisation when interacting via the photoelectric and Compton effects. The damage can be directly related to the irradiation, i.e. the dose, expressed in Gray (Gy).

Neutral and low-energy charged particles can interact with the nucleus of the surrounding material. In a semiconductor, this results in the energy dissipation by the atom in the form of phonons or in the atom's displacement [39]. Displaced atoms are called interstitials, and create a vacancy in the crystal structure. The mobility of interstitials is strongly temperature dependent, which allows produced vacancies to be refilled, resulting in so-called annealing. However, if the lattice vacancy is bound by other atoms, it can form a stable defect which will have an impact on the macroscopic properties of the material.

For a SiPM two different types of damage can be observed. Ionising energy loss (IEL) will cause surface damage, which changes the electric field and increases the leakage current. Bulk damage, caused by non-ionising energy loss (NIEL), increases the dark count rate (DCR). [40]

Radiation effects of different particles can be scaled linearly to the resulting radiation damage. This is referred to as *NIEL scaling* [41]. As described in Ref. [42], the fluence of particles Φ crossing the material is scaled to the equivalent damage induced by 1 MeV neutrons using a hardness factor $k(E) = D(E)/D(n)$, where $D(E)$ is the displacement damage function for particles with energy E and $D(n)$ for 1 MeV neutrons:

$$\Phi_{\text{eq}} = k(E) \cdot \Phi . \tag{1.2}$$

The equivalent fluence Φ_{eq} is given in 1 MeV $n_{\text{eq}}/\text{cm}^2$. In Fig. 1.6, the hardness factor in silicon is shown for different particles.

All LHCb subdetectors are heavily exposed to the harsh radiation environment. To ensure the operation and detector performance throughout the lifetime of the detector, simulation studies in FLUKA [49, 50] have been performed to evaluate this radiation environment for every subdetector. This was crucial for the design choices of the subdetectors. The results for the VELO, the SciFi Tracker and the ECAL are listed below to provide an overview of the expected irradiation levels in LHCb.

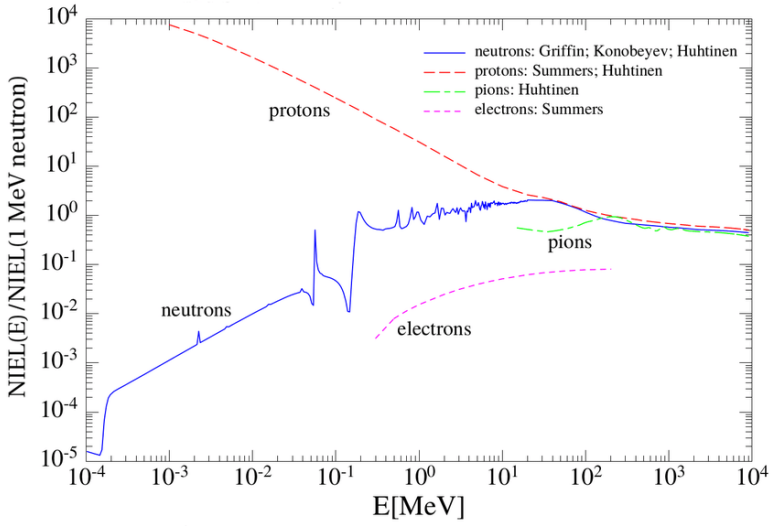

Figure 1.6 – The hardness factor in silicon of different particles. The data has been normalised to 1 MeV n_{eq}/cm^2. The data, summarised by Ref. [43], is based on Ref. [44–47]. *Picture taken from Ref. [48].*

VELO

As explained in Ref. [33], the VELO is exposed to the highest radiation dose as it is the sub-detector closest to the interaction point. The simulation in FLUKA shows that an integrated luminosity of 50 fb^{-1} corresponds to a maximum integrated fluence of 8×10^{15} 1 MeV n_{eq}/cm^2 in the region around the interaction point. Figure 1.7 shows the full estimated integrated dose per fb^{-1} of the covered detector radius r versus z position, which is the direction along the beam line. [33]

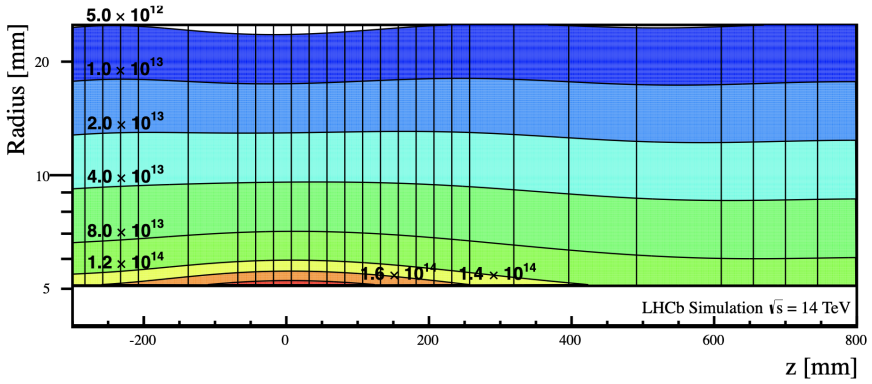

Figure 1.7 – Simulated integrated dose in the VELO region per fb^{-1} using FLUKA. The vertical lines represent the locations of the VELO stations. *Picture taken from Ref. [33].*

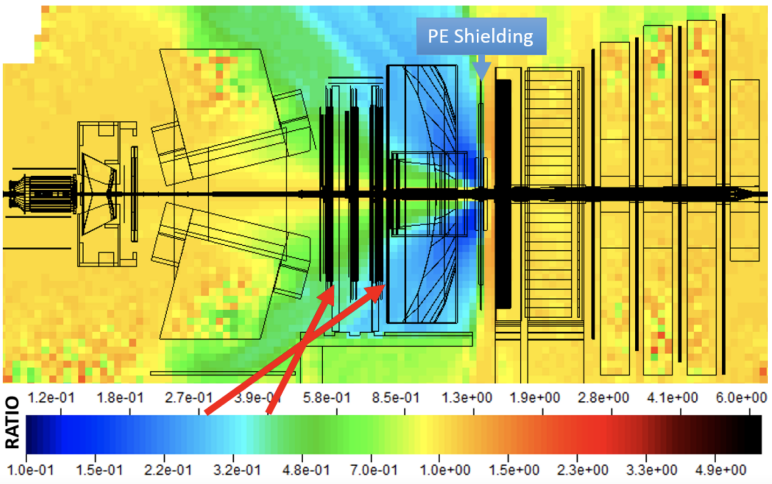

Figure 1.8 – Simulated ratio of the radiation environment with and without the neutron shielding for the SciFi Tracker using the FLUKA framework. The shielding is made of 95% polyethylene and 5% boron. *Picture taken from Ref. [51].*

SciFi

The radiation level was simulated in FLUKA for the SciFi stations T1 and T3 after an integrated luminosity of 50 fb^{-1} and a proton-proton total cross-section of 84 mb, as detailed in Ref. [51]. The main radiation source at the position of the SiPMs are neutrons backscattering from the calorimeters. This will lead to a maximum fluence around the beampipe of 8.1×10^{11} 1 MeV $n_{\text{eq}}/\text{cm}^2$ for T1 and 14×10^{11} 1 MeV $n_{\text{eq}}/\text{cm}^2$ for T3. An efficient neutron shielding has been designed and installed in front of the ECAL, reducing the fluences by factors of 2.5 and 3.4 down to 3.2×10^{11} 1 MeV $n_{\text{eq}}/\text{cm}^2$ and 4.1×10^{11} 1 MeV $n_{\text{eq}}/\text{cm}^2$, respectively. The expected radiation environment is shown in Fig. 1.8. The absorbed ionising dose will be 40 Gy at T1 and 80 Gy at T3 at the SiPMs' position. For the scintillating fibres the highest radiation is seen close to the beampipe, where an ionising dose of 35 kGy for T1 and 25 kGy for T3 is expected. [51]

ECAL

The highest radiation dose is expected at the front of the ECAL and in a horizontal region at the level of the beampipe. The ECAL was designed to withstand radiation up to 2.5 kGy per year for ten years. A simulation study in FLUKA as well as measurements with Alanine sensors[†] were performed in 2011 and 2012, and are compared in Fig. 1.9. They show a maximum dose of roughly 1 kGy and 2 kGy in the innermost region, respectively. The total dose for an integrated luminosity of 50 fb^{-1} amounts to approximately 50 kGy. [52]

[†]Alanine sensors are used as dosimeters to measure radiations between 1 Gy and 120 kGy [52].

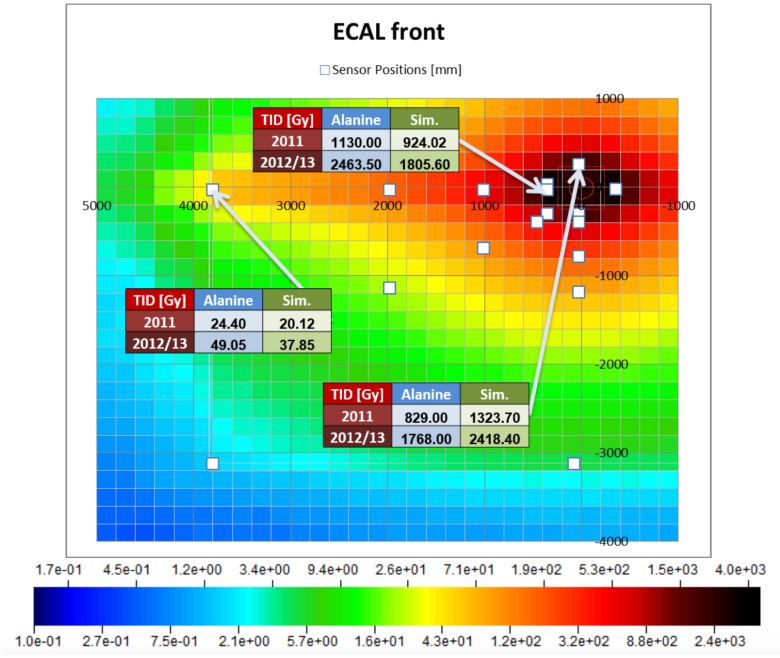

Figure 1.9 – Radiation dose on the front of the ECAL, simulated using FLUKA. The colour scale represents the ionisation dose in kGy. The simulated values (green column) for a $\sqrt{s} = 8\,\text{TeV}$ are compared in the tables to selected measurement positions (white squares) of the radiation dose measured by Alanine sensors (blue column) for Run 2. *Picture taken from Ref. [52].*

1.4 Future upgrades of the LHCb detector

The currently foreseen timeline of the next major LHCb detector upgrades is shown in Fig. 1.10. LHCb Upgrade Ib is scheduled during the Long Shutdown 3 (LS3) in 2026–2028, and Upgrade II during LS4 in 2032–2034, both described in Ref. [53].

1.4.1 Upgrade Ib

After Run 3, the works on the LHC accelerator for the high-luminosity upgrade will be finalised. With this upgrade the LHC's instantaneous design luminosity will be increased by a factor of five. LS3 provides the opportunity to perform preparatory installations for the LHCb Upgrade II. Additionally, consolidation works can be performed on the central SciFi modules with the fastest ageing due to radiation. Depending on the observed degradation of the hit detection efficiency in Run 3, the central modules will be entirely replaced (fibres and SiPMs). This allows the installation of new SiPMs with an enhanced photon detection efficiency (see Chapters 4 and 5). Moreover, a part of the inner region of the SciFi Tracker may be converted to a silicon pixel detector in a proof-of-concept installation for Upgrade II. The combination of

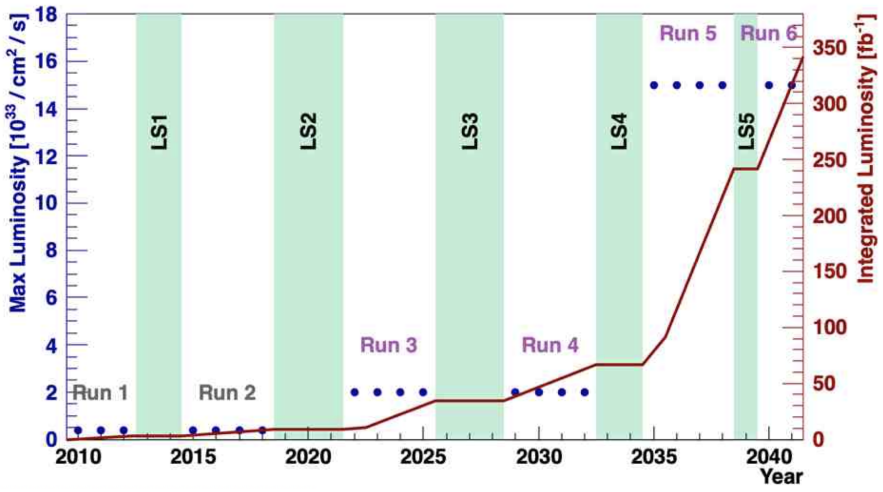

Figure 1.10 – The expected time schedule of the LHCb experiment. *Picture taken from Ref. [31].*

SciFi technology and silicon pixel detector envisioned for Runs 5 and 6 is known as the Mighty Tracker, and will improve the tracking efficiency in the region with the highest occupancy.

Finally, a new tracking detector inside the dipole magnet is planned to be installed [53]. The new subdetector system will measure low-momentum particles that are deflected by the magnetic field outside of the acceptance. As shown in Fig. 1.11, four panels will be placed inside the magnet. 5 mm-thick, rhomboidal-shaped scintillating bars read out by green wavelength-shifting fibres are grouped into four layers per panel. Clear plastic optical fibres transport the light from the scintillating bars to SiPMs stationed outside the magnet. All the electronic equipment is also placed outside the acceptance region in order to keep the material budget low. [53]

1.4.2 Upgrade II

In Run 5, LHCb is aiming to operate the detector at up to ten times higher instantaneous luminosity of 1.5×10^{34} cm^{-2} s^{-1}, planning to reach a five times higher total integrated luminosity of 240 fb^{-1} (see Fig. 1.10). This will put a significant strain on all the subdetectors in terms of occupancy (increase of a factor of ten) and radiation (increase of a factor of five). The tracking detectors will therefore be completely replaced to maintain a high tracking efficiency. The Mighty Tracker (with an Inner and Middle Tracker made of silicon pixels and an outer tracker made of scintillating fibres) will replace the current SciFi Tracker downstream of the magnet. [53]

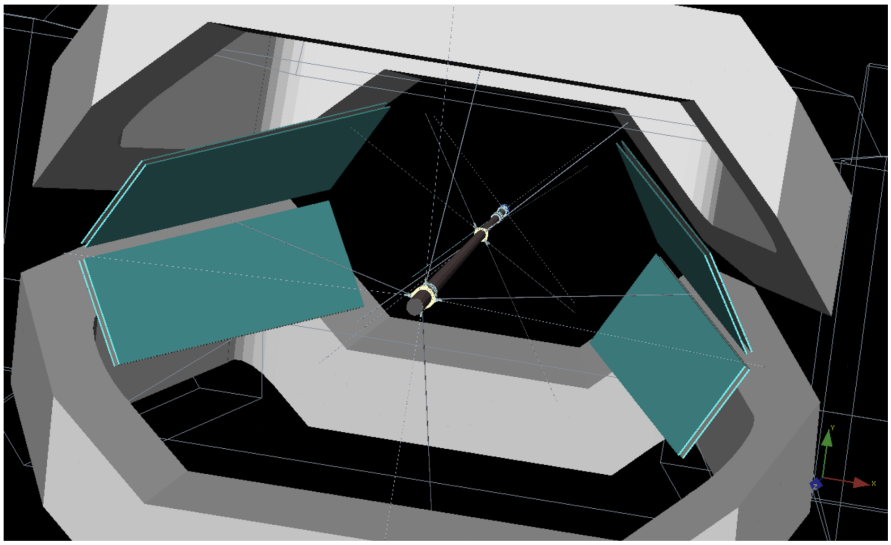

Figure 1.11 – Placement of the Magnet Stations inside the dipole magnet. *Picture taken from Ref. [53].*

The Mighty Tracker combines the SciFi Tracker with silicon pixel detectors in the region around the beampipe. The design of the Mighty Tracker can be seen in Fig. 1.12. The silicon detectors will be installed on six of the twelve layers of the tracking stations, covering a total of approximately 18 m^2. The prototype of the MightyPix sensors is based on MuPix10 [54] and ATLASpix3 [55] sensors and uses a High-Voltage CMOS (HV-CMOS) technology. In the current version, the sensors have a pixel size of 55 µm × 165 µm. They are mounted double-sided on a Kapton flex-circuit and grouped into modules of size 20 cm × 54 cm. 28 modules of silicon sensors and cooling pipes form one silicon layer. A schematic picture of a module is shown in Fig. 1.13. The monophase liquid cooling allows the operation of the sensors at 0 °C to cope with the high radiation. [53]

Due to the high radiation environment the DCR of the SiPMs is expected to increase to a level far beyond the acceptable rate of ≈ 10 MHz per channel, even while cooled to −40 °C. Therefore cryogenic cooling is envisaged, which will keep the DCR at the level of tens of kHz per channel. First studies on irradiated SiPMs have been performed in this thesis for Upgrade II, and are discussed in detail in Sec. 6.2. For the operation at cryogenic temperatures, the SiPMs have to be installed in a vacuum environment. This can only be achieved either via an intermediate optical interface made from clear fibres, or with a direct feed-through of the scintillating fibres into the vacuum box. In the first case, a loss in light of approximately 20% is expected, whereas in the second case longer fibre mats are needed (increase of ≈ 15 cm) with a negligible impact on the light yield. For both options, the installation of SiPMs with a higher detection efficiency is crucial to counteract the degradation of the scintillating fibres due to

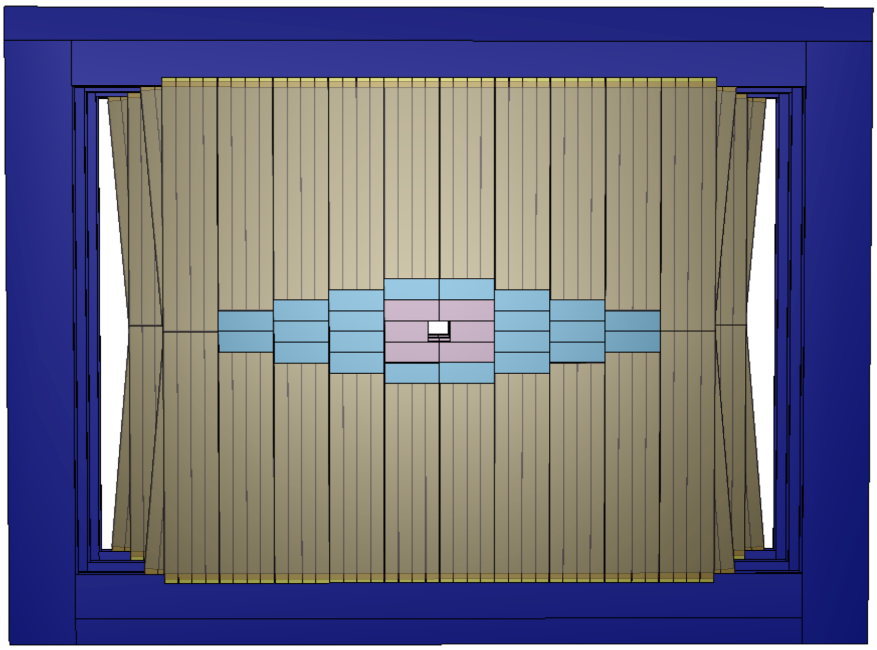

Figure 1.12 – Design of the Mighty Tracker. The outer part (brown) is made of SciFi modules. The Inner Tracker (pink) and the Middle Tracker (blue) are made of silicon sensors. A part of the Inner Tracker may already be installed during LS3 in a proof-of-concept installation. The complete Mighty Tracker will be installed in LS4. *Picture taken from Ref. [53].*

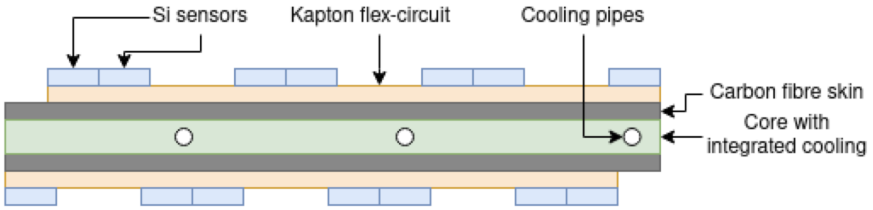

Figure 1.13 – Cross-section of the sandwich structure of the silicon module. *Picture taken from Ref. [56].*

the higher radiation exposure. This can be achieved by implementing microlenses on the SiPM pixel surface to deviate light into the active area, effectively increasing the geometrical fill factor and therefore the PDE. The results of a simulation and prototyping campaign are detailed in Chapters 4 and 5 of this thesis.

2 Photodetectors

Photodetectors are devices dedicated to the detection of incoming light and its conversion into an electric signal. In high energy physics, photosensors are mainly used together with scintillators or to detect Cherenkov radiation. Typical materials are *photocathodes*, made from alkali materials such as cesium iodide (CsI) or gases like tetrakis dimethyl-amine (TMAE), and *semiconductors*, where silicon (Si) is the most used. [57]

This chapter provides an overview of photodetectors employed in high energy physics, such as vacuum-based, gaseous-based and solid-state devices. Here, the most common detectors work in a spectral range from vacuum-ultraviolet (VUV) [58] to near-infrared (NIR) [59]. In this range the photon has an energy of a few electronvolts (eV). Therefore, photodetectors rely on the photoelectric effect to detect incoming light. In this type of process, the photon energy $E_\gamma = h\nu$ is higher than the binding energy of the electron E_{bin}, and the photon will transfer all of its energy to the electron. The electron will be ejected from the atom with an energy equal to $E_{\text{p.e.}} = h\nu - E_{\text{bin}}$.

One distinguishes conventionally between the *internal* and the *external* photoelectric effects. The internal photoelectric effect is used in semiconductors. When absorbing the photon, an electron is moved from the valence to the conduction band, and can from then on be considered as a free electron. The external photoelectric effect is used with a metal surface or a photocathode, extracting the electron from the surface or the cathode. [60, 61]

2.1 Overview of photodetectors

As described in Ref. [57], the most common photodetectors can be categorised as follows:

- **Vacuum-based photodetectors** employ the external photoelectric effect to produce a free electron. Typical detectors are photomultiplier tubes, hybrid photodetectors and microchannel plates. They all have an electron amplification stage specific to the detector type.
- **Gaseous-based photodetectors** either use photosensitive gas molecules or a solid photocathode to release the primary electron via external photoelectric effect. The released photoelectron moves towards the anode and, due to the high electric field, triggers the avalanche in the gas. The produced ions have a low mobility in the gas, and thus these types of photodetectors can be operated in a magnetic field. They are typically employed in Cherenkov detectors instead of vacuum-detectors due to their cost-efficient large coverage. Additionally, they have a lower noise level and a higher gain than solid-state devices [62]. A prominent example of this technology is the ALICE RICH detector, where segmented photocathodes are coated with CsI, and used in a multi-wire proportional chamber [63].
- **Solid-state photodetectors** employ semiconductors to detect incoming photons. The internal photoelectric effect will create the primary electron and, depending on the photodetector type, create an avalanche amplification (e.g. in avalanche photodiodes or SiPMs) or not (PIN-diode). The most commonly used material is silicon, due to its high quantum efficiency in the visible spectral range, thermal range, availability in nature and its wide use in industry.

Ideally, photodetectors would show a linear response to the incoming photon flux and detect all incoming photons. However, they have limited linearity and a detection probability smaller than 100%. Additionally, the detected signal shows statistical fluctuations, which is especially important for low-light detection applications [64].

One of the most important features concerning detection probability is the quantum efficiency, which is defined as the ratio between the number of generated photoelectrons (PE) N_{PE} over the total number of incoming photons N_{tot} [57]:

$$\mathrm{QE} = \frac{N_{\mathrm{PE}}}{N_{\mathrm{tot}}}. \tag{2.1}$$

As can be seen in Fig. 2.1, the QE is wavelength dependent. For the emission spectrum of the LHCb SciFi Tracker peaking at a wavelength of $\lambda = 450\,\text{nm}$, shown in Fig. 2.2 for several fiber lengths, silicon is clearly outperforming any photocathode materials, with a QE of more than 80%.

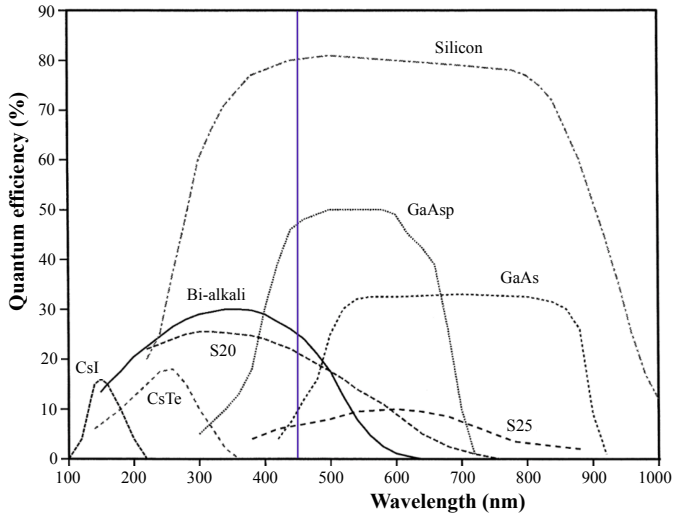

Figure 2.1 – Quantum efficiency of several different photocathodes compared to silicon. The vertical line at $\lambda = 450\,\text{nm}$ indicates the wavelength of the peak emission of the LHCb SciFi Tracker. *Picture taken from Ref. [65].*

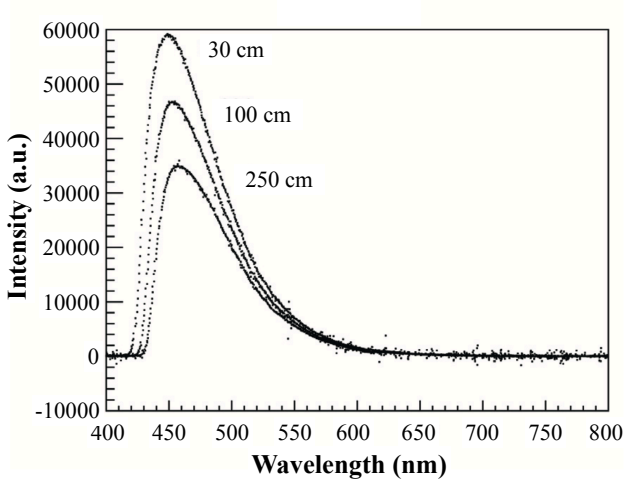

Figure 2.2 – Emission spectrum at different fibre lengths of the scintillating fibre SCSF-78MJ used in LHCb SciFi Tracker. *Picture taken from Ref. [28].*

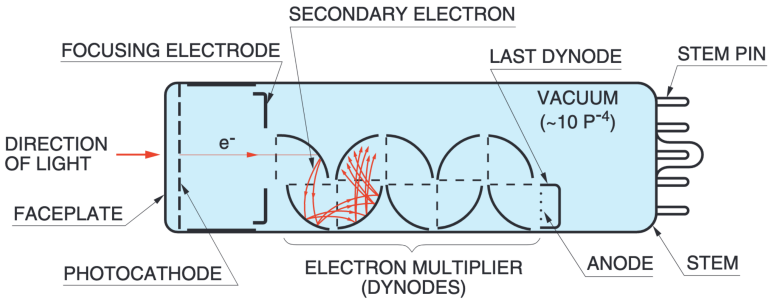

Figure 2.3 – Schematic design of a PMT with a ten dynodes structure. *Picture taken from Ref. [66].*

2.2 Photomultiplier tubes

One of the most common photodetectors used in particle physics is the photomultiplier tube (PMT). It is described in detail in Refs. [66, 67], both used as basis for this section. A typical structure is shown in Fig. 2.3. The photon enters the tube through the entrance window, which can be made of different materials, e.g. lime glass, quartz or beryllium, depending on the spectral range of the incoming photon. After the entrance window, the photon interacts with the photocathode via external photoelectric effect and produces a photoelectron. The electron will then be focussed by an electrode onto the first of several so-called dynodes, which are used to create an avalanche of electrons. Each dynode acts as an electron amplifier. The final signal after the last dynode is read out on the anode.

A high bias voltage (typically several thousand volts) is applied to the full device for electrons' acceleration. Voltage dividers are used to apply the voltage to the photocathode and dynodes. After creation, the photoelectron is accelerated towards the first dynode and creates secondary electrons due to impact ionisation. The secondary electrons are in turn accelerated towards the following dynode, and the process continues until a gain of up to 10^7 is reached [67]. The rise time of a signal pulse is usually in the ns range. The efficiency of a PMT is given by the product of its QE, the collection efficiency and the multiplication probability.

PMTs are widely used as photon detectors in high energy physics (HEP) because of their large active area, high radiation tolerance and low dark noise. Dark noise is the detected current produced in the dark by e.g. thermal electron emission from the photocathodes [67], and the average rate of the detected dark pulses is called dark pulse rate.

One example where PMTs are employed is the LHCb luminosity detector PLUME. The photodetectors are used to detect Cherenkov light produced by particles crossing quartz tablets

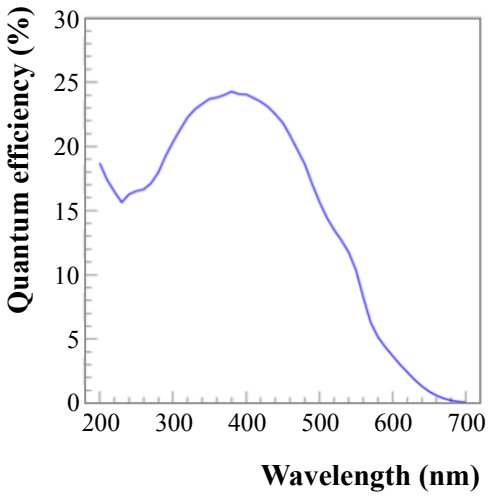

Figure 2.4 – QE of PMT type R760 as function of wavelength. The QE peaks at around 400 nm, and has a QE of 15% for the Cherenkov light emitted by the quartz window in PLUME (below 200 nm). Note that below 200 nm the quantum efficiency is expected to decrease (not increase as is the case in this figure), which has been previously shown in Fig. 2.1. *Data taken from Ref. [33].*

coupled to the PMT quartz entrance window. The light is emitted in the UV-spectrum, where PMTs generally have a relatively high QE. The QE of the R760 PMTs produced by Hamamatsu, which is installed in PLUME, is shown in Fig. 2.4, and exceeds 15% at 200 nm. The PMTs are also sufficiently radiation hard, showing acceptable change in the dark pulse rate at an irradiation with photons up to 200 kGy and with a neutron fluence of 2.7×10^{14} cm^{-2}. The dark pulse rate will still stay below 10 kHz, allowing single photon detection. [33]

A disadvantage of a PMT is the low gain of the first dynode, which introduces statistical fluctuations following a Poisson distribution. Another important factor to consider when using PMTs is their sensitivity to radiation and the accompanying ageing effects, i.e. decrease in sensitivity due to the transmission loss of the entrance window and additional noise production [66]. Both effects are highly dependent on the chosen entrance window material. Additionally, their sensitivity to the magnetic field, their size as well as the complicated mechanical design make solid-state photodetectors often a more favourable option.

2.3 Semiconductors

The bandgap of a material, as shown in Fig. 2.5, determines the conductivity of a material [68]. In a semiconductor, the conduction and valence bands are separated by a bandgap of low value (as compared to insulators), which is for silicon, germanium and gallium arsenide

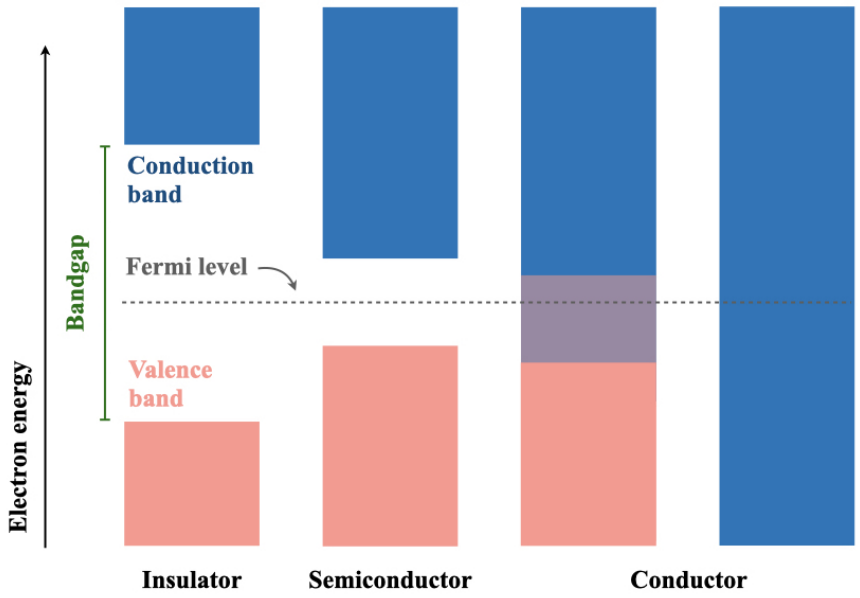

Figure 2.5 – Schematic representation of the band structure of an insulator, semiconductor and a conductor. The Fermi levels for each are indicated.

1.12 eV, 0.66 eV and 1.42 eV at T = 300 K, respectively [69]. The bandgap for insulators like glass is usually much larger and cannot be easily crossed by thermally excited electrons. For conductors like metals the bandgap is non-existent due to the overlapping of the valence and conduction bands, or the highest energy band is only partly filled.

The Fermi level is the highest energy level which electrons can occupy at absolute zero temperature [68]. For semiconductors and insulators it lies in the bandgap, whereas for a conductor it is inside the overlap of conduction and valence band. Typically, the aforementioned semiconductors silicon, germanium and gallium arsenide are used in photodetectors.

2.3.1 p-n junction

The following section is based on Refs. [69–71]. Silicon can be doped to increase the number of free charge carriers. Atoms of the chemical group III are introduced to increase the number of free positive charge carriers (holes). These atoms are called electron acceptors, and create a p-doped silicon. Usual elements to use are boron, aluminium and gallium. To produce negatively (n) doped silicon, atoms from group V such as nitrogen, phosphorus and arsenic are introduced in the lattice structure. These atoms are then referred to as donors, and have an additional free electron in the structure. The free charge carriers for both types of doped silicon (electrons for n-type and holes for p-type) are referred to as majority carriers. Holes

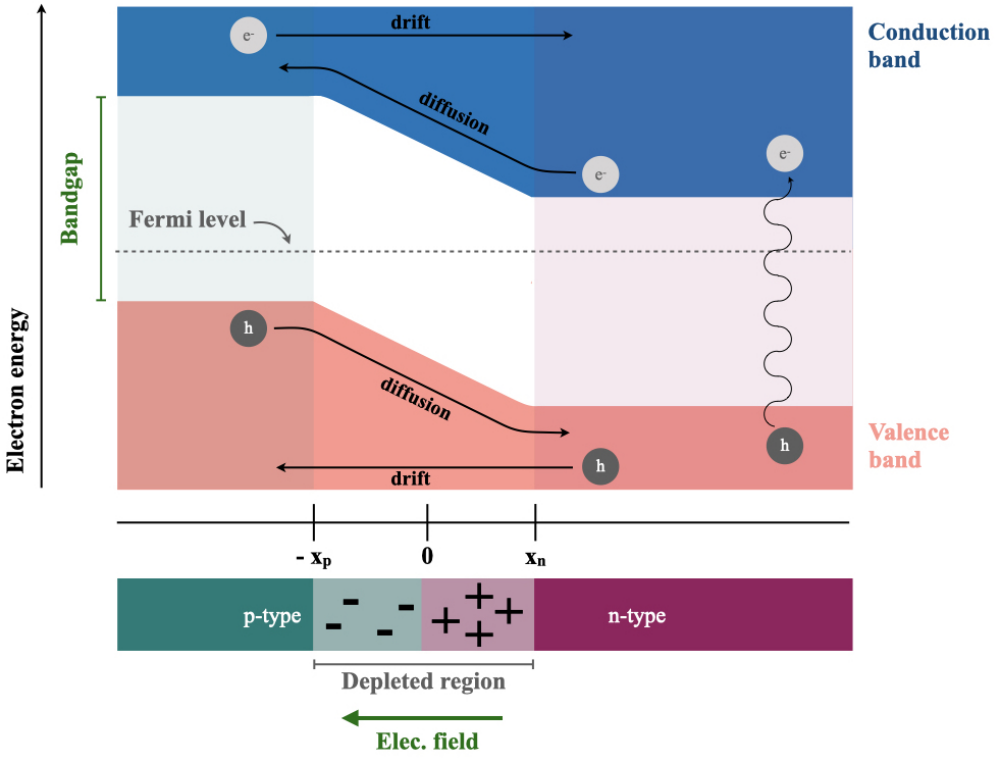

Figure 2.6 – Band structure of a p-n junction at equilibrium. Diffusion and drift currents for electrons (light grey) and holes (dark grey) are shown. A thermally generated electron-hole pair is shown on the right side of the junction. *Picture inspired from Ref. [72].*

in the n-doped and electrons in the p-doped silicon are referred to as minority carriers. Very highly doped materials are denoted by p^+ and n^+.

The Fermi level in the n-doped silicon is close to the conduction band, whereas for the p-doped side it is close to the valence band. If p-type and n-type silicon structures are joined, they form a p-n junction at which the Fermi levels of the p- and n-doped regions will align. This modifies the band structure of the material as shown in Fig. 2.6. Due to the concentration gradient, electrons from the n-type region will diffuse towards the p-doped region, and recombine with holes. The same is happening in the p-type region, with holes diffusing towards the n-side and recombining with electrons. The diffusion process creates ionised atoms at the border, where a negative charge in the p-region and a positive one in the n-region are created. This is known as space charge region or depletion region, which is now depleted of free majority charge carriers.

An electric field is formed as a result of the built up charge distribution in the depletion region. Electrons from the p-side drift towards the n-side and holes to the p-side. The drift current will counteract the diffusion current until they are equal and an equilibrium is reached.

Statistically, as described for example in Refs. [73, 74], some majority carriers will manage to diffuse and will become minority carriers upon crossing the junction. This is why a small diffusion current remains. Minority carriers that reach the junction's edge will drift due to the electric field, which results in a small drift current. At equilibrium, diffusion and drift currents from both electrons and holes cancel each other out.

An applied external voltage can modify the size of the depletion region. When a positive bias voltage is applied between the p-side and the n-side, the depletion region is reduced and the diode is said to be forward-biased. In this state it is easier for electrons and holes to cross the junction from the n-type and p-type, respectively. When the electrons arrive at the junction edge of the p-side, they diffuse towards the other end due to the charge carrier density difference. The same applies for holes on the n-side.

A reverse bias voltage will increase the size of the junction, preventing the diffusion of the majority charge carriers. In this mode, only the minority carriers are able to cross the junction by diffusion and drift across the junction, resulting in a small current. This current is called reverse bias saturation current I_S.

In a first approximation the behaviour of the current of an ideal diode I_D with respect to the applied bias voltage V_D is described by the Shockley equation [71]:

$$I_D = I_S(e^{\frac{qV_D}{nk_BT}} - 1), \tag{2.2}$$

where q is the elementary charge, k_B is the Boltzmann constant, T the temperature and n is the ideality factor (which is 1 for an ideal diode, but is between 1 or 2 in a typical diode). In a reverse biased diode, I_S is one of the components of the so-called leakage or dark current I_{dark}*.

At a high reverse bias voltage V_{bias}, the junction enters into a multiplication mode not described by Eq. 2.2. The high electric field will accelerate the charge carrier so much, that it causes secondary impact ionisation. At a voltage above the so-called breakdown voltage V_{BD} the avalanche is self-sustained.

*Additional parameters of I_{dark} are (band-to-band or trap-assisted) tunnelling current $I_{tunneling}$, and thermal generation and recombination of charge carriers [75].

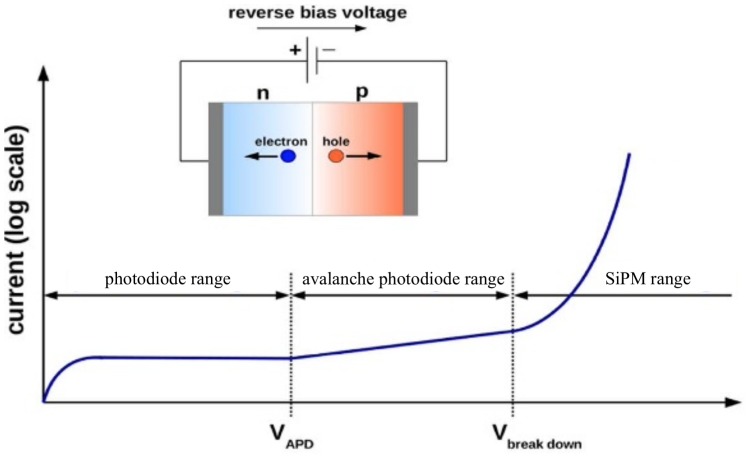

Figure 2.7 – The three operational voltage regimes of a p-n junction under reverse bias. *Picture taken from Ref. [76].*

Depleted p-n junctions are the base of solid-state photodetectors. The different operational regimes of a reverse biased semiconductor photodetector are shown in Fig. 2.7. The regions are named after the most common detectors that operate in these bias regimes, namely the photodiode, avalanche photodiode and SiPM.

2.3.2 PIN-diode

Introducing an additional intrinsic (undoped) or very lightly n^- doped region into the p-n junction improves the photon absorption probability and thus the creation of charge carriers because of the enhanced depletion region that reaches into the intrinsic region. The thick intrinsic region also decreases the diode's capacitance. The structure of a PIN-diode is shown in Fig. 2.8. [57]

When used as photodetectors, PIN-diodes are reversely biased in order to increase the depletion region, for which only a low bias voltage of a few volts is required. They are insensitive to magnetic fields, and show only a small temperature dependence due to the gain being equal to one. However, the signal is very small due to the lack of an amplification region, thus requiring an external amplification. [57]

PIN-diodes are for example used in the BELLE II electromagnetic calorimeter, where they are coupled to CsI crystals and read out the scintillating light produced by charged particles [78].

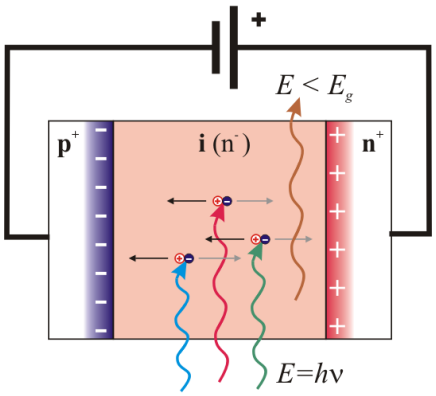

Figure 2.8 – Schematic view of a PIN-diode. *Picture taken from Ref. [77].*

2.3.3 Avalanche photodiode

An avalanche photodiode (APD) has a similar structure to a PIN-diode, but has in addition to the intrinsic region two strongly doped ones (p^+ and n^+) [57]. An incoming photon will create an electron-hole pair in the intrinsic region. The electron is accelerated in the strong electric field, and produces secondary impact ionisation. This results in a gain of up to 1000 is achieved. The structure of an APD is shown in Fig. 2.9. In high energy physics, APDs have been employed in calorimeter read-out systems of crystals (cm^2 size), where a large dynamic range is required. An example where APDs are employed in HEP is the electromagnetic calorimeter of CMS [79]. In general however their strong temperature dependence and radiation sensitivity makes them less attractive than modern SiPMs.

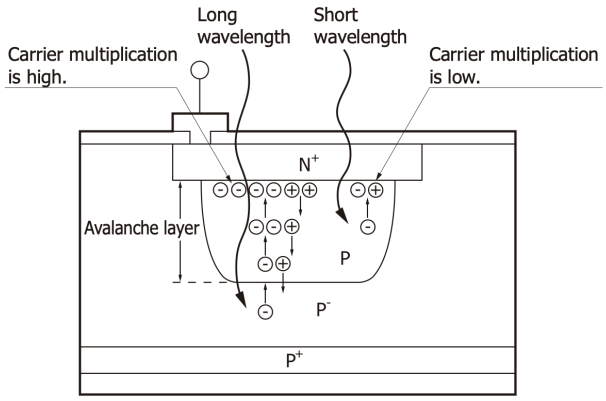

Figure 2.9 – Schematic view of a near-infrared avalanche photodiode. *Picture taken from Ref. [80].*

2.4 Silicon photomultipliers

This section mainly references Refs. [75,76,81,82]. Silicon photomultipliers (SiPMs) work in the non-linear amplification region of a p-n junction, sometimes also denoted as Geiger-Müller region in analogy to gaseous detectors. The photodetectors are pixelised devices, consisting of arrays of single photon avalanche diodes (SPADs) connected in parallel. They are operated in reverse bias with a voltage V_{bias} exceeding the linear amplification region. At the breakdown voltage V_{BD} the avalanche regime changes from the linear to the self-sustaining mode.

In a single SPAD, an arriving photon will create an electron-hole pair, which is accelerated by the high electric field and will trigger an avalanche in the depletion region, creating additional charge carrier pairs along its way. The resulting self-sustaining avalanche has a fast rising current and is only stopped using a technique called *quenching*, by either reducing the voltage across the diode (active quenching) or by limiting the current below a critical value in the order of few µA (passive quenching). In the latter, a serial resistor called the quenching resistor R_{q} is used. The working principle of a SPAD is illustrated in Fig. 2.10. [81,83]

The avalanche process is strongly temperature dependent as the mobility and the ionisation rate of charge carriers decrease with increasing temperature. Therefore a higher electric field is needed leading to an increase of V_{BD} with temperature. The temperature dependence is linear and expressed with a temperature coefficient. The value of this coefficient depends on the SiPM technology, and typical values are in the range of $20-60$ mV/K [76]. Many characteristics of SiPMs depend on the difference of V_{bias} and V_{BD}, which his called the excess bias or overvoltage ΔV:

$$\Delta V = V_{\text{bias}} - V_{\text{BD}} \tag{2.3}$$

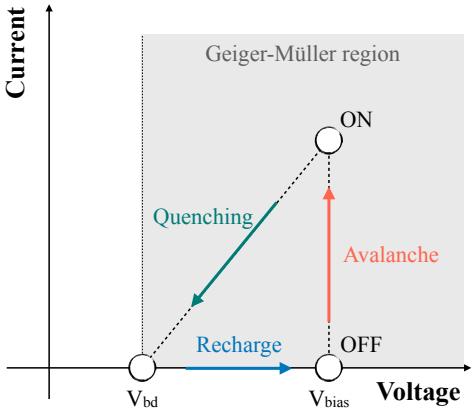

Figure 2.10 – Steady state diagram of a SPAD cell. A photon-induced avalanche results in a current in a cell biased at $V_{\text{bias}} > V_{\text{BD}}$. *Picture inspired from Ref. [83].*

The electrical model

The electronic circuit of a SPAD is shown in Fig. 2.11. As a current is only produced when a photon is absorbed, the state of the diode can be represented by an electrical switch. When the switch is open, the diode capacitance C_d is charged to the applied reverse bias V_bias. Once a photon is absorbed, the switch is closed. The consequent current produces a voltage drop on R_q, which reduces in turn the voltage across the diode. The diode capacitor C_d is discharged by the diode resistance R_d until V_BD is reached. In modern SiPM cells a capacitor C_q is introduced bypassing R_q to allow for a fast signal pulse. This results in a pronounced fast component of the pulse shape. The discharge time τ_d is then given by:

$$\tau_\mathrm{d} = R_\mathrm{d} \cdot (C_\mathrm{d} + C_q). \tag{2.4}$$

The discharge time corresponds to the rise time of the signal with the current following $1 - \mathrm{e}^{-\mathrm{t}/\tau_\mathrm{d}}$. Once the avalanche is quenched, the switch is reopened. Quenching occurs at the so-called latch current $I_\mathrm{latch} = (V_\mathrm{bias} - V_\mathrm{BD})/(R_\mathrm{q} + R_\mathrm{d})$. Typically in a passive-quenching circuit, the avalanche is terminated when a current of approximately 20 µA is reached [84]. As the current drops, the voltage across R_q reduces, and the C_d is recharged through R_q to V_bias once the recovery is complete. The recovery time τ_rec of the SPAD can thus be calculated with:

$$\tau_\mathrm{rec} = R_\mathrm{q} \cdot (C_\mathrm{d} + C_\mathrm{q}) \,. \tag{2.5}$$

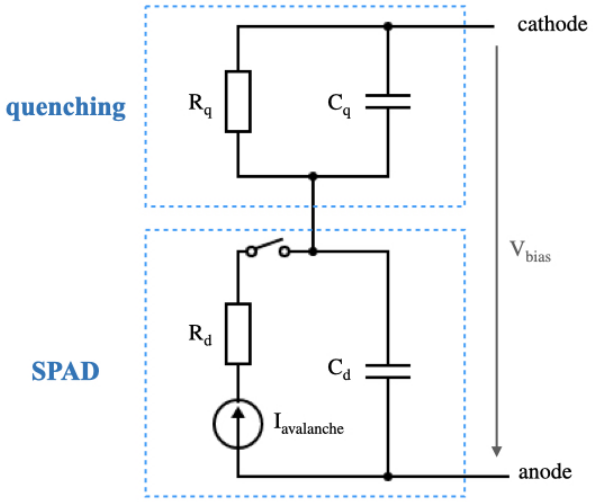

Figure 2.11 – The electronic circuit of a SPAD (single SiPM cell). *Picture inspired by Ref. [81].*

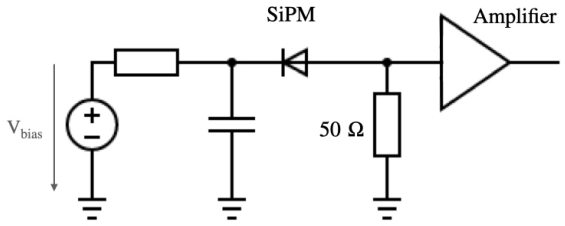

Figure 2.12 – SiPM readout scheme. The SiPM, illustrated by the photodiode, is connected to a filtered power supply and a readout amplifier.

The current decreases exponentially with $e^{-t/\tau_{rec}}$. Figure 2.12 shows how a SiPM with one channel (SPAD) is attached to a readout amplifier.

A SiPM is made up of many SPAD cells, i.e. APD in Geiger-Müller mode, connected in parallel, with the corresponding electronic circuit shown in Fig. 2.13. The signal of a SiPM is characterised by its rise time (typically of the order of a ns), and the fast and slow part of the recovery time. The fast signal discharge is determined by the product of the load resistor R_L and the total capacitance of N_{tot} cells $C_{tot} = N_{tot} \cdot (C_d + C_q) + C_g$, with C_g being the grid capacitor resulting from pixel connectors. The fast component is:

$$\tau_{fast} = R_L \cdot C_{tot}\,. \tag{2.6}$$

The slow component is given by the full recharge of the capacitors C_d and C_q through R_q in the active pixel(s), and therefore $\tau_{slow} = \tau_{rec}$. When the SiPM is connected to the readout electronics, a parasitic serial inductor L_p can cause a ringing effect in the slow component of the signal. A typical SiPM waveform is shown in Fig. 2.14 showing the fast and slow component of the signal.

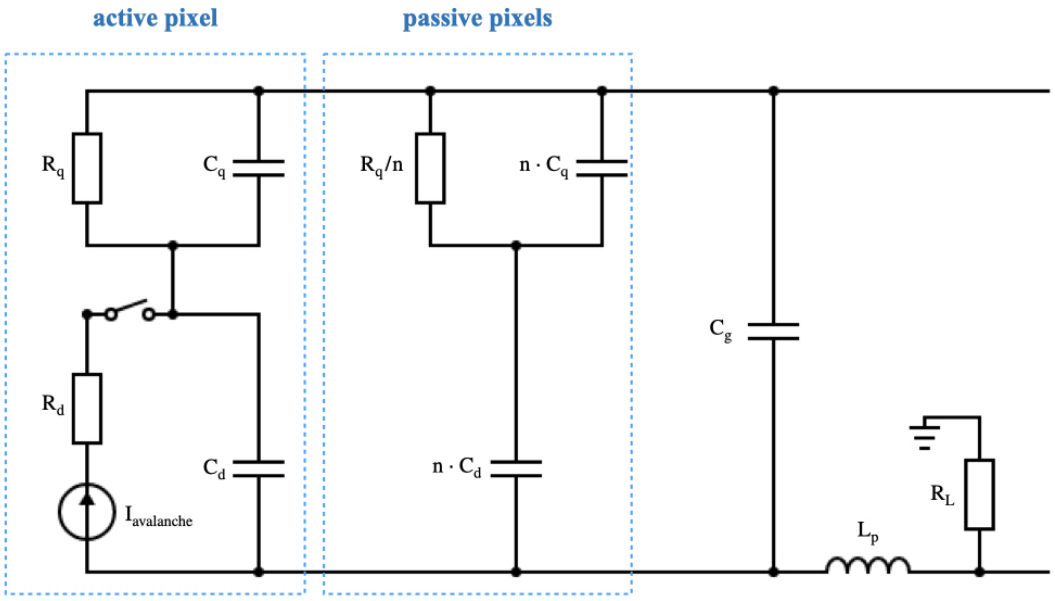

Figure 2.13 – The electrical circuit of a SiPM array for one active and n passive pixels. The total number of cells is given by $N_{tot} = n + 1$. *Picture inspired from Ref. [76].*

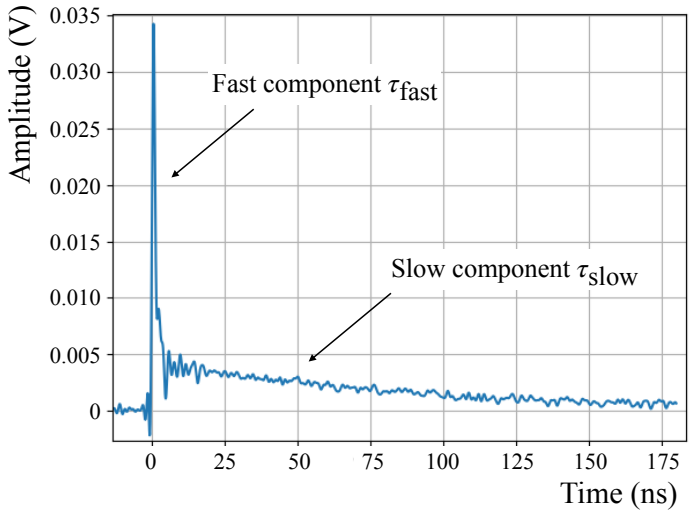

Figure 2.14 – A typical waveform recorded with an oscilloscope of a SiPM used in the LHCb SciFi Tracker. The fast and the slow component of the recovery time are indicated. The ringing in the slow component is caused by the Kapton flex cable, which is used to connect the SiPM to the readout electronics.

2.4.1 Gain

The gain (G) of a SiPM pixel is equal to the number of charge carriers created in an avalanche process, and the charge Q is given by $Q = G \cdot e$, where $e = 1.602 \times 10^{-19}$ C is the elementary charge. The transported charge corresponds to the reduction of the voltage on C_d by ΔV, and the gain can then be expressed by:

$$G = \frac{(V_\mathrm{bias} - V_\mathrm{BD}) \cdot C_\mathrm{d}}{e} = \frac{\Delta V \cdot C_\mathrm{d}}{e}. \tag{2.7}$$

The gain can also be written using the latch current I_latch and $\tau_{rec} \approx C_\mathrm{d} \cdot R_\mathrm{q}$:

$$G = \frac{I_\mathrm{latch} \cdot \tau_\mathrm{rec}}{e}, \tag{2.8}$$

From Eq. 2.7 it follows that the gain is in general linearly dependent on the overvoltage. However, for some devices a progressive depletion of the epitaxial layer (beneath the p-n junction) can occur, causing a deviation in the linear behaviour [81]. In the operation region of the detectors studied in this work, a linear behaviour of the SiPMs has been verified.

In reality, the gain is determined by the bandwidth and shaping time of the front-end electronics. In the LHCb SciFi Tracker, a portion of the slow part of the signal is not integrated due to the fast shaping time (~ 20 ns) and a slow component cancellation circuit (pole-zero), effectively reducing the gain. Note that for fast shaping times a high signal-to-noise ratio is difficult to achieve.

The gain can be determined by measuring the delivered charge of a signal produced by a single photon $G = \int I \, \mathrm{d}t/e$. The delivered charge is determined by numerical integration of the voltage pulse measured on an oscilloscope. This leads to the relation

$$G = \frac{1}{R_\mathrm{load} \cdot G_\mathrm{amp} \cdot e} \cdot \int U \, \mathrm{d}t, \tag{2.9}$$

where R_load is the input impedance of the pre-amplifier and G_amp the pre-amplifier gain. The pre-amplifier is necessary to optimise the amplitude resolution of the oscilloscope in the required dynamic range. This gain measurement is performed for several bias voltages and the linear fit allows to determine the V_BD and $\mathrm{d}G/\mathrm{d}V$. This method is used with low-intensity light pulses. Note that the numerical integration and G_amp depend on the pulse shape (bandwidth, sampling rate), and will lead to small differences.

A different method is to calculate the gain from a measured dark current I_{dark} and the measured DCR:

$$I_{\text{dark}} = \text{DCR} \cdot G \cdot e. \tag{2.10}$$

Also this method has some limitations. It is crucial to correct the DCR by the contribution of the direct crosstalk probability and afterpulse, which are explained in detail in Sec. 2.4.3.

Finally, the gain can also be obtained by determining the distance between photon peaks in a charge spectrum recorded by an integrating charge sensitive amplifier. This method is described in Sec. 5.4.2.

2.4.2 Photon detection efficiency

The photon detection efficiency (PDE) is the ratio of the detected number of incoming photons to the total number of photons. For SiPMs, the PDE can be expressed by the product:

$$\text{PDE} = \text{QE} \cdot P_{\text{avalanche}} \cdot \text{GFF}. \tag{2.11}$$

QE is the quantum efficiency and depends on the wavelength λ of the incoming photons. It represents the probability that the photon generates an e-h pair in the depletion region. GFF is the geometrical fill factor, i.e. the ratio between the active and total detector surface. It depends on the pixel layout, and will vary with the implementation of R_{q}, insulation trenches and electrical routing. In general, it is higher for larger pixels. Finally, $P_{\text{avalanche}}$ is the probability that an e-h pair produces an avalanche. It depends on the electric field and is thus a function of V_{bias}. At high overvoltages $P_{\text{avalanche}}$ saturates because of the saturation of the charge carrier ionisation rate. The effect can be observed as a plateau at the PDE graph at high ΔV shown in Fig. 2.15.

The silicon layers of a SiPM can be customised to optimise its efficiency to the incoming photon's wavelength, as shown in Fig. 2.16. The longer the wavelength, the further it will travel in the silicon until it interacts. Therefore, photons in the blue region will interact close to the surface, whereas photons with a longer wavelength will interact much deeper inside the silicon. Additionally, as electrons have a higher ionisation probability than holes, it is more efficient for the photon to interact in the p-doped layer. This results in a n-on-p structure for green and red photons, whereas a p-on-n structure is favoured for photons in the blue and UV regime. [86]

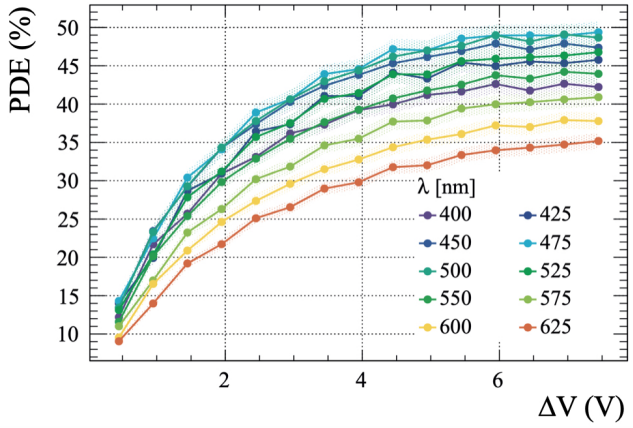

Figure 2.15 – The PDE of a SiPM used in the LHCb SciFi Tracker. The PDE saturates at $\Delta V = 6\,\mathrm{V}$ for a wavelength of $\lambda = 475\,\mathrm{nm}$. *Picture taken from Ref. [85].*

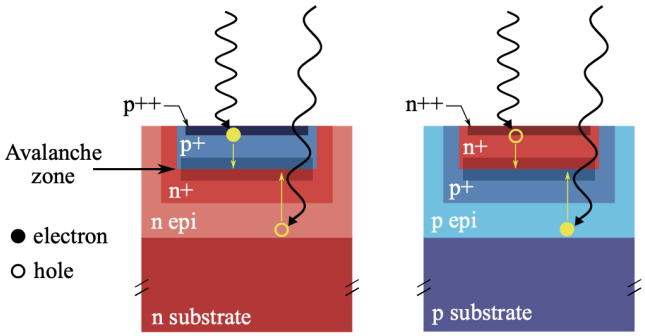

Figure 2.16 – The structure of the p-n junction determines the efficiency of the SiPM to the incoming photon. On the left, a SiPM for efficient blue light detection is depicted, whereas the SiPM on the right is efficient for red light detection. *Picture taken from Ref. [85].*

2.4.3 Noise in a SiPM

A SiPM pixel can be triggered not only by an impinging primary photon, but also by e.g. secondary photons or trapped charges. Two different types of noise can be distinguished: primary dark noise also called uncorrelated noise, and correlated noise.

Dark noise

Primary dark noise counts are random signals, where an avalanche is triggered by thermal excitation of a charge carrier, by (trap assisted or band-to-band) tunnelling, or by diffusion

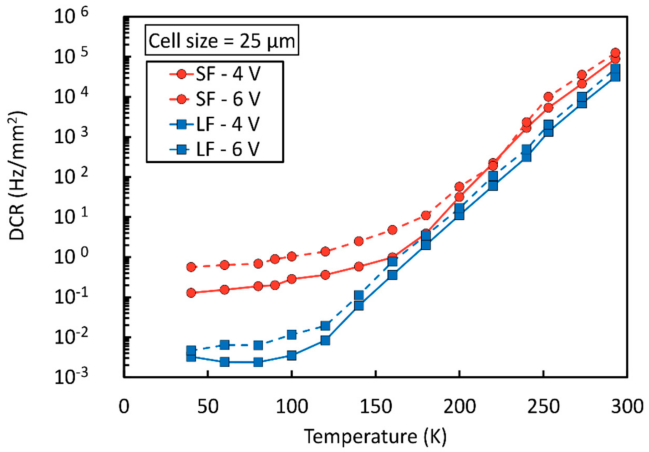

Figure 2.17 – DCR as a function of the temperature at two values of overvoltage for two SiPM technologies by FBK. SF (LF) refers to a SiPM with a standard (low) electric field in the near-ultraviolet high-density (NUV-HD) technology implementation. *Picture taken from Ref. [88].*

from the bulk region. The produced signal is uncorrelated to any photo-induced signal and the amplification process is the same, thus dark pulses cannot be distinguished from signal. Dark count pulses are distributed in time according to Poisson statistics. They are used to characterise SiPMs, e.g. measuring gain, correlated noise and V_{BD}.

The dark count rate (DCR) is strongly temperature dependent. At room temperature, dark noise charge carriers are dominantly produced by lattice defects and impurities in the silicon, which introduce intermediate energy levels and reduce the required energy to reach the conduction band. This is described by the Shockley-Read-Hall (SRH) mechanism [87]. At lower temperatures, tunnelling effects become dominant, and are especially important for cryogenic applications. At temperatures below 150 K, the DCR reduction is less pronounced, which can be seen for SiPMs produced by FBK in Fig. 2.17.

The DCR is proportional to the active area and is linearly dependent on ΔV for a limited range. At high ΔV, the DCR increases quadratically due to increase of correlated noise probabilities [75].

Correlated noise

Pulses that are correlated to a primary avalanche are called correlated noise. They are divided in direct crosstalk (DiXT), delayed crosstalk (DeXT) and afterpulse (AP). An illustration of the three different types of correlated noise is shown in Fig. 2.18.

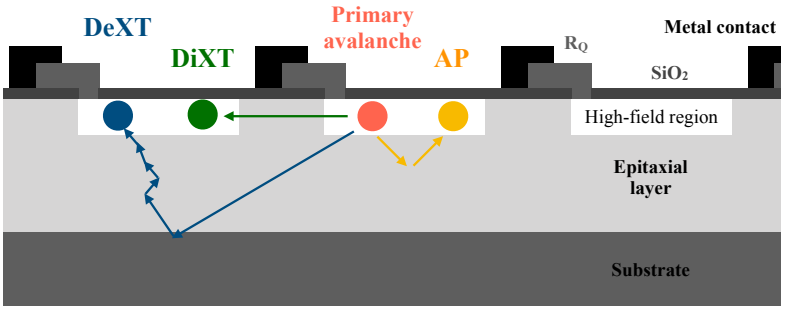

Figure 2.18 – The different types of correlated noise caused by a primary avalanche event. Direct crosstalk (DiXT), delayed crosstalk (DeXT) and afterpulse (AP) are shown. *Picture inspired by Ref. [89].*

- **Direct crosstalk:** The avalanche in a pixel emits infrared photons by interband recombination or transitions [90]. These photons have a low absorption coefficient in silicon and can therefore travel over a large distance. Optical opaque trenches are commonly implemented in large devices to absorb these photons. The number of produced photons in a pixel is proportional to the gain of the pixel. Thus also the probability of these photons triggering another pixel is proportional to G. The time delay between the two avalanches is given by the travel time of the infrared photon (< 1 ps) and the drift time of the produced e-h pair towards the amplification region, and is typically below 1 ns. This can be seen in Fig. 2.19a. The peak amplitude of the signal can be between 1 and 2 PE, depending on the arrival time.

- **Delayed crosstalk:** If the produced infrared photon is absorbed in the silicon substrate, the minority carrier will drift into the depletion region, starting an avalanche in another pixel. This is called delayed crosstalk. An alternative process of DeXT is the production of a free charge carrier by the drifting charge liberated by a primary avalanche. Both of these processes result in a signal delayed by a few tens to hundreds of ns as shown in Fig. 2.19b. In general, DiXT and DeXT events can be distinguished by their time delay. The peak amplitude of a DeXT event is 1 PE.

- **Afterpulse:** Charge carriers released by an avalanche can be trapped by impurities or lattice defects in the silicon. These carriers are released only after a delay, and produce a second avalanche in the same pixel. The time delay between primary and the afterpulse is typically a few hundreds of ns. This is illustrated in Fig. 2.19c. The AP amplitude is between 0 and 1 PE, depending on the recharge state of the pixel. AP can also occur due to incomplete quenching of the avalanche. This leaves free charges in the avalanche region producing AP. Incomplete quenching limits the stable operation range of a SiPM, especially at high ΔV.

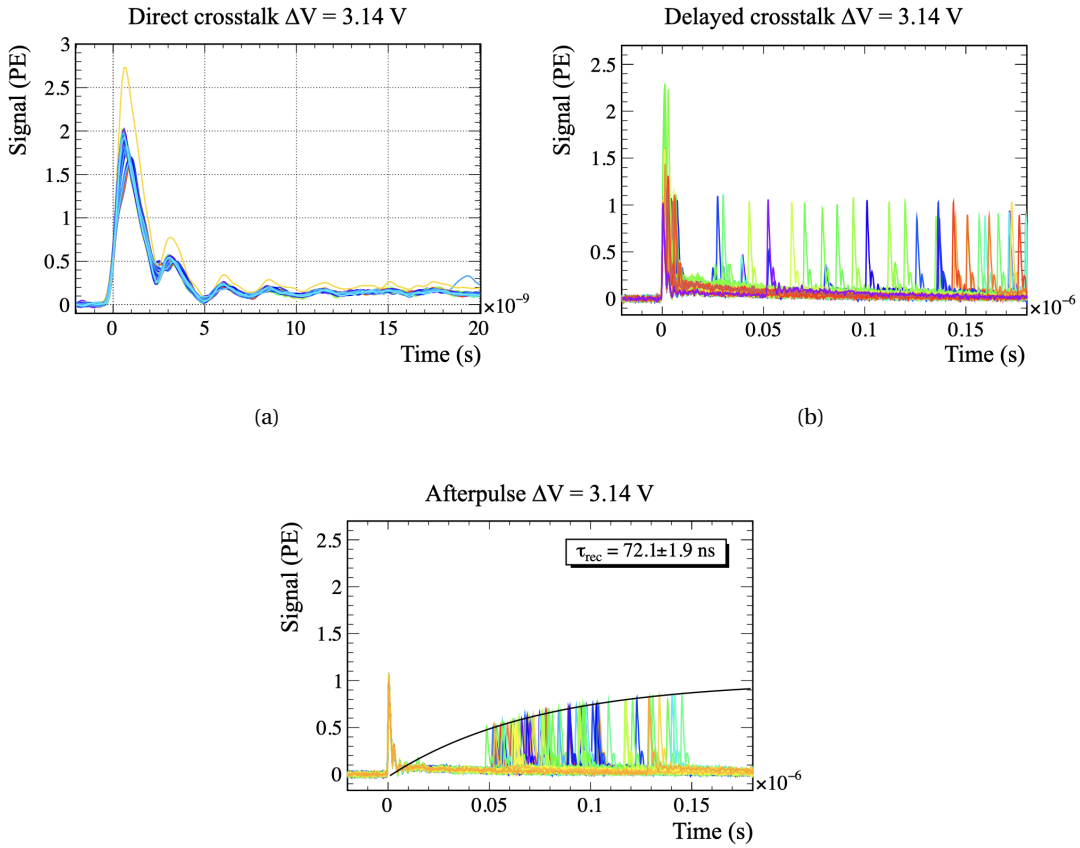

Figure 2.19 – Three types of correlated noise measured with a NUV-HD device by FBK. The waveforms were recorded with an oscilloscope. DiXT is shown in (a), where one event with an amplitude bigger than 2 PE can be seen, which corresponds to two DiXT pulses. The ringing between 2 and 5 ns is due to the electronic connector (Kapton flex cable). In (b) DeXT events are shown, where some are secondary crosstalk caused by a primary event with DiXT. Events with AP are depicted in (c). The exponential fit over the afterpulse amplitude returns the recovery time of the pixel.

The excess noise factor (ENF) is the ratio between the total number of detected output pulses and the single input signal. At the breakdown voltage the ENF is typically equal to one, and increases with higher overvoltage. For SiPMs with low correlated noise, the ENF remains close to one [76]. The excess charge factor (ECF) describes the additional charge produced by correlated noise, and is given by the average of the measured charge divided by the average charge produced by the primary pulse. ENF and ECF are equal when the total noise is only made up of crosstalk, i.e. DiXT and DeXT. If there is also AP occurring, the ECF diverges at high ΔV while the ENF remains proportional to the AP. The ECF can hence be considered an approximate upper limit for the ENF [91]. Equation 2.10 can be rewritten with ECF to:

$$I_{\text{dark}} = e \cdot G \cdot \text{ECF} \cdot \text{DCR}. \tag{2.12}$$

2.4.4 Timing performance

SiPMs have become widely used in particular because of their excellent time resolution. A good timing is for example important in time-of-flight positron emission tomography (TOF-PET) [82,92], tracking in particle detectors to speed up the search algorithm, and light detection and ranging (LiDAR) applications in the automotive sector [93, 94].

The single photon time resolution (SPTR) of a SiPM is the width of the distribution of the time interval between a trigger and the detection of the signal. It is caused by the jitter, i.e. fluctuation, of the detection time of the signal, which is dependent on the system components, e.g. electronics, light source and data acquisition system. The SPTR has an impact on the achievable time resolution of a whole detector system, influencing also directly the coincidence time resolution (CTR), which is the time resolution of a true coincidence event measured by two SiPMs. Therefore it is important to decouple the intrinsic SPTR for a measured SiPM. The SPTR is typically measured with a pulsed laser, where the laser trigger is used as start signal. Figure 2.20 shows the result of an intrinsic SPTR evaluation of several SiPMs by different manufacturers, reported in Ref. [95]. Intrinsic SPTR values reach from 70 ps FWHM for the FBK NUV-HD device to 130 ps FWHM for the Hamamatsu HPK S13360-3050 at ΔV = 5 V.

To determine the CTR, two SiPMs of the same type are usually coupled to a plastic scintillator or a crystal (e.g. LYSO). The leading edge of the first arriving photon (or of a higher threshold) is determined for both, and the difference between the two time measurements is plotted. The width (FWHM) of the distribution is equal to the CTR. As described in Ref. [96], the CTR depends on the rise time τ_{r} and decay time τ_{d} of the scintillator, on the number of photons

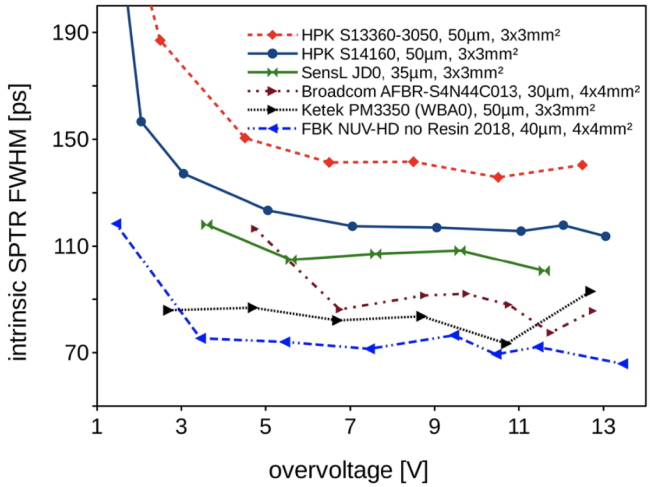

Figure 2.20 – Intrinsic SPTR of different SiPMs. *Picture taken from Ref. [95].*

detected N_{ph} and the time variance of the i-th emitted photon var(i):

$$\text{CTR} = 3.33 \cdot \sqrt{\text{var(i)} \cdot \frac{\tau_\text{r}\tau_\text{d}}{N_\text{ph}}}. \tag{2.13}$$

The factor 3.33 comes from the transformation of the standard deviation into the full width at half maximum in coincidence $2 \cdot \sqrt{2 \cdot \ln(2)} \cdot \sqrt{2}$. For the first arriving photon, Eq. 2.13 simplifies to:

$$\text{CTR}_{\text{1st ph}} = 2.18 \cdot \sqrt{\frac{\tau_\text{r}\tau_\text{d}}{N_\text{ph}}}. \tag{2.14}$$

2.4.5 Radiation damage of SiPMs

This section is largely based on Ref. [40]. As briefly mentioned in Sec. 1.3, radiation damage in a semiconductor can be caused by two processes: NIEL and IEL. NIEL damages the crystalline structure of the silicon, mostly important for the noise induced avalanche generation in the pre-amplification region, whereas IEL causes mostly surface damage in the silicon-oxide (SiO_2) layer and at the interface SiO_2-Si. The focus of the following sections will be on the radiation damage induced by neutrons, protons and X-rays.

IEL-induced surface damage

Photons and charged particles (typically with an energy below 300 keV [40]) can ionise the atoms in the SiO_2 layer and the SiO_2-Si interface region. The electron diffuses (when no electric field is present) or drifts (with electric field) into the SiO_2 layer, where charges are accumulated. At the SiO_2-Si interface layer, deep traps are generated, where holes are prone to be trapped. When the SiO_2-Si interface is depleted, additional surface currents are produced, which increase the dark current.

As stated in [40], IEL-induced radiation damage was studied exposing a device to high-energetic X-ray radiation (20 MGy). The dark current increased due to the higher surface current by three orders of magnitude (below breakdown), while the DCR (above breakdown) increased by only one order of magnitude. The difference in dark current and DCR can be explained by the fact that only a fraction of the produced surface current reaches the amplification region.

NIEL-induced bulk damage

High energy charged particles, high energy photons (gammas) and neutrons can cause damage in the silicon lattice by displacement of an atom. This is called NIEL damage. The minimum energy required to displace an atom in silicon amounts to 25 eV. Electrons will mainly produce point defects while neutrons and high-energetic particles can produce point as well as cluster defects.

One of the effects common to radiation-induced bulk damage is the increase in leakage (below V_{BD}) and dark current (above V_{BD}). This is caused by new energy levels with an energy close to half the bandgap energy, at which charge carriers can easily reach the conduction band already at room temperature. The leakage and dark currents are either produced by the diffusion of minority carriers into the depleted region, by the creation of charge carriers due to defects or, at high electric fields, by band-to-band or trap-assisted tunnelling. The dark current can be reduced by a factor two for every ten degrees of cooling (reported e.g. in Ref. [97]). At temperatures below 100 K, the DCR saturates and is dominated by band-to-band or trap-assisted tunnelling.

Another common result of radiation damage is the decrease of the charge collection efficiency, caused by additional trapping centres that have a long de-trap time, thus part of the charge carriers are lost for the signal. Finally, in low-doping concentration regions (typically for silicon strip detectors), a change in effective doping concentration caused by defect states can occur. At higher levels of irradiation ($> 10^{12}$ 1 MeV n_{eq}/cm^2) this can have an impact on the electric field in the amplification region of a SiPM.

Irradiation with high-energy photons, electrons and positrons: Photons with an energy higher than 300 keV can produce surface as well as bulk damage, and similar effects are expected from electrons and positrons with energy > 300 keV. A SiPM shows a significant increase in DCR when irradiated with gammas up to 1 kGy. At a dose higher than 1 kGy, a distinction of single photo-electron peaks is no longer possible at room temperature. Tests with electrons and positrons (reported in Refs. [98, 99]) also show an increase in DCR, without impacting the PDE.

Irradiation with hadrons: At hadron irradiation up to a level of $\Phi_{eq} \approx 2 \times 10^{12}$ 1 MeV n_{eq}/cm^2 PDE, crosstalk and AP remain the same, whereas the DCR is dramatically increased. This is the expected level for SiPMs in the SciFi Tracker at LHCb Upgrade II. At higher fluences up to $\Phi_{eq} = 2 \times 10^{14}$ 1 MeV n_{eq}/cm^2, the SiPM current can reach a level where the dark current leads to power dissipation in the form of self-heating. The measurement of gain, PDE and crosstalk becomes difficult due to self-heating, a change in V_{BD} and DAQ saturation. In general, thinner avalanche regions show a less significant shift in V_{BD}. At this level of irradiation, R_q implemented in poly-silicon shows a high fluence dependency, whereas for thin films (used by Hamamatsu) this is not expected.

2.4.6 Implications on future SiPM developments

One of the biggest challenges is the increasing DCR with the high radiation exposure. Operating the SiPMs at cryogenic temperatures decreases the DCR by several orders of magnitude, which is at the current state the most effective countermeasure to the increase in DCR. All experiments with radiation exposure will have to evaluate the operation temperature. For IEL-induced radiation damage, another possibility is to limit the surface current from reaching the multiplication region by careful surface design. For NIEL-induced damage the reduction of the diffusion from the non-depleted substrate and a field-shaping of the depletion region can minimise the DCR.

PDE is reduced by the high pixel occupancy after high radiation exposure. The problem can be mitigated by smaller pixels to increase the cell density. This reduces the cell capacitance, which has a positive effect on the recovery time, gain and crosstalk. However, as small cells have a lower GFF, this compromises the PDE. A method on how to achieve small pixel sizes and at the same time a high PDE is described in this thesis in Chapter 4. Microlenses at the pixel level can be used to deviate the light from the dead to the active area, increasing the effective GFF, as is one goal of this thesis.

Current manufacturers

Three companies have provided SiPMs for LHCb SciFi R&D in the past years, namely Hamamatsu (Japan), FBK (Italy) and Broadcom (US), previously KETEK (Germany). Hamamatsu and KETEK have both produced SiPM prototypes for the SciFi Tracker for Run 3. After an extensive evaluation procedure the customised photodetectors by Hamamatsu (referred to as H2017 or via Hamamatsu internal ID S13552) were chosen for production.

One of the biggest challenges for future applications of SiPMs in HEP is the photodetectors' tolerance to radiation. FBK is evaluating customised SiPM designs for improving the radiation hardness, actively studying the changes in characteristics caused by radiation damage of different particles.

A possibility to cope with the increase in DCR caused by high radiation exposure is to cool the photodetectors down to cryogenic temperatures (< 100 K). Until the dedicated technologies for cryogenic temperatures were developed, the SiPM operation range was limited by the high AP at low temperatures (below 150 K). FBK has produced NUV SiPMs for the DarkSide-20k experiment [100], which are planned to be operated at 87 K, as well as VUV SiPMs developed for a potential use at the nEXO experiment [101]. The low afterpulse probability is achieved by dedicated electric field engineering. For the LHCb SciFi Tracker, the NUV samples of FBK provide a good base for future R&D efforts due to the emission spectrum of the fibre. Hamamatsu has also developed SiPMs with VUV-technology (down to 120 nm) for experiments which employ liquid argon or xenon to detect Cherenkov radiation (e.g. MEG II [102]).

For several years, isolation trenches are added mainly for large pixels (> 25 µm) to reduce pixel-to-pixel crosstalk with a reduction of PDE as a consequence. The trench technology has been greatly improved, where a collaboration between FBK and Broadcom has successfully produced a novel metal-in-trench (MT) technology [103], efficiently reducing crosstalk. The disadvantage of the GFF decrease and the accompanying reduction of the PDE is overcome by the improved characteristics of low crosstalk, bringing the option of a higher ΔV and increasing the operational range.

For future R&D efforts of the LHCb SciFi, FBK has provided SiPMs for the first tests of microlens-enhanced SiPMs (explained in Chapter 4), and has also produced in 2022 a prototype of customised SiPM arrays that combines the MT technology with optimised cryogenic temperature technology (detailed in Sec. 6.2).

3 Scintillating Fibre Tracker for LHCb

The Scintillating Fibre (SciFi) Tracker was installed during the Long Shutdown 2 (LS2) as the new downstream tracker in the LHCb experiment. 11 000 km of scintillating fibres are grouped together into three detector stations, and are read out by 4096 SiPM arrays. It is the first time this type of technology is employed on such a large scale, covering a total of 340 m^2 active detector area, and in such a harsh radiation environment. This chapter is based on the technical design report in Ref. [28], which describes the SciFi Tracker in detail.

3.1 Requirements and implementation

The SciFi Tracker was designed with the following requirements:

- **Efficiency and noise:** The hit detection efficiency is the most important quantity for the overall tracking efficiency. A high hit detection efficiency requires a sufficiently high signal, which is closely linked to the material budget. Additionally, the noise cluster rate should be below 10% of the signal cluster rate to limit the number of ghost hits. A higher noise cluster rate increases the occupancy, and therefore the track reconstruction time. This lead to an implementation with a 95% efficiency at the end of the lifetime of the detector at the worst location. The inefficiency due to the dead time of the pixels is below 1.6% [97].

- **Material budget:** The material budget (X/X_0) is an important characteristic of every tracking detector. Lightweight support structures and thin detectors are required to avoid multiple scattering and the production of secondary particles inside the tracker. The material budget for the current implementation is below 1% per layer. Secondary particles generate approximately 60% of the SciFi hits.

- **Resolution:** The single hit spatial resolution in the horizontal bending plane should be better than 100 µm, whereas a 1 mm resolution in the vertical y direction is sufficient. The fibres are mostly vertical to achieve the resolution in the horizontal x direction. Stereo angles are used to reach the resolution in the vertical direction.

- **Electronics:** The front-end electronics is designed to readout the detector at the bunch crossing rate of 40 MHz. A zero-suppression algorithm, based on SiPM channel clustering (explained in Sec. 3.5), is reducing the data rate and allows for a compact data format for transmission to the event building PCs located on the surface.

- **Radiation tolerance:** The SciFi Tracker has to withstand a total integrated luminosity of 50 fb^{-1} over the course of the Run 3 and 4 data–taking periods. This means that the fibres close to the beampipe have to withstand an ionising dose of 35 kGy, whereas the SiPMs outside of the acceptance region will receive an ionising dose of 50 Gy and a neutron fluence up to 4.1×10^{11} 1 MeV $\text{n}_{\text{eq}}/\text{cm}^2$. The highest ionising dose for the fibres is around the beampipe in the first station (T1), whereas the highest neutron fluence is expected at the SiPM position in the central part of the third station (T3) closest to the calorimeters.

3.2 Tracker design and technology

With these constraints, the tracker was designed as follows: twelve planes of SciFi mats are grouped into three detection stations shown in Fig. 3.1a. Every station has four layers (x-u-v-x), perpendicular to the beam axis z and with vertical fibres tilted by $0°, +5°, -5°, 0°$, respectively. The x-layers provide a single hit spatial resolution below 100 µm, whereas the two stereo layers (u and v) give a resolution in y of about 1 mm. As the tracking is dominated by multiple scattering in the upstream subdetectors a better resolution is not required.

A fibre mat is composed of six layers of staggered scintillating fibres of type SCSF-78MJ produced by *Kuraray* [104]. The emitted scintillating light, which is peaking in the blue spectral region, is detected on one end of the fibre mat outside of the acceptance region by SiPMs (referred to as H2017) by Hamamatsu. A mirror is placed on the other side to increase the detected light. The photodetectors are optimised to have high photon detection efficiency (PDE), low correlated noise and the best achievable dark count rate (DCR) performance after irradiation.

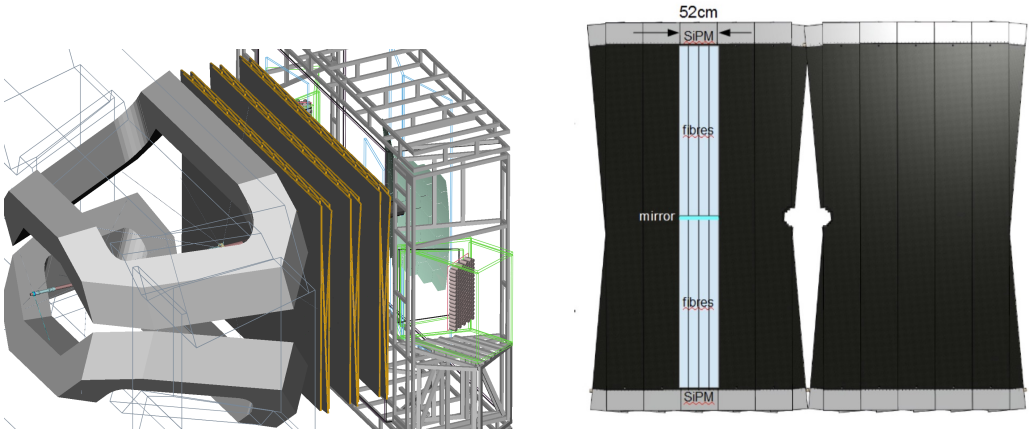

(a) (b)

Figure 3.1 – The three SciFi stations in between the dipole magnet and the RICH2 detector (a) and the front view of one SciFi station (b). *Pictures taken from Refs. [28] and [105].*

3.2.1 Working principle

The typical signal of a fibre tracker module is illustrated in Fig. 3.2. When a charged particle traverses the fibre mat, it deposits (ionising) energy along its trajectory, and creates photons in several fibres. The photons, that are emitted within the acceptance angle described in Sec. 3.3, travel along the fibre to the photodetectors. The photons are then detected by several pixels. The signal is distributed across several channels, and neighbouring channels are grouped into so-called clusters. Clusters represent the particle's position and provide amplitude-time information in a tracking layer. In the clustering algorithm, described in detail in Sec. 3.5, the signal amplitude is compared against three thresholds: seed, neighbour and high. In the SciFi Tracker a typical cluster size is 2–3 channels. The mean cluster position $\overline{x}$ can be calculated as the weighted mean position of the channel position x_i and the signal amplitude s_i for every i channel of the cluster:

$$\overline{x} = \frac{\sum (x_i \cdot s_i)}{\sum s_i}. \tag{3.1}$$

The weights used in the cluster algorithm are proportional to the mean charge of the signals that pass that threshold. The cluster sum is the sum of the total photoelectron (PE) signal inside a cluster $\sum s_i$. The most probable value (MPV) of its distribution, which follows a Landau distribution, gives the light yield (LY) of the tracker. The light yield can also be understood as the total number of detected photons per SiPM cluster for a minimum ionising particle traversing the fibre mat perpendicularly.

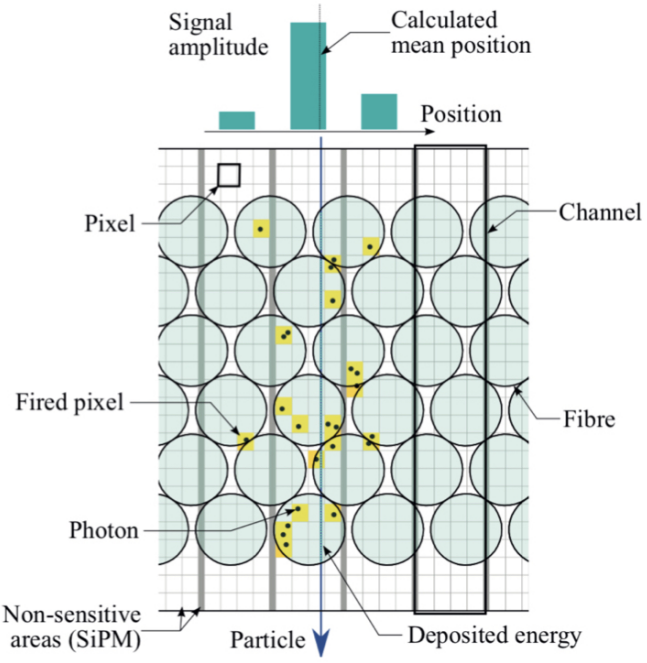

Figure 3.2 – A GEANT4-simulated event of an ionising particle traversing a six-layer fibre mat. The clustering of the SiPM channels with fired pixels, represented as yellow squares, along the particle's trajectory is shown on the top. *Picture taken from Ref. [85].*

The light yield is influenced by the thresholds set for the clustering algorithm. Thresholds which are chosen too high can cause inefficiencies in the tracking performance as low-light clusters might be removed. At the same time, the thresholds have to be sufficiently high to suppress noise cluster. Noise clusters can be produced by correlated noise in the SiPM or, at a sufficiently high DCR, by randomly overlapping dark pulses, which is especially critical for irradiated photodetectors. The right balance between noise suppression and detector efficiency is one of the most crucial operating elements of the SciFi Tracker.

3.3 Scintillating fibres

The plastic optical fibre SCSF-78MJ by Kuraray is a double-cladded fibre emitting scintillating light in the blue spectral region as seen in Fig. 2.2. The emission of scintillating light happens in a multi-step process shown in Fig. 3.3. When an ionising particle crosses the fibre, it excites a molecule of the polymer core, which is made of > 98% of polystyrene (PS). The activator p-Terphenyl (PTP) is added (1 – 2% by weight) to couple to the PS via exchange of a virtual photon. Like this, the de-excitation process happens via non-radiative dipole-dipole coupling, called Förster Resonance Energy Transfer (FRET), allowing for a relaxation time in the sub-ns

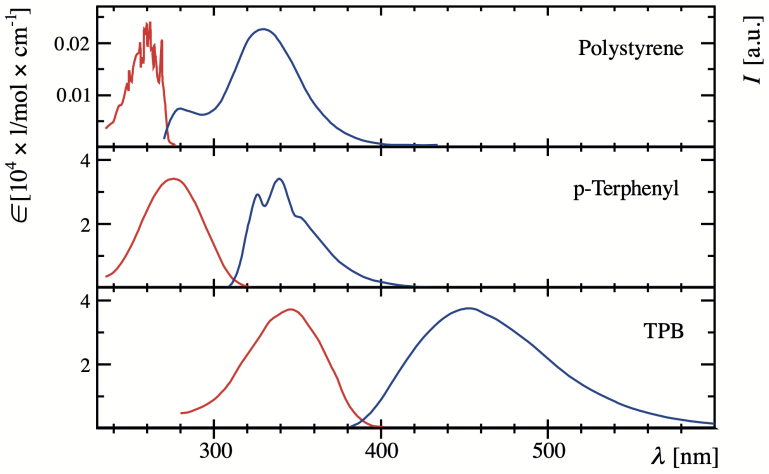

Figure 3.3 – The multi-step scintillating process of the SCSF-78MJ fibre. Absorption is shown in red, while the spectral emission intensity is shown in blue. The data for core material polystyrene (PS), the activator p-Terphenyl (PTP) and the wavelength shifter tetraphenyl-butadiene (TPB) refer to solutions in cyclohexane and are obtained from Ref. [106]. *Picture taken from Ref. [107].*

level. However, the emitted photon is in the UV spectral range, which can only travel a few µm in the plastic. Thus the second scintillator tetraphenyl-butadiene (TPB) is added (0.1% by weight) to act as a wavelength shifter. The UV photons are therefore absorbed and re-emitted in the spectral range. The total scintillator decay time is dominated by the TPB, and amounts to 2.8 ns.

The scintillating fibre has a diameter of 250 µm, including the two claddings. The inner cladding (IC) and outer cladding (OC) are used to increase the trapping efficiency as scintillating light is emitted isotropically inside the fibre. The polymer core has a refractive index of $n_{\mathrm{core}} = 1.59$, while the refractive index of the claddings is decreasing to $n_{\mathrm{IC}} = 1.49$ and $n_{\mathrm{OC}} = 1.42$, respectively. The fibre has a high light yield of 8000 photons per MeV of deposited energy, which corresponds to an average of 300 photons for a minimum ionising particle traversing one such 250µm-thick fibre in the centre. 5.35% of the light is captured by internal reflection in both directions, as shown in Fig. 3.4. Due to the fibres refractive indices, the maximal exit angle of photons in air specified by the manufacturer is 45.7°. This is especially important for the implementation of microlenses described in Chapters 4 and 5. The fibres have an attenuation length of 3 – 3.5 m before irradiation, which reduces to less than 1 m at the worst location after irradiation. Due to the non-homogeneous irradiation profile ($\propto 1/r$) in LHCb, a reduction of the light output at 50 fb^{-1} is expected. For the central modules with the highest radiation exposure, the light loss for photons produced close to the mirror is

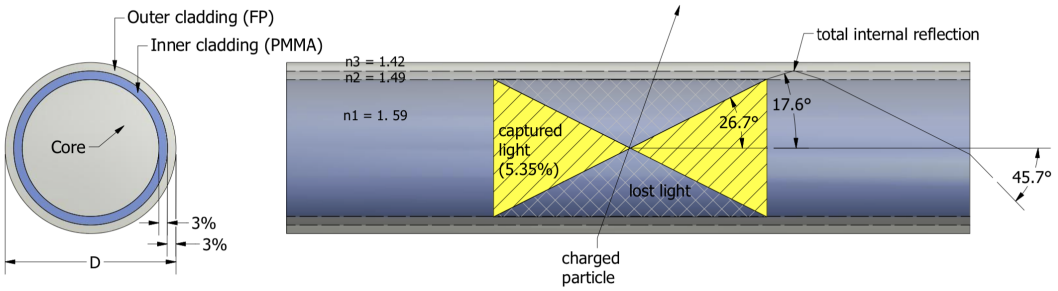

Figure 3.4 – Schematics of the scintillating fibre SCSF-78MJ. Note that the angles 26.7° and 17.6° correspond to the angles at which total internal reflection occurs for the core and first cladding. *Picture taken from Ref. [108].*

expected to reach up to 40%. Finally, the light travels along the fibre with an average speed of 150 mm/ns. This is an important characteristic for timing applications as the travel distance inside the fibre has to be compensated. The measurement of the time resolution of a short fibre mat is described in Sec. 6.1.

3.4 SiPMs

The scintillating light is detected by customised multichannel SiPM arrays produced by Hamamatsu. 4096 arrays of SiPMs are used to equip the full LHCb SciFi Tracker. A SiPM array, shown in Fig. 3.5, consists of 128 channels and covers a total area of 32.540 mm × 1.625 mm. The array is built with two separate silicon dice, each with 64 channels, mounted on a common PCB. The dead area between the dice is 220 µm. Every channel has a width of 230 µm, and is connected via individual bond wires. 104 pixels with a size of 57.5 µm × 62.5 µm and a GFF = 65% form one channel. The pitch between channels amounts to 250 µm. A feature of this detector is the transparent thin metal film implemented as quench resistor, which transmits 80% of the light and thus reduces the dead pixel area. A 105 µm thick transparent epoxy entrance window protects the silicon and the bond wires from environmental and mechanical damage. Deep trenches between pixels decrease the optical crosstalk. The PCB is soldered onto a Kapton flex cable, and is stabilised with a ceramic stiffener. A PT1000 temperature sensor is integrated on the flex PCB, and allows to measure the temperature with an accuracy of ±1°C .

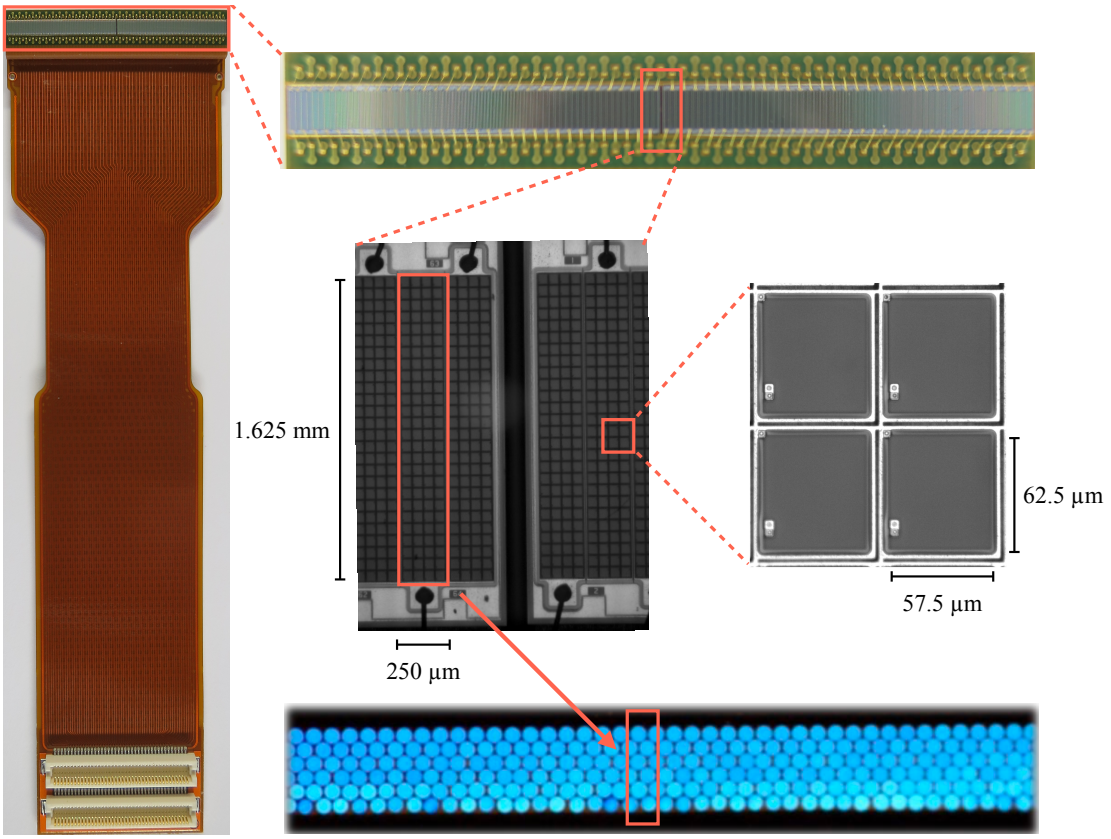

Figure 3.5 – A H2017 SiPM array for the LHCb SciFi Tracker. The two silicon dice are bonded onto a Kapton flex PCB (left). The SiPM consists of 128 channels, with bond wires alternating on each side for signal collection.

The SiPMs have been fully characterised at EPFL and the results are reported in detail in Refs. [85, 97]. The most important features for these photodetectors are listed below:

Low noise: Noise clusters can be produced by correlated noise or random overlap of DCR pulses in the integration window. The noise has to be low to achieve the hit detection efficiency of > 95% for the full SciFi Tracker at the end of lifetime. The correlated noise probability of the H2017 is shown in Fig. 3.6a. At the operational voltage of $\Delta V = 3.5$ V the technology shows a total correlated noise probability of less than 10%, and is independent of the radiation at this level. The DCR is in general strongly affected by irradiation. The SiPMs were thus optimised to provide an acceptable rate of dark counts after irradiation of 4.1×10^{11} 1 MeV $n_{\mathrm{eq}}/\mathrm{cm}^2$ to achieve the required detection efficiency.

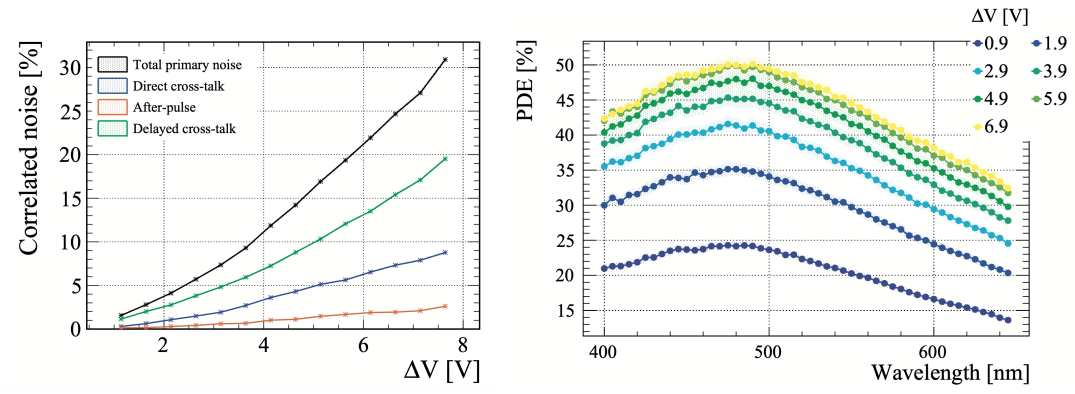

(a) (b)

Figure 3.6 – Correlated noise as a function of ΔV (a) and PDE as function of wavelength (b) for the H2017 detector. *Pictures taken from Ref. [85].*

High PDE: The PDE is the figure of merit for the photodetector. High PDE allows for high signal thresholds without efficiency loss. The pixels of the H2017 were chosen to be big to have the highest possible PDE without compromising the detector in other requirements such as gain, recovery time or DCR. The PDE (shown in Fig. 3.6b) reaches up to 45% at the operating overvoltage $\Delta V = 3.5\,V$.

Short recovery time: The recovery time influences the dead time of the detector, thus τ_{rec} should be as small as possible to ensure small dead time at the full 40 MHz data rate. For a H2017 detector, the average recovery time is 84 ns [85].

3.5 Readout electronics

The data is read out by customised electronics at an event rate of 40 MHz. In the first step, an application-specific integrated circuit (ASIC) called PACIFIC* acquires the signal from the SiPM channels, and processes it using threshold-level discriminators. The amplitude information is used to form clusters.

Clustering algorithm: A typical signal is distributed over several neighbouring SiPM channels. A threshold-based algorithm groups neighbouring channels into clusters to suppress noise. At LHCb SciFi clustering is based on an algorithm with three thresholds (2-bit digitisation). The data is then transmitted from the ASIC to a closely attached Field-Programmable Gate Array

*low-Power Asic for the sCIntillating FIbre traCker (PACIFIC)

(FPGA). The three thresholds are: *seed*, *neighbouring* and *high threshold*. To suppress random noise, a cluster is only formed if:

1. at least one channel exceeds the seed threshold and at least one adjacent channel reaches the neighbouring threshold, or
2. three single channels reach the neighbouring threshold, or
3. a single channel exceeds the high threshold.

The maximum cluster size is limited to four channels. In clusters exceeding four channels, the first four channels are flagged as "large", and the last channels (up to four) are flagged as the end of the large cluster. The decoding then either merges these clusters again as a single large cluster (smaller than eight) or creates two or more clusters with widths up to four channels each. The values for the seed, neighbouring and high thresholds are typically 2.5, 1.5 and 4.5 photoelectrons. These thresholds are the result of an optimisation process taking into account the light yield of the detector, the acceptable noise cluster rate, the required efficiency of the detector and the correlated noise characteristics of the SiPMs in use. Further parameters are the integration and shaping time of the front-end electronics (as e.g. described in Ref. [85]). The parameter set is adjusted during the lifetime of the detector to account for the increase in DCR (ageing). The clustering algorithm is illustrated in Fig. 3.7. The zero-suppression is optimised to reduce the data bandwidth.

The threshold information is digitally encoded and sent to the clusterisation board. This board houses two FPGAs, on which the clusterisation is performed. Only the cluster position, cluster size and cluster quality bit is transmitted to the off-detector processor. The master board collects all data from the clusterisation boards and sends them to the data acquisition (DAQ) system.

The DAQ system (shown in Fig. 3.8) consists of three logical stages: event readout, event building and event filtering. In the event readout, the front-end information of the subdetectors is transmitted to the event building network via optical links. The data is then sent back to the event builder PCs. In the final step, the event selection is performed by the HLT as described in Sec. 1.2.1, and only selected events are stored. [109]

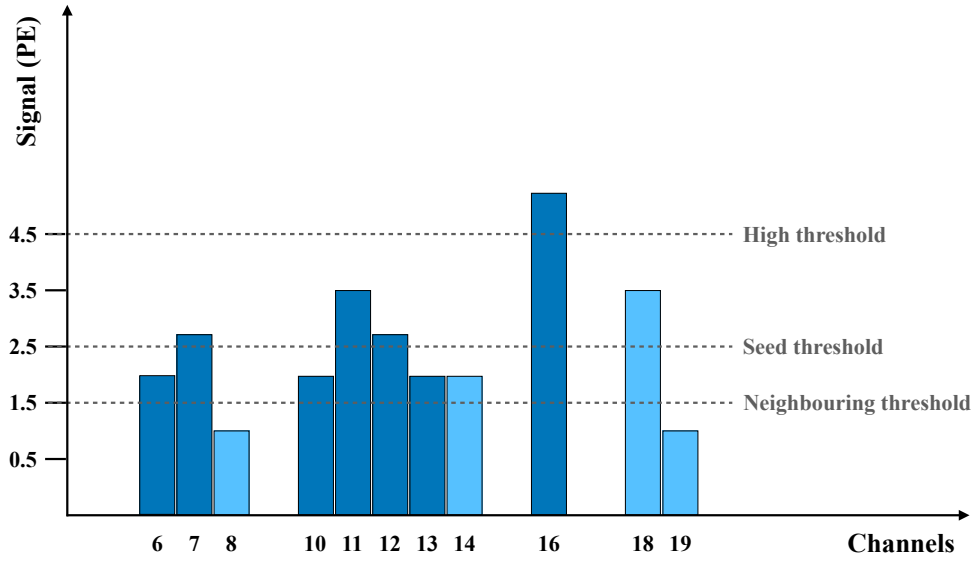

Figure 3.7 – The three threshold-based clustering algorithm of the LHCb SciFi Tracker. Formed clusters are coloured in dark blue. Channel 14 is not included in the cluster as it is not a neighbour to a seed.

3.6 SciFi Tracker modules

For the SciFi Tracker at LHCb, a dedicated development lead to the fibre mat construction process called fibre winding. Single fibres are wound on a wheel with a thread and fixed with glue loaded with TiO_2 to minimise the spread of photons produced by ionisation between fibres. The mats are produced with a customised winding wheel, which defines the pitch between fibre centres of 275 µm. One single mat is 130.80 mm wide, and has a length of 2.424 m and a thickness of 1.35 mm. At one end of the fibre mat a thin mirror is glued to increase the light yield. Each mat surface is covered with a thin Kapton foil for mechanical stabilisation.

Eight fibre mats are grouped together to form a module of a size of 0.53 m × 4.85 m. The mats are carefully aligned and sandwiched between two carbon fibre sheets with a honeycomb structure and a thickness of about 20 mm, leading to a total module thickness of 42 mm. Endplugs are placed at the module end containing a light injection system for SiPM calibration and provide mechanical support and alignment for the SiPMs.

Four SiPM arrays are grouped together according to their thickness and breakdown voltage (variation of less than 0.5 V) to allow for a common bias voltage. The SiPMs are then firmly pressed against the optical interface of the SciFi mat. A thermal isolation box surrounds the photodetectors and ensures gas tightness and the stable operation of the SiPMs at −40 °C .

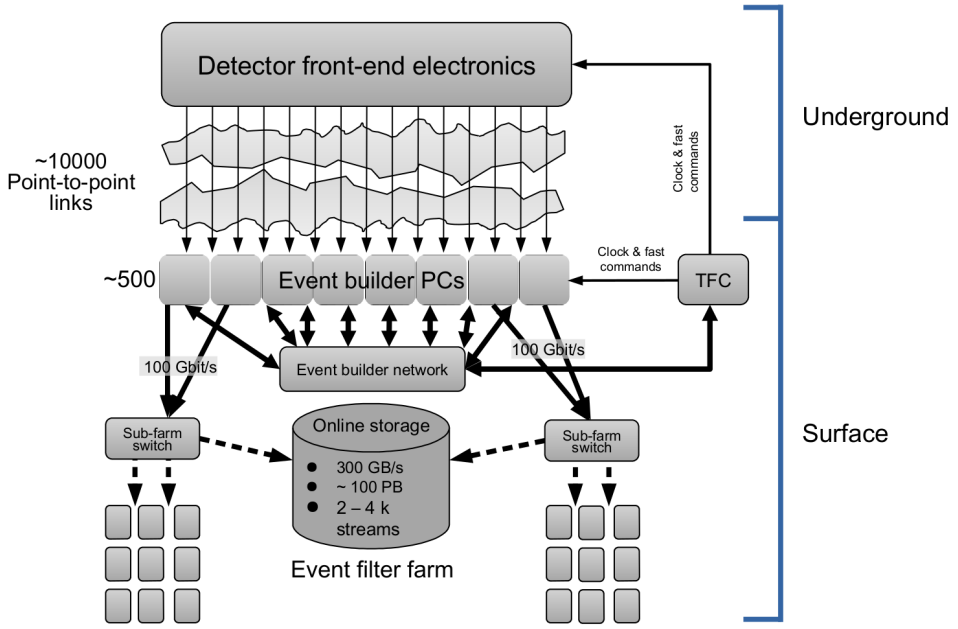

Figure 3.8 – The LHCb data acquisition system for Run 3. Events are built by combining data from all LHCb subdetectors, and are then forwarded to an event filter farm where the event reconstruction is done. Only selected events are stored. The Time and Frequency Control (TFC) ensures that all readout electronics and the event builder network run synchronous to the LHC bunch crossing frequency. *Picture taken from Ref. [109].*

The modules are mounted on C-frames, where one C-frame contains one half of the 0°-layer (x-layer) and one half of a 5°-layer (u- or v-layer). The other matching halves are on a second C-frame, such that two SciFi layers are made of two C-frames. In a C-frame half of a layer is made of five or six modules. Additionally to the SciFi modules, the C-frames contain the services, which include the dry gas, optical readout links, vacuum-insulated cooling pipes, high and low voltage cables, and the front-end electronics boxes. The C-frames are mounted on rails, allowing for the opening and closing of the halves for maintenance and operation. Altogether the tracker consists of twelve such C-frames, forming the twelve layers of the SciFi.

3.7 Radiation damage of the SciFi Tracker

The radiation environment described in Sec. 1.3 will cause significant ageing in the SciFi Tracker. Firstly, the fibre's attenuation length is decreased and will cause a reduction in light yield by up to 40% in the worst central region. Secondly, the DCR of the SiPMs would dramatically increase at standard temperatures. The SiPMs are thus cooled to −40 °C, as the DCR decreases approximately by a factor of two every 10 K. The expected DCR after irradiation of 4.1×10^{11} 1 MeV $n_{\mathrm{eq}}/\mathrm{cm}^2$ (corresponding to 50 fb^{-1}) is therefore limited to 10 MHz per

channel [110]. The combination of the ageing effects of the fibres and the radiation effect of the SiPMs will decrease the average signal per cluster from 20 to 12 PE, with the noise cluster rate reaching up to 2–3 MHz per SiPM array.

Since the start of the new data taking period Run 3 in spring 2022, the SciFi Tracker has been exposed to an estimated radiation of approximately 1.05 fb^{-1}. Figure 3.9 shows the analysis of the average DCR (calculated from the measured current) for a single SiPM channel with respect to the integrated luminosity of the first layer of every SciFi station (T1, T2, T3). The data has been taken at a temperature of 23.5 °C . The DCR increases from 6.6 MHz at 560 pb^{-1} to 10 MHz 1040 pb^{-1} for station T1, from 8.9 MHz to 13.2 MHz for T2, and from 9.3 MHz to 14.3 MHz for station T3, which is the one closest to the calorimeters. Annealing has taken place during beam absence, and can be seen in the decrease of the DCR. The most visible example is at around 790 pb^{-1}, where the DCR decreased approximately 1 MHz for all three stations. Note that the two data points at 780 pb^{-1} and 800 pb^{-1} were taken a few weeks apart.

Scaling the measured DCR to the irradiation level of 50 $fb^{-1}$and to −40 °C, assuming that the DCR is halved every 10 K, the DCR per channel is approximately 8 MHz for T1, 10 MHz for T2 and 11 MHz for T3. This is in very good agreement to the expected DCR of 10 MHz.

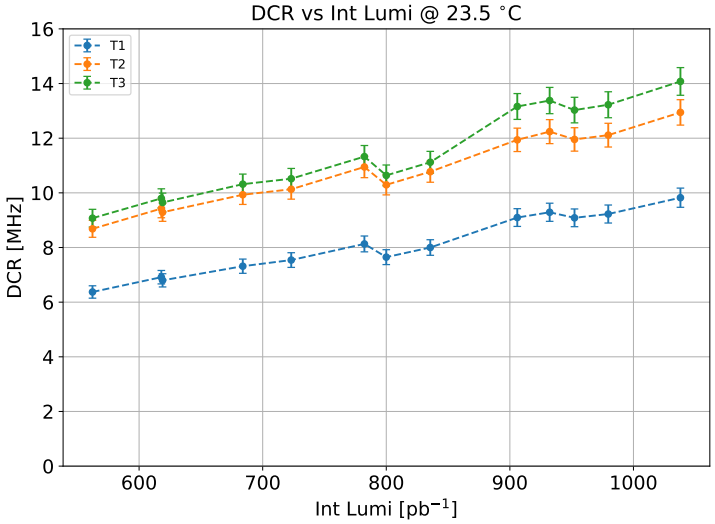

Figure 3.9 – The average DCR of one SiPM channel of the SciFi Tracker as a function of the integrated luminosity cumulated from October to November 2023. The blue line is the DCR for SciFi station T1, the orange for station T2 and the green for station T3. For each station, the SiPMs are selected to be in the centre of the first layer. The detector has been operated at a temperature of approximately 23.5 °C for this measurement. The significant decrease in DCR at around 790 pb^{-1} and 950 pb^{-1} shows that annealing of the SiPMs has taken place in periods of beam absence. *Picture taken from Ref. [111].*

3.8 Other applications

The SciFi technology developed for LHCb is also employed in other applications and experiments, of which a short list is given below. As the requirements are different from those of the LHCb SciFi Tracker, R&D is performed in different areas, for example the implementation of timing information and the extension of the detector response for ion detection in different energy regions. It is important to take these other applications into consideration when it comes to the customisation and optimisation process of detectors (e.g. packaging options).

SND@LHC: The SND@LHC experiment [13] is dedicated to identify and measure the three types of standard-model neutrinos produced in the very forward region of the pp collisions at LHC. The detector has been installed in 2021, and the data–taking started with Run 3. The target region of the detector consists of emulsion walls (alternating tungsten and emulsion films with micrometric spatial resolution) and SciFi planes oriented in x-y direction. The SciFi planes are used to provide the event timestamp, and determine the energy as well as spatial information. The fibre mats are composed of six layers of 250 µm-thick fibres (SCSF-78MJ), and form 40 cm × 40 cm big modules. They are read out by H2017 SiPMs, identical to the ones of the current LHCb SciFi Tracker. Different read-out electronics than in LHCb are used. The SciFi tracker at SND@LHC can achieve a time resolution of 200 ps for one x-y station.

BGV: A Beam-Gas Vertexing (BGV) demonstrator, described in detail in Ref. [85], was built as a non-invasive beam-monitoring device for the LHC in 2015. The installed prototype consists of a gas tank and two SciFi stations for charged particle tracking. Each station is composed of two modules placed above and below the beam pipe, and oriented to obtain x and y information. One module is made of two fibre mats oriented at 0° and 2° for ghost suppression. The mats are made of four or five layers of SCSF-78MJ fibres, and cover an active area per plane of 260 mm × 340 mm. The readout SiPMs are H2014 detectors manufactured by Hamamatsu, a previous prototype version of the H2017.

HERD: The High Energy Cosmic Radiation Detection (HERD) experiment [112] is a future space experiment, with a planned start around 2027, and will measure cosmic rays in unprecedented energy regions. The detector will be equipped with four scintillating fibre walls for tracking, described in Ref. [113]. The fibre mats are made of six layers of scintillating fibres (type SCSF-78MJ) oriented in x and y direction. The width of a mat is 97.8 mm. The used SiPM S13552-10 by Hamamatsu is a variant of the H2017, but with 10 µm square pixels, which extends the linearity range needed for particle identification of ions.

Mu3e: The Mu3e experiment [114] , which is currently under construction at the Paul Scherrer Institut (PSI), uses a SciFi detector in combination with a scintillating bars tracker to provide very precise timing information for the search of the lepton flavour violating decay $\mu^+ \rightarrow e^+e^+e^-$. The fibre mats are made of three layers of staggered 250 µm thick scintillating fibres (SCSF-78MJ). H2017 photodetectors are used for the fibre read-out. The SciFi detector provides a time resolution of 250 ps when read out with the dedicated MuTRiG ASIC [115].

4 Simulation study of microlens-enhanced SiPMs

The radiation environment in Run 3 and 4 will cause significant ageing effects in the SciFi Tracker. The light yield of a minimum ionising particle traversing the fibre mat will decrease from approximately 20 to 12 photoelectrons [28]. Additionally, the DCR of the photodetectors will dramatically increase making tighter noise cuts necessary to comply with an acceptable noise cluster rate.

An efficient way to mitigate these radiation-induced ageing effects is to increase the PDE of the photodetectors. The central point of this thesis is to study the feasibility of implementing an optical focusing system consisting of microlenses on the pixelised SiPM surface. The focusing is used to avoid dead and inefficient pixel regions, increasing the effective ratio of the active-to-total area. A dedicated simulation study using the ROOT framework was performed to evaluate the feasibility of such a system for the LHCb SciFi Tracker. Its results are described in this chapter.

4.1 Light propagation through the optical interface

The light propagation from the fibre to the SiPMs involves several media with different refractive indices. A light ray exiting the fibre core will pass through air and a polymer, i.e. flat coated layer or implemented microlenses, before reaching the silicon, as shown in Fig. 4.1.

The light propagation is described by the Fresnel equations for transmission and reflection of a plane wave. The angle of reflection is equal to the incident angle θ_i, whereas the angle of transmission θ_t can be determined with Snell's law between two media:

$$n_i \sin(\theta_i) = n_t \sin(\theta_t)\,, \tag{4.1}$$

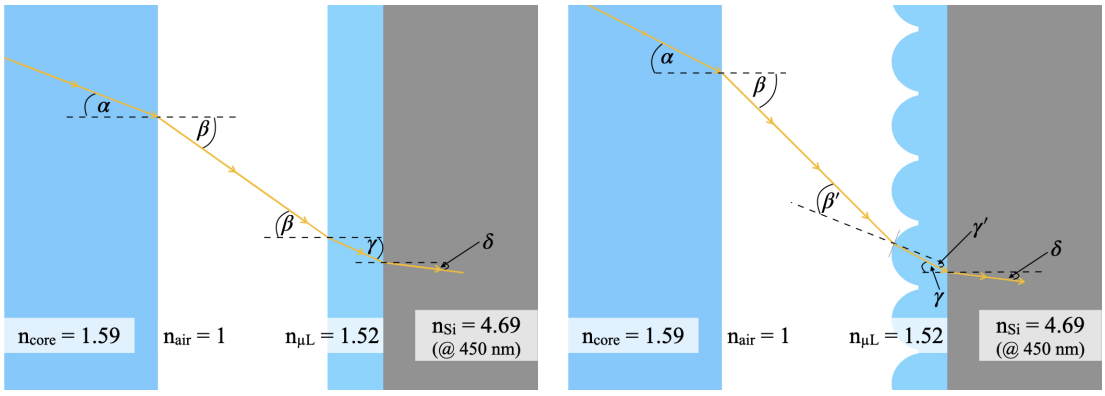

(a) flat coated layer (b) microlenses

Figure 4.1 – Schematics (not to scale) of the path of the light propagating from the fibre core to the silicon without and with the addition of microlenses, indicating the refractive indices and the angles between the different media: fibre core, air, microlens material (μL) and silicon (Si). An anti-reflective coating may be present on top of the silicon.

where n_i is the refractive index of the medium of the incident angle and n_t of the transmitted one. The effective reflectivity of unpolarised light, like the light from the fibre, is given by [116]:

$$R_\mathrm{eff} = \frac{1}{2}\left(\left|\frac{n_\mathrm{i}\cos(\theta_\mathrm{i}) - n_\mathrm{t}\cos(\theta_\mathrm{t})}{n_\mathrm{i}\cos(\theta_\mathrm{i}) + n_\mathrm{t}\cos(\theta_\mathrm{t})}\right|^2 + \left|\frac{n_\mathrm{i}\cos(\theta_\mathrm{t}) - n_\mathrm{t}\cos(\theta_\mathrm{i})}{n_\mathrm{i}\cos(\theta_\mathrm{t}) + n_\mathrm{t}\cos(\theta_\mathrm{i})}\right|^2\right). \tag{4.2}$$

The reflection probabilities of a light ray between the different media were calculated according to Eqs. 4.1 and 4.2 for a flat coated layer, and are listed in Table 4.1. From these formulas, the largest possible value of the exit angle in air is 89.57°. In the case where microlenses are implemented on the silicon surface, the calculation has to be performed using the vector of the incoming photon and the normal of the lens. This has been done in the simulation study, described in Sec. 4.5.

However, the double-cladded fibre used in the LHCb SciFi Tracker (see Sec. 3.3) is designed to maximise the light trapping efficiency with a numerical aperture of 0.71. The numerical aperture corresponds to the sine of the maximum angle for which total internal reflection occurs between the core and the fibre cladding. Therefore, the maximum angle inside the fibre core is limited to $\alpha = 26.75\,^\circ$ to provide total internal reflection between core material and the second cladding, capturing a minimum of 5.35 % of the produced light in each direction (see Fig. 3.4). This corresponds to a maximum exit angle in air to $\beta = 45.7°$. In contrast to these fibre propagation properties, exit angles up to 55° have been observed. They can be explained by helicoidal modes, where light rays propagate without crossing the fibre axis, i.e. spiralling along the fibre as described for example in Ref. [117].

4.2 Scintillating fibre exit angle distribution

With a spherical lens, a parallel incident (perfectly collimated) light beam can be focused into one point. This principle has been prototyped on small surface SPADs to increase the GFF and consequently the PDE for low-light imaging applications [118].

For the LHCb SciFi Tracker, however, the light exiting the scintillating fibre has an angular distribution determined by the numerical aperture, resulting in partially collimated light. This exit angle distribution is crucial to evaluate the efficiency of a focusing system made of microlenses. Therefore a simulation study and a measurement have been performed to determine this distribution.

4.2.1 Simulation of the fibre exit angle distribution

The light propagation in the fibre and the exit angle in air have been simulated [119] using the GEANT4 framework [120, 121]. GEANT4 is the standard simulation package used in high-energy physics for detector simulation. It provides the implementation of the scintillator and directly includes the light propagation in solids. The simulation is based on the single fibre simulation for the LHCb SciFi Tracker described in Ref. [107].

In the LHCb tracking detector, the majority of particles are expected to act like minimum ionising particles (MIP-like), and the particles detected in the SciFi Tracker are indeed MIP-like. Therefore, in this simulation, a double-cladded 2.4 m long fibre is excited by 2 GeV muons to mimic MIP-like particles passing the detector at a distance of 1.8 m from a detector placed at the fibre end. The number of photons and the angular distribution is measured. The refractive indices correspond to the ones specified by the manufacturer in Sec. 3.3 and the scintillation yield is set to 8000 photons/MeV according to manufacturing specifications for the SCSF-78MJ

Table 4.1 – Reflection probabilities for the transitions between the different media for the case of a flat coated layer. The maximum angle (also known as critical angle) for which light can exit the fibre core material is $\alpha = 38.97°$.

α (°)	β (°)	$R_{eff,air}$ (%)	γ (°)	$R_{eff,\mu L}$ (%)	δ (°)	$R_{eff,Si}$ (%)
5.00	7.97	5.19	5.34	3.87	1.69	26.72
10.00	16.03	5.20	10.68	3.88	3.38	26.72
15.00	24.30	5.26	16.03	3.93	5.05	26.72
20.00	32.94	5.44	21.41	4.10	6.68	26.73
25.00	42.22	6.00	26.81	4.61	8.26	26.76
30.00	52.66	7.69	32.25	6.18	9.78	26.80
35.00	65.78	14.21	37.74	12.51	11.24	26.89
38.97	89.57	95.86	42.15	95.77	12.34	27.00

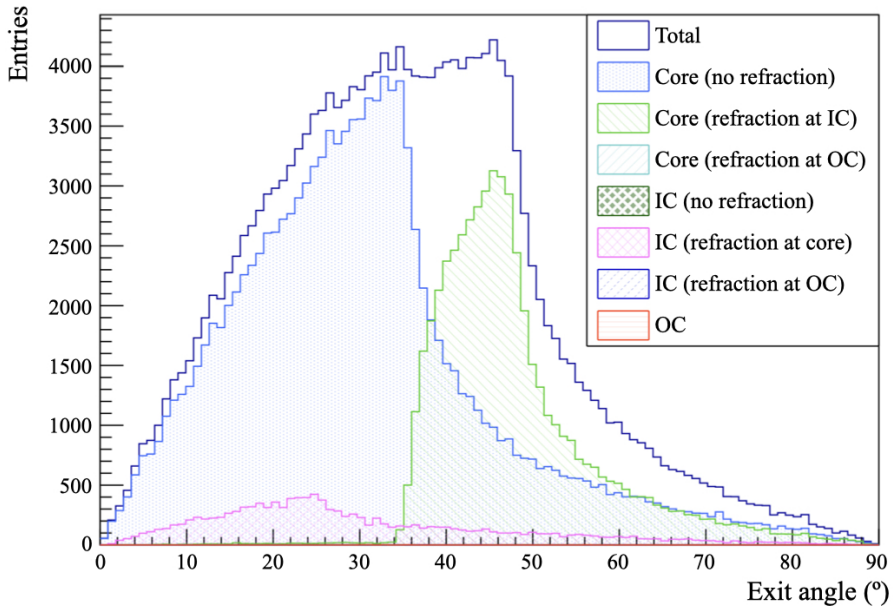

Figure 4.2 – Simulated fibre exit angle distribution in air, with a mean value of 35.6°. The contributions of photons exiting the fibre from the core, IC and OC (taking into account refraction possibilities at the different interfaces) are shown. The total distribution is made up of photons exiting the fibre from the core without refraction (bright blue), from the core with refraction at the inner cladding (green), or from the inner cladding with refraction at the core (pink).

fibre used in the LHCb SciFi Tracker. The components are divided into photons exiting the fibre from the core, from the inner cladding (IC) or from the outer cladding (OC).

The simulated distribution in Fig. 4.2 shows that the majority of detected photons exits the fibre from the core, either without refraction (Fig. 4.3a) or with refraction at the IC (Fig. 4.3b). A small contribution is given by photons exiting the fibre from the IC with refraction at the core (Fig. 4.3c). In this case the photons propagate to the fibre end in the same way as in Fig. 4.3b, but the refractive indices are different at the fibre interface to air. Photons that refract or exit the fibre via the OC have no contribution to the total distribution as they are heavily suppressed due to the large number of interface transmissions necessary for propagation. In Fig. 4.2 these components are zero.

(a) Core (no refraction) (b) Core (refraction at IC) (c) IC (refraction at core)

Figure 4.3 – The three modes of photons exiting the scintillating fibre that make up the vast majority of the simulated exit angle distribution of the single fibre in air.

4.2.2 Measurement of the exit angle distribution

The exit angle distribution was measured for the very first evaluation of microlens-enhanced SiPMs for the SciFi Tracker in 2019 [122](see Appendix A). For this microlens simulation study it has been remeasured with increased accuracy.

A single SCSF-78MJ scintillating fibre with a diameter of 250µm is excited with a UV-LED at a distance of 2.4m from the fibre end, and the light is detected with the camera *Astrolumina QHY5L-II* (CMOS technology) [123]. This camera was chosen as it has a monochrome high quantum efficiency, low noise and a high dynamic range, which is needed for light detection at 0° and 90°. The camera was mounted $d = 140$mm from the fibre end on a rotatable stage providing a coverage from $\beta = 0°$ to $\beta = 90°$. A schematic picture of the setup can be seen in Fig. 4.4.

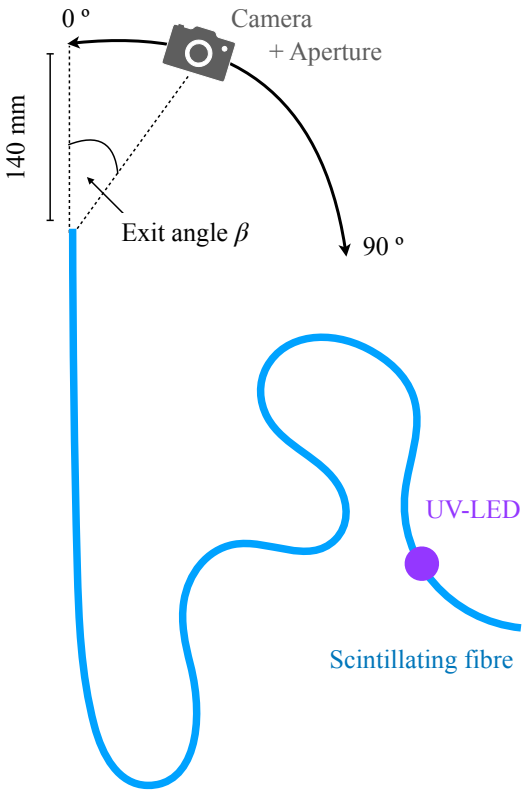

Figure 4.4 – Schematic setup (not to scale) of the exit angle measurement of a scintillating fibre in air.

The setup was placed in a light-shielded box and the UV-LED was operated in a continuous mode. The camera's focus on the optical surface of the fibre end is crucial for the measurement of the intensity with this camera, as

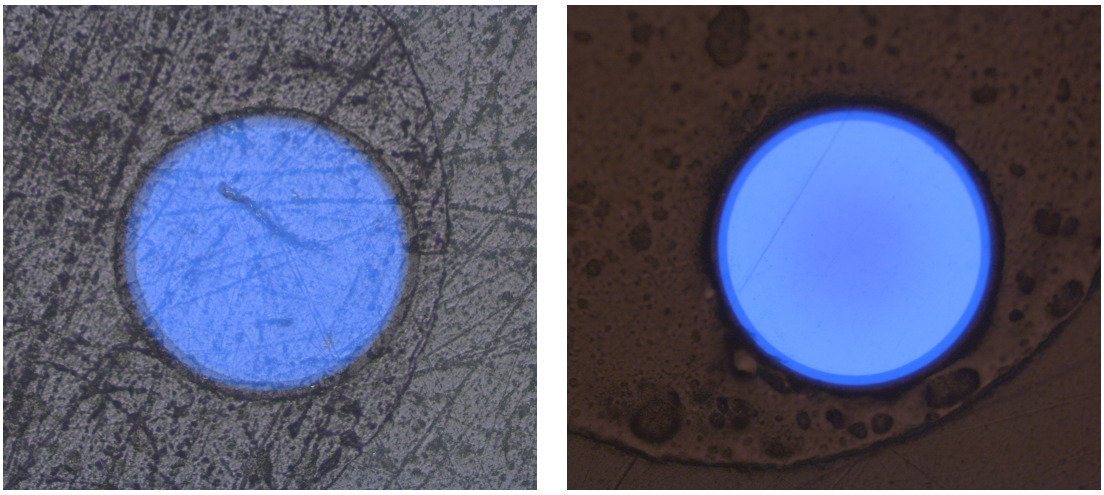

(a) (b)

Figure 4.5 – Picture of the fibre end of a (a) cut and (b) cut, polished and cleaned fibre. The surface quality of the fibre greatly influences the exit angle distribution.

it could otherwise lead to systematic errors. Additionally the exposure time is carefully tuned to 164 ms to avoid saturation at low angles but still detect enough light at angles larger than 50°C. The light output was scanned in angular steps over 5°.

As described in Ref. [124], the measured intensity has to be scaled by a factor g, taking into account the camera's aperture ζ and the angle β:

$$g = \frac{1-\cos(\zeta)}{\cos(\beta-\zeta)-\cos(\beta+\zeta)}\,. \tag{4.3}$$

The angular acceptance ζ is limited by an aperture placed in front of the camera with a radius of 2 mm. The angular acceptance was therefore determined to be $\zeta = \arctan(2\,\text{mm}/d) = 1.6°$.

The exit angle distribution heavily depends on the quality of the fibre end, which must be very well polished and cleaned to achieve a reproducible result. The difference between a cut fibre and a cut, polished and clean fibre is shown in Fig. 4.5.

The fibre's light output was measured by capturing a picture at each angle, and by summing over all pixels in a region of interest, which was necessary as the fibre cross-section is very small compared to the camera's surface, and therefore noisy pixels would influence the result. The fibre was rotated in steps of 90° around its cylindrical axis to ensure it was glued straight into its holder. After a full 360° rotation, the measurement was repeated to reduce systematics and verify that the fibre has not been damaged by the UV-LED. A dark frame was also captured before each fibre rotation and subtracted from the light frame at each angle. The evaluated

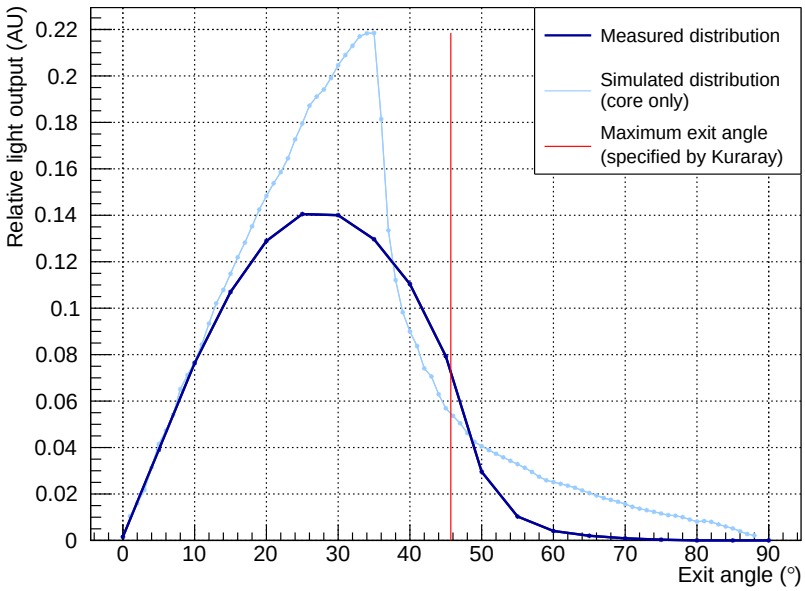

Figure 4.6 – Measured exit angle distribution of a 250 m long scintillating fibre (SCSF-78MJ) in air (dark blue). The fibre was excited with a UV-LED at a 240 cm distance from the fibre end. For comparison, the simulated angular distribution of photons propagating inside the core, which is the dominating mode over large distances in the fibre, is plotted in light blue. The measured distribution corresponds the specified maximum exit angle of 45.7°, with larger angles coming from helicoidal modes.

uncertainties on the measurement are dominated by the preparation of the fibre sample. The exit angle distribution in air averaged over all measurements (two times four fibre rotations) is shown in Fig. 4.6. The statistical error on the averaged values is below 1%.

The exit angle distributions for a fibre excited at 240 cm and 14 cm have been compared, only changing the position of the UV-LED. As can be seen in Fig. 4.7, a clear distinction between the two distributions is observed, corresponding to a shift in the mean value from 27.9° to 34.0°. This confirms that for short travel distances modes with higher angles can still exit the fiber and are not attenuated.

4.2.3 Comparison of simulation and measurement

The result of the exit angle measurement is crucial for the microlens implementation and the optimisation of the microlens parameters. A large discrepancy between the simulated and the two measured exit angle distributions is observed. Modes where the cladding is traversed are subject to strong attenuation. The simulation poorly implements the loss at the interfaces between the core and the claddings as photons travelling in the claddings should be highly suppressed due to the higher attenuation coefficient, and the higher number

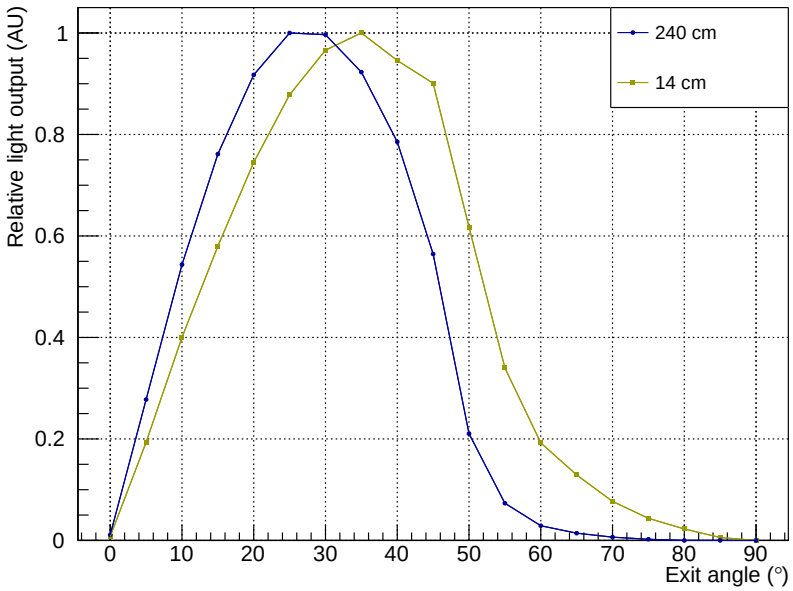

Figure 4.7 – Measured exit angle distribution of a scintillating fibre (SCSF-78MJ) in air. The fibre was excited with a UV-LED at a distance of 240 cm or 14 cm from the fibre end.

of reflections/refractions due to the longer path. This therefore leads to a distribution that overestimates larger angles. These modes can only exit the fibre as helicoidal modes, which seem to be overestimated as well.

Comparing the measured distribution (excitation at 240 cm) with the simulated core distribution, shown in Fig. 4.6, a difference in shape can be seen. However, the observed mean value of the measured distribution follows in good approximation the simulated core light propagation, i.e. 27.9° and 30.8°, respectively, suggesting that the measured light distribution only comes from photons exiting the fibre core. The tail of the simulated distribution is due to larger angles leading to a larger number of internal reflections.

4.3 Microlens arrangement

The goal of implementing microlenses on the SiPM surface is to deviate and to concentrate the light onto the active area. In this section several possible arrangements of the focussing system and their respective advantages and disadvantages are discussed. With the large exit angle distribution of the SciFi Tracker, the primary goal is to focus the light into the active pixel area. Even though a reduction of the sensitive SiPM area would reduce the DCR, it is not a viable option as reducing the sensitive area of a pixel or channel by design will always lead to a loss of detected photons.

One possibility is to place cylindrical lenses across the full SiPM channels to deviate the light from the dead regions along the channel edge, which was considered for the H2017 detector as it has a 10% gap between channels. This implementation, however, will not collect light from all the dead areas surrounding the pixels, and will focus part of the collected light on regions in the middle of the channel including dead and inefficient areas. The improvement in PDE is expected to be small compared to a system where all dead regions are recovered.

Another possibility is to place hexagonal lenses on every pixel of hexagonal shape. The change from square to hexagonal pixels would be necessary as otherwise the full lens coverage of the surface is very inefficient. As hexagonal pixels are a non-standard shape in industry, the optimisation procedure is less advanced optimisation procedure. Additionally, dead regions at the edges of the sensor would be introduced if they are used in the SciFi Tracker. Therefore, this option is also not pursued.

Another possible implementation that has been considered are microlenses aligned with each 250µm-thick fibre of the fibre mat. However, this was deemed unfeasible due to manufacturing tolerances and the fact that dead pixel areas would still be present.

The most promising option is to place microlenses on every other pixel in a checkerboard structure as shown in Fig. 4.8. Light arriving towards dead and inefficient pixel regions is deviated and focused onto the active area with the help of microlenses. The regions that are left uncovered are efficient and do not require any focussing.

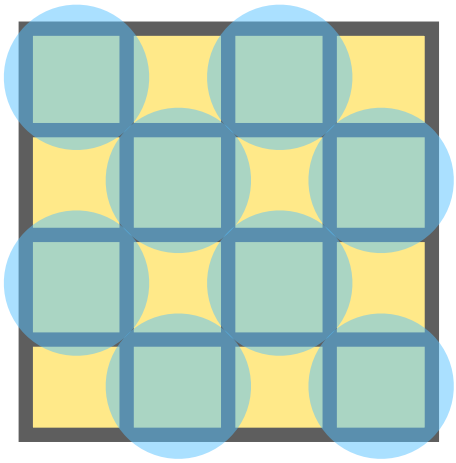

Figure 4.8 – Sketch of the checkerboard implementation of microlenses (in blue) on a SiPM array. The dead regions between the square pixels are indicated as dark bands and the active pixel areas are shown in yellow.

4.4 Microlens simulation

A ray-tracing algorithm has been developed to optimise the parameters of microlenses placed on a pixelised SiPM surface using the ROOTS framework (C++), and is available in an open git repository [125]. This simulation study is an improved version of the one described in detail in Ref. [97]. Results considering a detector with and without microlenses are compared. The improvement obtained due to the microlenses is measured as an increase of the effective geometrical fill factor (EGFF), which is defined as the ratio between the number of photons arriving in an active region of the SiPM surface and the total number of photons arriving at the SiPM surface.

The microlens simulation study uses both, the simulation and measured angular distributions for a long fibre described in Sec. 4.2 to examine the impact of different fibre exit angle distributions. The measured exit angle distribution of a short fibre is well within the range of the simulated and measured distribution for a long fibre module, and has not been available before this simulation study. The microlens prototyping described in Chapter 5, however, is based on the earlier version of the measurement of a long fibre (Fig. A.1), which has an angular distribution with a mean value of 34.8°, which is situated between the two distributions examined in this study.

The photodetector is modelled by a 3×3 pixel grid with the pixel geometry shown in Fig. 4.9. The dead area is implemented as an inactive band surrounding the active area, and is calculated from the geometrical fill factor (GFF):

$$x_{\text{dead}} = x_{\text{pixel}} \cdot \left(\frac{1 - \sqrt{\text{GFF}}}{2} \right), \tag{4.4}$$

$$y_{\text{dead}} = y_{\text{pixel}} \cdot \left(\frac{1 - \sqrt{\text{GFF}}}{2} \right), \tag{4.5}$$

where x_{pixel} is the pixel width and x_{dead} is the width of the dead area in the x direction. The same is applicable to y_{pixel} and y_{dead} in the y direction. To take the edge effects of the electric field into account, an additional part at the border of the active area is implemented with a width of 2 µm and reduced efficiency.

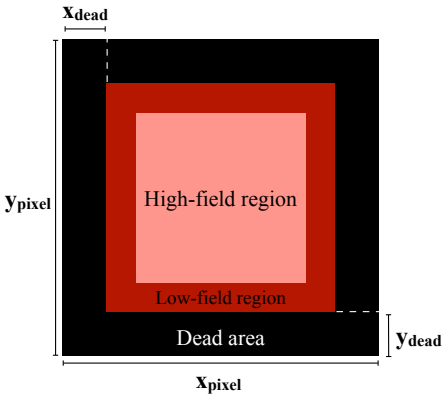

Figure 4.9 – The geometrical fill factor of one pixel is determined by the total active area (high-field plus low-field region) and the dead area.

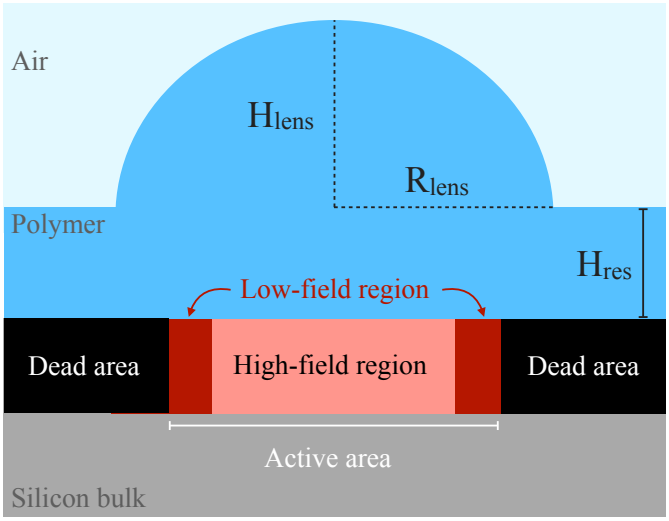

Figure 4.10 – The pixel layout implemented in the simulation. A pixel is made up of the active area, which includes a low-field region with adjustable efficiency, and the surrounding dead area.

One microlens is placed over the central pixel. The spherical lens is characterised by its height H_{lens}, its radius R_{lens} and its residual height H_{res}, which is the thickness of its substrate layer. Varying the residual height influences the region where the photons arrive on the silicon. A schematic picture of a spherical microlens implemented on a pixel is shown in Fig. 4.10. The microlens manufacturing process imposes some restrictions on the parametrisation, which are discussed in Sec. 4.5.

The microlens is simulated as a spherical cap of height:

$$H_{\text{lens}} = R_{\text{lens}} - \sqrt{R_{\text{sphere}}^2 - R_{\text{lens}}^2}, \tag{4.6}$$

where R_{sphere} is the radius of the underlying sphere. The photons are generated randomly at a position x and y, a polar angle θ in the x-y plane with a $0° - 360°$ coverage, and an azimuthal angle ϕ, which was implemented for both exit angle distributions described in Sec. 4.2. The photons are produced in an area exceeding that of the pixel grid, such that a homogeneous distribution across the pixel grid is achieved. The generated photon distribution is shown in Fig. 4.11. The photons travel through air until reaching either the microlens or the substrate layer H_{res}.

The Fresnel reflection of the photon crossing from air to polymer is calculated with Schlick's law, as it allows for a faster calculation of the reflection probability in three dimensions [126]. The photon is either transmitted or reflected, depending on the incident angle ξ between the unit vector $\vec{v}_{\text{i}}$ in the direction of the photon momentum and the unit vector $\vec{n}$ normal to the

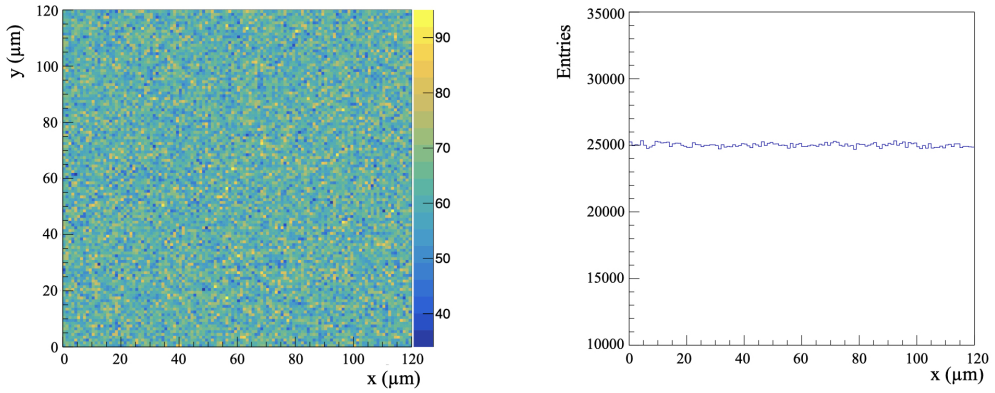

(a) (b)

Figure 4.11 – (a) Distribution of the generated photons over a 3 × 3 pixel grid with a pixel size of 40 µm × 40 µm. The photons are generated at a z-position of $H_{\text{lens}} + 0.01\,\mu\text{m}$. (b) The y-projection of the generation shows the uniformity of the distribution.

lens surface at the point where the photon arrives on the lens. ξ is then computed with:

$$\xi = \cos^{-1}\left(\frac{\vec{n}\cdot\vec{v}_{\text{i}}}{||\vec{n}||\cdot||\vec{v}_{\text{i}}||}\right). \tag{4.7}$$

Once ξ is determined, the reflection probability can be calculated using Schlick's approximation [126]:

$$R(\xi) = \left(\frac{n_{\text{air}} - n_{\text{polymer}}}{n_{\text{air}} + n_{\text{polymer}}}\right)^2 + \left(1 - \left(\frac{n_{\text{air}} - n_{\text{polymer}}}{n_{\text{air}} + n_{\text{polymer}}}\right)^2\right) \times (1 - \cos(\xi))^5, \tag{4.8}$$

with $n_{\text{air}} = 1$ and $n_{\text{polymer}} = 1.5$. If the photon is transmitted, the photon vector after refraction $\vec{v}_{\text{t}}$ is calculated using Snell's law:

$$\vec{v}_{\text{r}} = \frac{n_{\text{air}}}{n_{\text{polymer}}}[\vec{n}\times(-\vec{n}\times\vec{v}_{\text{i}})] - \vec{n}\sqrt{1 - \left(\frac{n_{\text{air}}}{n_{\text{polymer}}}\right)^2 (\vec{n}\times\vec{v}_{\text{i}})\cdot(\vec{n}\times\vec{v}_{\text{i}})}. \tag{4.9}$$

In the region where only the residual layer is present, $\vec{n}$ can be replaced by $\vec{n}_{\text{plane}} = \{0,0,1\}$.

The number of photons arriving in the active and dead areas are counted, and the EGFF can be calculated by the fraction of photons arriving in the active area over the total number of arriving photons. If the photon arrives in the low-field region, it is randomly attributed to photons arriving either at the active or at the dead area, depending on the set efficiency. This is done for the case when no microlens is implemented, returning EGFF_0, and when one microlens is implemented on the central pixel, EGFF_1. The result of EGFF_1 is then scaled

to 4.5 microlenses, which is the average number of lenses that can be implemented on a 3×3 pixel grid:

$$\mathrm{EGFF}_{4.5} = \mathrm{EGFF}_0 + 4.5 \times (\mathrm{EGFF}_1 - \mathrm{EGFF}_0)\,. \tag{4.10}$$

Finally, the improvement in light yield (LY) is calculated as:

$$\mathrm{G}_{\mathrm{LY}} = \frac{\mathrm{EGFF}_{4.5}}{\mathrm{EGFF}_0} - 1\,. \tag{4.11}$$

4.5 Simulation results

The SiPMs for the first implementation, were already available and provided by FBK. These samples were designed for microlens implementation. They have an active die surface of 3.2 mm × 3.12 mm, divided into ten channels with a pixel size of 40 µm × 40 µm, and a fill factor of GFF = 82.4%. R_{lens}, H_{lens} and H_{res} were varied to deduce the optimal lens parameters for such an implementation, based on a previous measurement of the fibre exit angle distribution shown in Fig. A.1. After the first microlens implementation (see Sec. 5.5), the microlens mould design was fixed and fabricated with a designed lens radius of $R_{\mathrm{lens}}/R_{\mathrm{lens,max}} = 95\%$. The lens height H_{lens} was also fixed to $H_{\mathrm{lens}} = 75\%\ R_{\mathrm{lens}}$, based on studies of the variation of H_{lens} which proved that a value below 75% of R_{lens} is not feasible. This value complies with the manufacturing constraints, as the demoulding procedure is impossible for a larger angle between lens and residual height.

In this simulation study, different parameter options are evaluated based on the findings of the first implementation. In addition to a SiPM with GFF = 82.4%, a smaller fill factor of GFF = 50% has been studied. Two different exit angle distributions, namely the simulated (Sec. 4.2.1) and the measured for a long fibre (Sec. 4.2.2), are evaluated to understand the effect on the expected improvement of the gain in light yield for both fill factors. From the first implementation, it has also been clear that the residual height is the most difficult parameter to achieve, and therefore a dedicated study to evaluate the required residual height has been performed. For all studies, the low-field region (LFR) is set to an efficiency of $\varepsilon_{\mathrm{LFR}} = 100\%$ when modelling the array at a high ΔV or to $\varepsilon_{\mathrm{LFR}} = 60\%$ at a low ΔV.

The effect of a paraboloid lens shape was also briefly evaluated. However, the results showed less improvement than possible for a spherical lens and this implementation was thus not pursued.

4.5.1 Impact of the lens radius

R_{lens} is varied to evaluate the optimal relation between the lens radius and the pixel size to deviate the highest amount of light towards the active region. The maximal lens radius in the simulation $R_{\text{lens,max}}$ is equal to the half-diagonal of the pixel $L_{\text{pix}}/\sqrt{2}$. The study was performed for the three values $R_{\text{lens}}/R_{\text{lens,max}} = \{100\%, 95\%, 90\%\}$, to understand how heavily the light yield is influenced by each parameter. The radius of $R_{\text{lens}}/R_{\text{lens,max}} = 95\%$ is in accordance with the specified minimal distance between lenses for the production ($2-4\,\mu$m). The residual height was fixed to $H_{\text{res}} = 10\,\mu$m. The obtained results are listed in Tables 4.2 and 4.3 for GFF = 50.0% and GFF = 82.4%, respectively. The photon distribution of a microlens with $R_{\text{lens}}/R_{\text{lens,max}} = 95\%$ implemented on pixels with a GFF = 50.0% is shown in Fig. 4.12.

The maximum lens radius shows the least improvement for all combinations. For the pixel with GFF = 50.0%, the smallest lens radius $R_{\text{lens}}/R_{\text{lens,max}} = 90\%$ results in the highest gain for both angular distributions. For a partially efficient low-field region, this gain is only minimal, whereas for the fully efficient pixel the gain becomes more significant.

For the larger fill factor with $\varepsilon = 60\%$, no significant difference between a lens with radius $R_{\text{lens}}/R_{\text{lens,max}} = 95\%$ or $R_{\text{lens}}/R_{\text{lens,max}} = 90\%$ is observed for both angular distribution. For the fully efficient pixel, the lens with radius of 95% $R_{\text{lens,max}}$ yields the better result.

At the time this simulation study has been performed, the microlens mould has already been fabricated with a designed lens radius of $R_{\text{lens}}/R_{\text{lens,max}} = 95\%$. The following study on the residual height described below is therefore performed with the radius fixed to this value.

Table 4.2 – Simulation results for different microlens radii R_{lens} for a 40µm × 40µm pixel with GFF = 50.0%. The residual height is set to $H_{\text{res}} = 10\,\mu\text{m}$. The statistical uncertainty of the obtained $\text{EGFF}_{4.5}$ and G_{LY} values is 0.30% and 0.31%, respectively.

ε_{LFR} (%)	Angular distribution	$R_{\text{lens}}/R_{\text{lens, max}}$ (%)	R_{lens} (µm)	EGFF_0 (%)	$\text{EGFF}_{4.5}$ (%)	G_{LY} (%)
60	measurement	100	28.28	44.8	65.7	46.7
		95	26.87	44.7	68.2	52.5
		90	25.46	44.7	69.5	55.5
	simulation	100	28.28	44.7	62.7	40.4
		95	26.87	44.7	65.0	45.6
		90	25.46	44.7	65.2	45.9
100	measurement	100	28.28	50.0	72.9	45.9
		95	26.87	50.0	75.2	50.6
		90	25.46	50.0	75.9	51.9
	simulation	100	28.28	50.0	68.6	37.2
		95	26.87	50.0	70.5	40.9
		90	25.46	50.0	71.5	42.9

Table 4.3 – Simulation results for different microlens radii R_{lens} for a 40µm × 40µm pixel with GFF = 82.4%. The residual hight was set to $H_{\text{res}} = 10\,\mu\text{m}$. The statistical uncertainty of the obtained $\text{EGFF}_{4.5}$ and G_{LY} values is 0.25% and 0.26%, respectively.

ε_{LFR} (%)	Angular distribution	$R_{\text{lens}}/R_{\text{lens, max}}$ (%)	R_{lens} (µm)	EGFF_0 (%)	$\text{EGFF}_{4.5}$ (%)	G_{LY} (%)
60	measurement	100	28.28	75.5	91.6	21.3
		95	26.87	75.5	93.2	23.5
		90	25.46	75.5	92.8	23.0
	simulation	100	28.28	75.5	89.0	17.9
		95	26.87	75.5	90.6	19.9
		90	25.46	75.5	90.4	19.7
100	measurement	100	28.28	82.4	95.3	15.7
		95	26.87	82.4	96.9	17.6
		90	25.46	82.4	96.0	16.6
	simulation	100	28.28	82.4	93.7	13.8
		95	26.87	82.4	95.1	15.5
		90	25.46	82.4	93.9	14.1

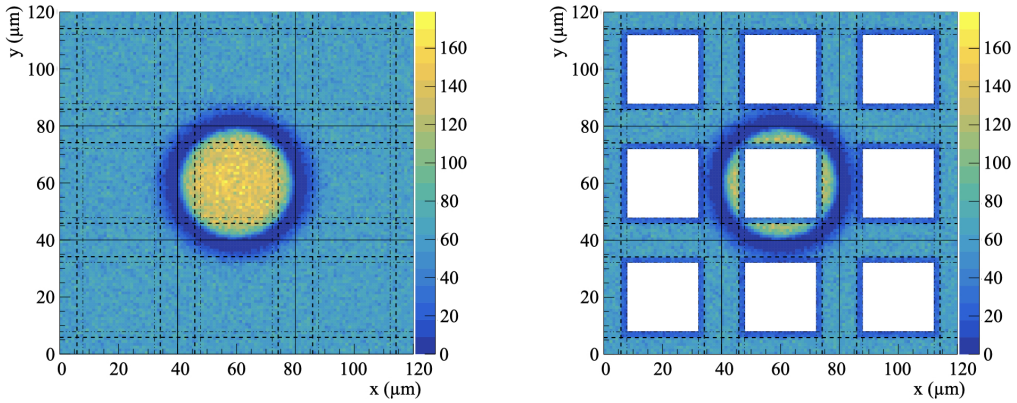

(a) (b)

Figure 4.12 – Simulation result of the photon distribution after propagation to the (a) total pixel area and (b) dead pixel area. The lens is implemented with a radius $R_{\text{lens}}/R_{\text{lens,max}} = 95\%$ and $H_{\text{res}} = 10\,\mu\text{m}$ on pixels $40\,\mu\text{m} \times 40\,\mu\text{m}$ and GFF = 50.0%. The thick dashed lines show the dead area, whereas the thin dashed lines highlight the implemented low-field region, where the efficiency is set to 60%. The results were obtained with the measured (narrow) exit angle distribution.

4.5.2 Impact of the residual height

The variation of the residual height was studied for both fill factors, GFF = 50.0% and GFF = 82.4%, and the results are listed respectively in Tables. 4.4 and 4.5. The lens radius was fixed to $R_{\text{lens}}/R_{\text{lens,max}} = 95\%$ according to the mould design of the first microlens implementation, and the efficiency of the low-field region set to $\varepsilon_{\text{LFR}} = 60\%$. The residual height was varied for values $H_{\text{res}} = \{5, 10, 15, 20\}\,\mu\text{m}$. The limitation from the manufacturing process imposes a minimal thickness of approximately 8 µm, which is difficult to achieve for larger array productions.

For both fill factors the improvement in light yield is greater for the measured angular distribution than for the simulated one. The light yield obtained with the simulated exit angle distribution is more sensitive to the residual height, which means that H_{res} has to be kept as thin as possible ($H_{\text{res}} = 10\,\mu\text{m}$). The light yield obtained with the measured exit angle distribution is less sensitive to the residual height, which can be about 5 µm thicker and relaxes the manufacturing constraints.

Table 4.4 – Simulation results for different residual heights H_{res} for a 40µm × 40µm pixel with a GFF = 50.0%. The efficiency of the low-field region was set to ε_{LFR} = 60%. The statistical uncertainty of the obtained $EGFF_{4.5}$ and G_{LY} values is 0.95% and 0.96%, respectively.

Angular distribution	H_{res} (µm)	$EGFF_0$ (%)	$EGFF_{4.5}$ (%)	G_{LY} (%)
measurement	5	44.6	63.1	41.5
	10	44.7	68.2	52.5
	15	44.7	69.9	56.5
	20	44.6	67.9	52.3
simulation	5	44.6	63.4	42.0
	10	44.7	65.0	45.6
	15	44.9	62.1	38.4
	20	44.8	58.2	29.9

Table 4.5 – Simulation results for different residual heights H_{res} for a 40µm × 40µm pixel with a GFF = 82.4%. The efficiency of the low-field region was set to ε_{LFR} = 60%. The statistical uncertainty of the obtained $EGFF_{4.5}$ and G_{LY} values is 0.79% and 0.80%, respectively.

Angular distribution	H_{res} (µm)	$EGFF_0$ (%)	$EGFF_{4.5}$ (%)	G_{LY} (%)
measurement	5	75.5	88.0	16.5
	10	75.5	93.2	23.5
	15	75.5	93.6	24.0
	20	75.5	89.4	18.3
simulation	5	75.3	89.8	19.2
	10	75.5	90.6	19.9
	15	75.6	88.3	16.8
	20	75.7	83.2	9.9

4.5.3 Simulation outcome

According to our studies, the optimal parameters for a microlens implementation on 40µm × 40µm pixels with a fill factor of GFF = 82.4% are:

- $R_{\text{lens}} = 26.87\,\mu\text{m}$
- $H_{\text{lens}} = 20.15\,\mu\text{m}$
- $H_{\text{res}} = 10\,\mu\text{m}$

These SiPM parameters correspond to the ones used for the first microlens implementation on available SiPMs described in detail in Chapter 5.

The results have been confirmed by the microlens manufacturer *Centre Suisse d'Electronique et de Microtechnique* (CSEM) [127], where another ray-tracing study with a commercial software (Zemax OpticStudio [128]) has been performed for verification, using the exit angle distribution described in Appendix A. Modelling the microlens with these optimal parameters, CSEM confirmed a possible 25.4% improvement of a microlens-enhanced SiPM over a SiPM without microlens, compared to 23.2% improvement obtained with the simulation of Sec. 4.5.

4.6 Best projection for future implementations

In view of new available silicon, future SiPMs at the LHCb SciFi Tracker will most likely have a pixel size between 30 µm × 30 µm and 40 µm × 40 µm, with a GFF of approximately 75%. The study described below gives a projection of the optimisation of the microlens parameters for such an implementation with a pixel size of 40 µm × 40 µm. The angular distribution for long fibre mats is assumed to be close to the narrow, measured distribution in Sec. 4.2.2.

The optimal microlens parameters have been determined for two lens radii and two low-field region efficiencies, varying the residual heights. The results are listed in Table 4.6. The highest gain is observed with a lens of $R_{\text{lens}}/R_{\text{lens,max}} = 95\%$ yielding an expected improvement of 31.2% with a residual height $H_{\text{res}} = 15\,\mu\text{m}$ for a 60% efficient low-field region, and 24.7% with a residual height $H_{\text{res}} = 10\,\mu\text{m}$ for a fully efficient pixel.

Table 4.6 – Simulation results for a pixel size of 40 µm × 40 µm with a GFF = 75%. The results are obtained with the narrow (measured) exit angle distribution. The statistical uncertainty of the obtained $\text{EGFF}_{4.5}$ and G_{LY} values is 0.27% and 0.28%, respectively.

ε_{LFR} (%)	$R_{\text{lens}}/R_{\text{lens, max}}$ (%)	R_{lens} (µm)	H_{res} (µm)	EGFF_0 (%)	$\text{EGFF}_{4.5}$ (%)	G_{LY} (%)
60	95	26.87	10	68.4	89.7	31.0
		26.87	15	68.4	89.8	31.2
		26.87	20	68.4	86.3	26.0
	90	25.46	10	68.4	89.6	30.9
		25.46	15	68.4	88.1	28.7
		25.46	20	68.4	85.1	24.3
100	95	26.87	10	75.0	93.6	24.7
		26.87	15	75.0	93.4	24.5
		26.87	20	75.0	90.4	20.6
	90	25.46	10	75.0	93.0	23.9
		25.46	15	75.0	91.4	21.8
		25.46	20	75.0	88.5	18.0

5 Implementation and testing of microlens-enhanced SiPMs

The first microlens-enhanced SiPMs were produced in 2021 after positive results were obtained from the simulation discussed in Chapter 4. The lenses were designed and deposited by CSEM on already available multichannel SiPM arrays provided by FBK. The SiPMs have a channel segmentation appropriate for a SciFi Tracker readout and a very high fill factor (GFF = 82.4%). Several difficulties during the demoulding process as well as faulty electronic connections on the SiPMs lead to only two devices that could be tested as all channels in a die need to be working to measure the light yield: one reference die with a uniform 30µm thick (flat) residual layer and one microlens-enhanced die. The comparison of the light yield measurement between these two detectors showed a significant improvement of the microlens sample over the flat one.

A second prototyping campaign was therefore performed in 2022 using the same SiPM technology but with two fill factors (GFF = 50.0% and GFF = 82.4%). The microlenses alignment with respect to the pixel geometry for this iteration and the microlens production, in particular the demoulding process, were improved. The light yield measurement was repeated on 16 SiPM arrays (eight with implemented microlenses, four with a flat residual layer and four with the bare silicon surface exposed).

This chapter describes in detail the chosen SiPM samples including their characterisation in terms of correlated noise and PDE, the microlens design and production steps, as well as the results of the light yield comparison between SiPMs with and without microlenses for the two iteration steps.

5.1 Characterisation of FBK2019-10ch SiPMs

10-channel SiPMs of near-UV high density (NUV-HD) technology with deep trenches filled with silicon dioxide for optical and electrical isolation [129] have been provided by FBK for testing. They are from now on referred to as FBK2019-10ch. These devices (not customised for LHCb SciFi Tracker) are equipped with alignment markers necessary for a microlens implementation. The samples have a pixel size of 40 µm × 40 µm and are available with two pixel layouts: GFF = 50.0% and GFF = 82.4%. Single channels (width of 320 µm and height of 3.12 mm) of both fill factors are characterised in terms of correlated noise and PDE.

5.1.1 Correlated noise determination

With the waveform analysis the correlated noise probability (direct crosstalk (DiXT), delayed crosstalk (DeXT) and afterpulse (AP)) is determined as a function of the overvoltage ΔV. One SiPM channel is connected to a 20 dB amplifier* and read out with an oscilloscope†. A large number of waveforms is acquired for every bias voltage setting while triggering on dark noise with a trigger threshold of 0.5 PE.

The waveforms are analysed offline using ROOT. In the first step, the breakdown voltage V_{BD} is calculated using the amplitude spectrum. For every bias voltage the 1 PE-pulse amplitude $A_{1\,\mathrm{PE}}$ is fitted with a Gaussian distribution‡, and is used for the calibration of the amplitude to photoelectrons (PE). The linear extrapolation of the mean amplitudes to zero returns the V_{BD}, which is shown in Fig. 5.1 for GFF = 50.0% and GFF = 82.4%.

The converted PE peaks are then categorised into DiXT, DeXT and AP according to amplitude and time thresholds, which depend on the SiPM type. They need to be evaluated and serve as input to the analysis. An example of the used parameters for the correlated noise characterisation of FBK2019-10ch are given in Table 5.1.

*FEMTO high speed GHz amplifier series HSA with bandwidth up to 2.5 GHz

†Teledyne LeCroy WavePro 254HD with 2.5 GHz bandwidth

‡The width of the photon peak is due to gain fluctuations between pixels on the SiPM, and is well described by a Gaussian distribution.

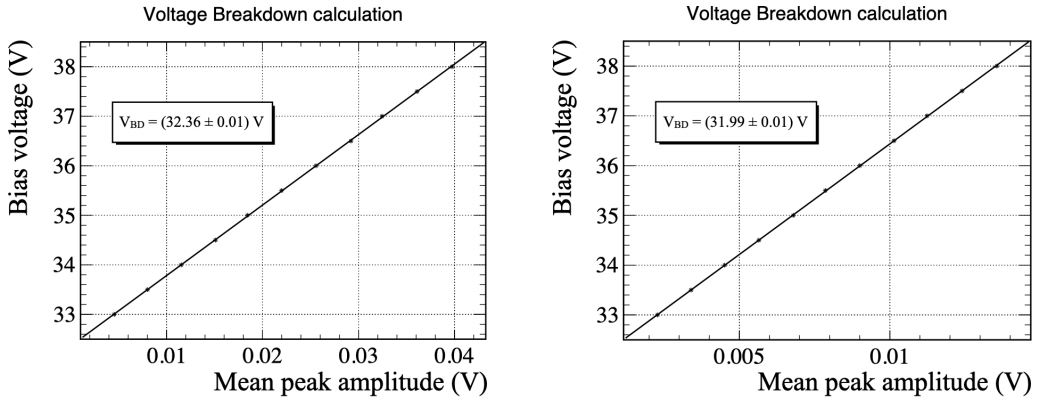

(a) (b)

Figure 5.1 – Examples of a single channel V_{BD} determination of FBK2019-10ch devices with (a) GFF = 50.0% and (b) GFF = 82.4% using the waveform analysis. The precise knowledge of V_{BD} is needed to compensate sample-to-sample variations and temperature fluctuations. Note that the sample with GFF = 50.0% has a metal mask which acts as an additional capacitance in parallel to R_q. This enhances the fast component of the pulse shape and leads to a higher pulse amplitude.

The correlated noise probabilities for both fill factors are shown in Fig. 5.2. The sample with GFF = 50.0% shows a total correlated noise of 15% at $\Delta V = 6$V, and has a prominent AP contribution. The maximum operational voltage is thus set to $\Delta V = 4$V, using a limit of total correlated crosstalk of 10%. The sample with GFF = 82.4% shows already at a low overvoltage of $\Delta V = 3$V a high total correlated noise that reaches 20%, making the peak detection with this threshold-based algorithm difficult. The detector is henceforth not operated above $\Delta V = 3$V. The very high correlated noise probability indicates that the fill factor of this detector has been pushed beyond the acceptable limit, and is an example that a GFF of 82.4% with this technology is not viable.

Table 5.1 – Typical amplitude (A) thresholds and time (t) windows for the wavelength analysis. The time windows for the two pixel layouts are slightly different for the DeXT detection.

Correlated noise	Amplitude threshold both GFFs	Time window GFF = 50.0%	Time window GFF = 84.2%
DiXT	1.20 PE $< A$	0.0 ns $< t <$ 1.1 ns	0.0 ns $< t <$ 1.5 ns
DeXT	0.85 PE $< A <$ 1.90 PE	1.1 ns $< t$	1.5 ns $< t$
AP	0.60 PE $< A <$ 0.85 PE	10.0 ns $< t$	10.0 ns $< t$

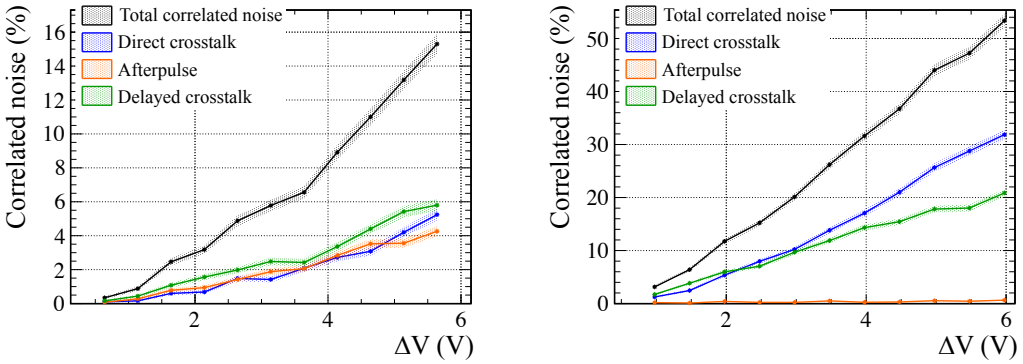

Figure 5.2 – Correlated noise probability for FBK2019-10ch with (a) GFF=50.0% and (b) GFF=82.4%. The correlated noise probability allows to evaluate the useful operational range, which is up to $\Delta V = 4\,\mathrm{V}$ for GFF = 50.0% and up to $\Delta V = 3\,\mathrm{V}$ for GFF = 82.4%.

5.1.2 Measurement of the photon detection efficiency

The PDE is measured on single dice with a flat, 500 µm thick silicone resin coating for both pixel technologies. The method and measurement setup to determine the PDE via Eq. 5.1 are described in detail in Ref. [130]. In contrast with a PDE measurement where correlated noise corrections need to be applied, this measurement shows very little bias even at high ΔV.

As mentioned in Sec. 2.4.2, the PDE is the probability to detect the impinging photons on the photodetector. It can be expressed by:

$$\mathrm{PDE} = \frac{(N_\mathrm{L} - N_\mathrm{D})}{N_\mathrm{i}} = \frac{N_\mathrm{F}}{N_\mathrm{i}}, \tag{5.1}$$

where N_L and N_D are the average rates of cells firing in light or dark condition, N_F is the rate of cells firing not caused by correlated noise, and N_i is the average rate of incident photons. The measurement is based on the fact that in a charge spectrum the zero-photon (or pedestal) peak is not influenced by correlated noise, and can thus be used to determine the probability of non-firing cells in light (P_L) and dark (P_D) conditions using Poisson statistics:

$$P_\mathrm{L} = \frac{(N_\mathrm{L})^0 \mathrm{e}^{-N_\mathrm{L}}}{0!} = \mathrm{e}^{-N_\mathrm{L}}, P_\mathrm{D} = \mathrm{e}^{-N_\mathrm{D}}. \tag{5.2}$$

The intensity of the LED pulse is set such that the large majority of events shows no detected photons in a typical time integration interval of 380 ns. N_i is measured with a calibrated

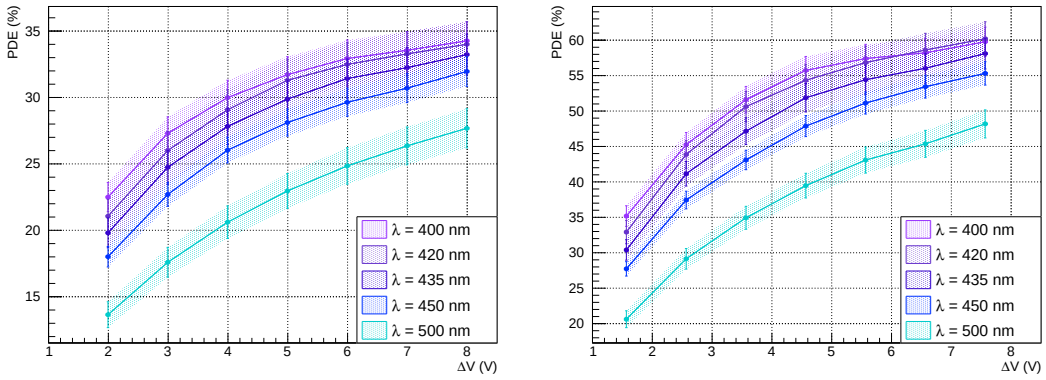

(a) (b)

Figure 5.3 – The photon detection efficiency of FBK2019-10ch used for the microlens prototyping with (a) GFF=50.0% and (b) GFF=82.4%. Note that due to the high crosstalk the maximum overvoltage is at $\Delta V = 4\,\mathrm{V}$ for 50.0% and at $\Delta V = 3\,\mathrm{V}$ for 82.4%.

reference photodiode. An integrating sphere ensures a uniform distribution of the photons across the photodiode and the SiPM, which is positioned at a calibrated distance from the sphere. From the probabilities, P_L and P_D of non-firing pixels, N_F is calculated using:

$$N_\mathrm{F} = -\ln(P_\mathrm{L}) - (-\ln(P_\mathrm{D})). \tag{5.3}$$

Finally, the PDE is determined by dividing N_F by the average rate photons impinging on the photodetector N_i.

The PDE is measured for five wavelengths $\lambda = \{400, 420, 435, 450, 500\}$ nm, and the results are shown in Fig. 5.3. For a wavelength of $\lambda = 450\,\mathrm{nm}$, the PDE reaches a value of 23% at $\Delta V = 3\,\mathrm{V}$ for GFF = 50.0% and 40% at $\Delta V = 3\,\mathrm{V}$ for GFF = 82.4%.

5.2 Microlens production

Microlenses can be produced with various techniques, depending on the chosen microlens material. For example, microlens arrays made from fused silica are typically fabricated via reactive ion etching, whereas microlenses made of epoxy can be produced with microjet printing [131]. In this method, droplets are directly placed on the substrate and UV-cured. It was explored for the first trial of microlens-enhanced SiPMs for the LHCb SciFi Tracker, as described in Ref. [97], but failed due to the non-flat SiPM surface.

The method used by CSEM for this production relies on photolithography and thermal reflow, and is typically used for microlenses made of polymer. With this method, microlens diameters as small as 4 µm can be achieved [132]. The production process is divided into three steps, shown in Fig. 5.4: the implementation of a masterlens array, the master mould fabrication, and the final microlens deposition on the SiPMs.

1. The photoresist layer is placed on top of a substrate, and exposed to UV light. A mask above the resist shields the material in places where the lenses are formed, determining the diameter and the gap between lenses. The height of the resist equals the height of the lens. This method constrains the height of objects to be equal for the full area. After UV-exposure, the photoresist can be removed everywhere except where microlenses are built, and the hardened remaining photoresist structures are melted at 150–200 °C (depending on the used polymer), forming the master lens array (spherical and cylindrical surfaces can be produced).

2. The master lens array is then pressed into a UV-curable material to form the master mould. After UV-exposure, the master mould is obtained. The master mould can be reused for several reproduction steps. Any damages such as scratches or misalignments will be present for every reproduction.

3. In the final production step, the silicon substrate is covered with a UV-curable material. The master mould is pressed onto the polymer, UV-cured and demoulded, yielding the final microlens-enhanced photodetector. The limitation of the residual layer thickness depends on the total mould surface and the applied force. This is a critical parameter in the fabrication process.

The chosen material is called Lumogen OVD Varnish produced by BASF, with a refractive index of 1.52 at a wavelength of 450 nm [133]. The material has a high transmission for the spectrum of the SciFi application and has been qualified for the radiation environment range of space applications.

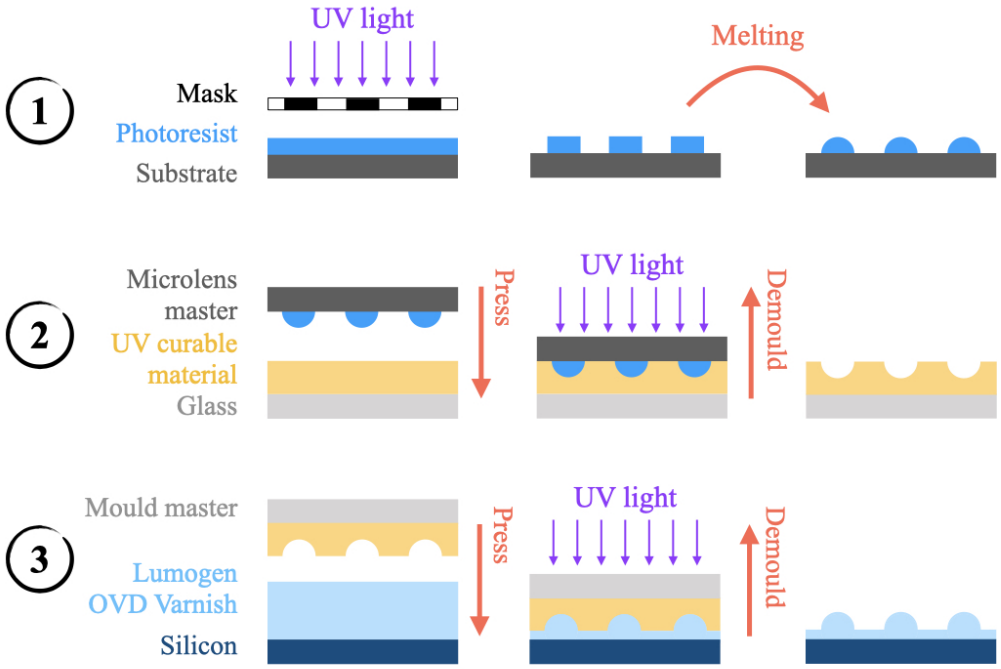

Figure 5.4 – The three production steps based on photolithography and thermal reflow to produce microlenses on an SiPM. In Step 1, master lens structures are produced, which are used in Step two to fabricate the master mould. In Step 3, the microlenses are deposited on the SiPM using the mould master. *Picture inspired by Ref. [132].*

5.2.1 Microlens design

The microlens parameters for the implementation on FBK2019-10ch SiPMs were determined by CSEM with a commercial software. The simulation was performed with an earlier version of the exit angle distribution measurement with a mean value between the simulated (Sec. 4.2.1) and the measured (Sec. 4.2.2) one, resulting in small variations of the optimal parameters described in Sec. 4.5.3. The final lens parameters are as follows [134]:

- $R_{\text{lens}} = 25.78\,\mu\text{m}$
- $H_{\text{lens}} = 20\,\mu\text{m}$
- $H_{\text{res}} = (8 \pm 3)\,\mu\text{m}$

These values are close to the ones used in Chapter 4 with $R_{\text{lens}} = 25.46\,\mu\text{m}$, $H_{\text{lens}} = 19.1\,\mu\text{m}$ and $H_{\text{res}} = 10\,\mu\text{m}$. The small difference in lens height of $1\,\mu\text{m}$ between implemented and simulated value is negligible compared to the lens radius which has a bigger influence on the

improvement in light yield. Therefore these values are used for the comparison between the outcome of the simulation and the outcome of the measurement in Sec. 5.6.

Four different microlens array structures have been implemented on different regions of the master mould. This allowed the fabrication of the four versions shown in Fig. 5.5. The flat layer in Fig. 5.5a is covering the complete SiPM surface and has the same thickness as the microlenses plus the residual height (approximately 30µm). This design is used for the light yield measurement (described in detail in Sec. 5.4) as reference die (from now on referred to as flat).

In Fig. 5.5b the complete silicon surface is covered with spherical microlenses. In the design of Fig. 5.5c, two spacer regions are implemented. The spacer is implemented to protect the microlenses from being damaged when a microlens-enhanced SiPM is pressed against the fibre mat. The spacer has a larger surface and thus redistributes the force. It is made of cylindrical lenses implemented on two sides covering an area of 500µm × 3200µm on the top and the bottom of the SiPM. They have the same height as the spherical microlenses. A final lens array without spacer but only with the flat residual layer is depicted in Fig. 5.5d. The thickness of this layer corresponds to the implemented residual height thickness. It can be designed to evaluate the need of a spacer.

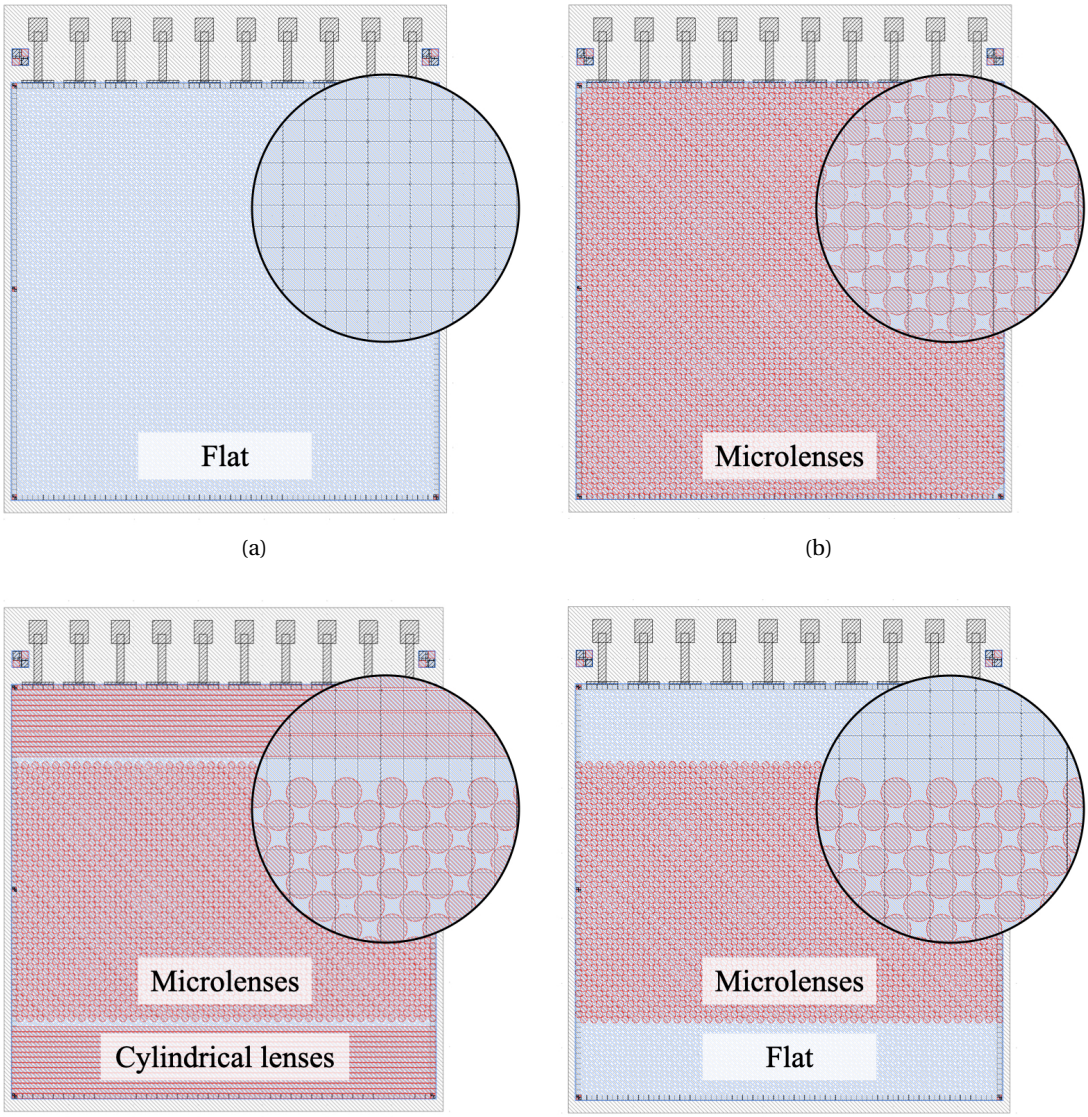

(a) (b)

(c) (d)

Figure 5.5 – The four different array structures: (a) array with a uniform flat spacer, (b) full SiPM array covered with spherical lenses, (c) array with spherical and cylindrical lenses used as spacer, and (d) array covered with spherical lenses and a flat residual layer. *Picture taken from Ref. [134].*

5.2.2 Packaging and optical coupling

The photodetectors are wire-bonded on a carrier PCB and connected to Kapton flex cables designed for the LHCb SciFi Tracker. The PCB (Fig. 5.6a) can accommodate four FBK2019-10ch dice and has a couple of alignment pins at the edges to align the SiPMs to the fibre mat.

The sideview of the SiPMs coupled to the fibre mat is shown in Fig. 5.6b. A 1 mm deep wedge is cut into the fibre mat endpiece to accommodate the bond wires present at the top edge of the SiPM. In a future development for LHCb, a Through-Silicon-Via (TSV) technology is the preferred option as bondwires are delicate to handle and require additional silicon areas. In TSV, the SiPMs are bump-bonded onto the PCB, avoiding bond wires completely and thus simplifying the packaging. Current TSV implementations by FBK however require a mm-thick glass substrate on top of the silicon for stabilisation, which is incompatible with microlenses.

The PCB is positioned on a holder equipped with adjustment screws to apply a defined coupling pressure for each of the four dice individually. In this way, differences in the die thickness due to the different surfaces can be mitigated and the same optical coupling ensured.

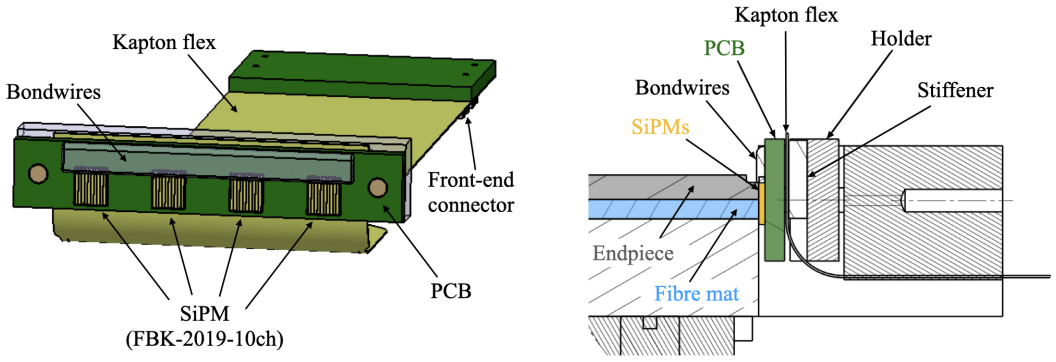

(a) (b)

Figure 5.6 – CAD drawings of (a) the Kapton flex with a dedicated PCB for bonding four multichannel arrays and (b) the interface between the fibre mat and the SiPMs.

5.3 Testing of the radiation hardness of the microlens material

In view of the expected ionising dose during Run 5 and beyond, the radiation tolerance of the microlens material has been tested in a dedicated irradiation campaign performed at the cyclotron of Bern University Hospital [135]. The cyclotron is primarily used for medical applications, but is also available as an irradiation facility for research.

The cyclotron provides a uniform beam of protons with an energy of 18 MeV. The protons are extracted using a 1 cm square collimator, on which the current is measured. The remaining proton current after the collimator is the difference between the beam current and the charge current measured at the collimator, and it is used to calculate the dose. After a 300 µm thick aluminium extraction window, the protons have an energy of 16.7 MeV.

Two 1 mm thick samples of the BASF Lumogen OVD Varnish have been produced on a glass substrate for the irradiation campaign. The samples have been mounted on plastic support structures with Kapton tape. They are divided into four regions, indicated by white vertical and horizontal lines indicated on the support structure. Each region has received a different radiation dose of {0, 1, 10, 100} kGy. The high radiation doses have been chosen to ensure the material can withstand a dose far beyond the expected ~ 1 kGy received by SiPMs in the LHCb SciFi Tracker at the end of Run 5.

The proton flux has been determined by dividing the remaining proton current after the collimator by the area of the collimator. To reach the required doses, the necessary proton fluence has been calculated using the following relation:

$$\text{dose} = \text{fluence} \cdot \text{ESP}, \tag{5.4}$$

where ESP is the electronic stopping power of protons in a given material. Polystyrene is used as a reference material for the microlens substrate, with an ESP $= 29.66$ MeV cm^2/g for the proton energy of 16.7 MeV as provided by Ref. [136].

Figure 5.7 shows the samples after the irradiation. The blue radiographic film marks the areas of the irradiation. A spectral transparency measurement of the microlens material has been performed at CSEM. The relative decrease in transparency of an irradiated sample with respect to the non-irradiated one is shown in Fig. 5.8. Note that the measured material is 30 times thicker than the thickness of the implemented microlenses (1 mm compared to 30 µm). The measurement therefore confirms the suitability of the material in the radiation environment at the LHCb SciFi Tracker, with an attenuation of 5% over 1 mm at 10 kGy and 450 nm. This corresponds to 0.17% over 30 µm.

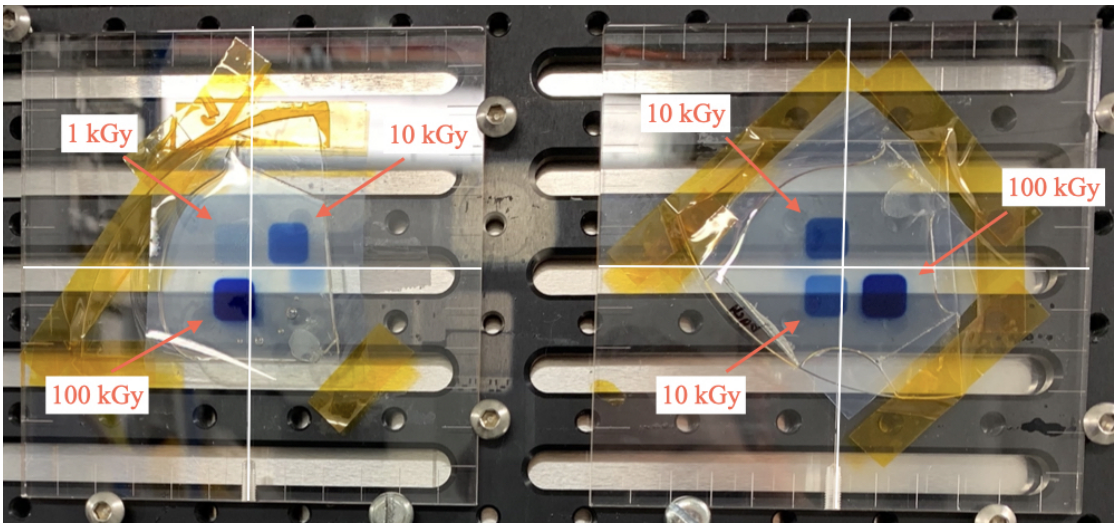

Figure 5.7 – Two Lumogen OVD Varnish substrates after irradiation. The samples have been divided into four regions indicated by the white vertical and horizontal lines on the plastic support. Note that the colouring in this picture does not reflect the change in transparency. The darker the radiographic film, the higher the received dose of the sample. For the sample on the right a wrong dose was applied in one of the areas.

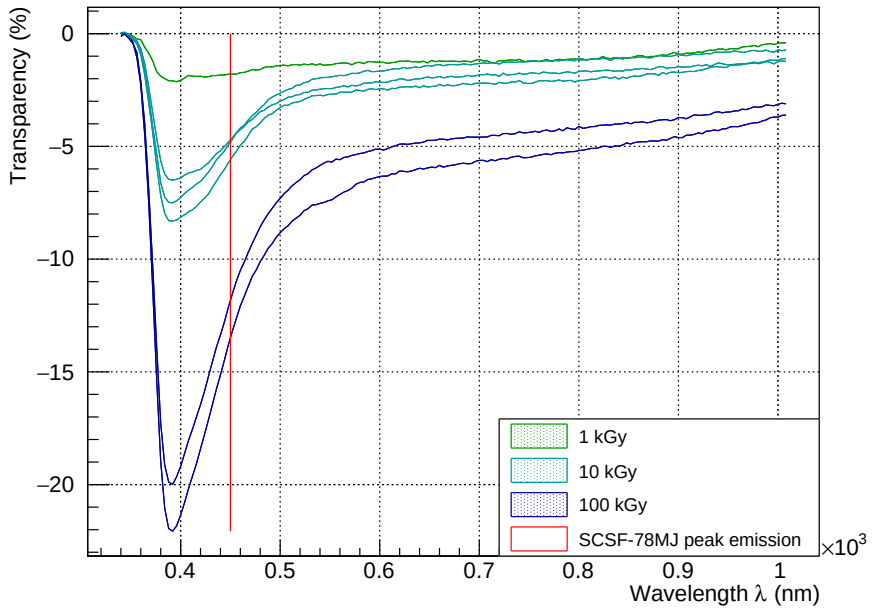

Figure 5.8 – Result of the relative transparency measurement of the microlens material BASF Lumogen OVD Varnish after irradiation at $\{1,\ 10,\ 100\}$ kGy with respect to the non-irradiated sample. The red line indicates the peak emission spectrum of the SCSF-78MJ scintillating fibre of the LHCb SciFi Tracker. *Picture plotted with data from Ref. [137].*

5.4 Light yield measurement setup and method

The light yield (LY) for the SciFi Tracker is defined as the number of detected photons for a minimum ionising particle. It is one of the most important parameters for the global characterisation of a SciFi module (composed of the SciFi mat and the SiPMs) and is the ultimate test for microlens-enhanced SiPMs.

5.4.1 Measurement setup

To compare the light yield of detectors placed at different positions of the fibre mat, a homogeneous and reproducible signal source is important. A light injection system does not fulfil this condition. For this setup, an electron gun made of a small β-spectrometer with a ^{90}Sr radioactive source and a solenoid coil to select electrons of 1 MeV has been used. The electron gun provides a trigger to the data acquisition (DAQ) electronics: electrons traversing three 1 mm-thick square plastic scintillating fibres and a SiPM readout will give a synchronous trigger signal. In the DAQ the analog signal is converted to a digital signal with a analog-to-digital converter (ADC). The measurement is performed in a dark room. The electron gun is mounted on a moving stage and injects electrons across the 13 cm-wide fibre mat. The mat is made of seven layers of scintillating fibres and a mirror is glued on the far side of the fibre mat.

The signal readout is performed with electronics based on the VATA64 front-end ASIC [138]. The charge-integrating amplifier has a linear response with respect to the input charge and a shaping time of $\tau_{\text{shaping}} = 200\,\text{ns}$. In this setup 128 SiPM channels are read out at the same time. Two flex PCBs, each with four SiPMs, can be coupled to the fibre mat at the same time.

The data taking consists of two steps:

1. With a random internal trigger and unbiased SiPMs the pedestal (zero signal offset) is recorded. It will be subtracted from the signal to define the zero-charge amplitude.
2. Using the trigger from the electron gun, the particle-induced signal of the fibre mat is acquired.

The room temperature has been monitored during the measurement, and has been stable up to $\pm 1\,^{\circ}\text{C}$.

The electron gun is positioned at the middle of each 3.2 mm wide die for the duration of the voltage scan, and is then moved to the next die on the PCB. This ensures an efficient DAQ mode. The particle injection is done approximately 10 cm from the SiPMs to suppress highly attenuated modes inside the fibre.

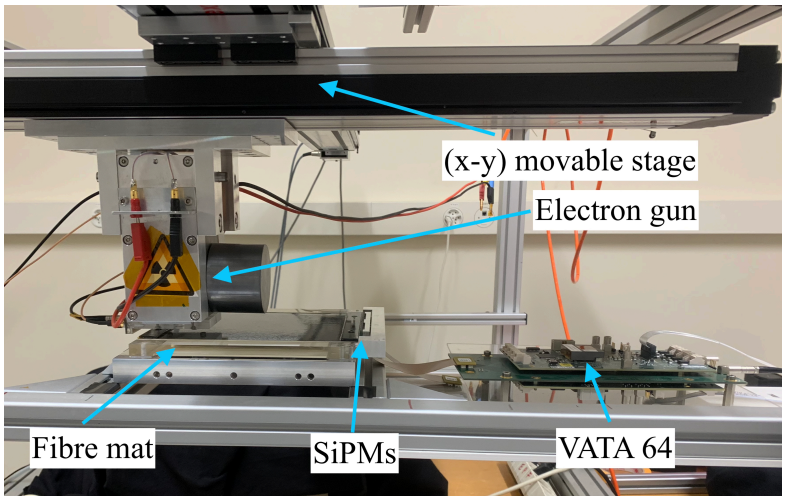

Figure 5.9 – Setup for the light yield measurement of a short fibre mat module in a dark room. The electron gun injects particles at several positions of the fibre mat at a 10 cm distance from the SiPMs, which are read out with electronics based on the VATA64 ASIC.

5.4.2 Data analysis

The two-dimensional charge histogram (ADC value against the channel number) of Fig. 5.10a shows the pedestal-subtracted data. In this case the electron gun was centred on die 1. Fig. 5.10b shows the charge amplitude spectrum of one channel of die 1 with a vertical logarithmic scale. The 0 PE peak is centred around 0 ADC value as the pedestal is already subtracted. Afterpulse and/or crosstalk are visible as signal to the right of each photon peak.

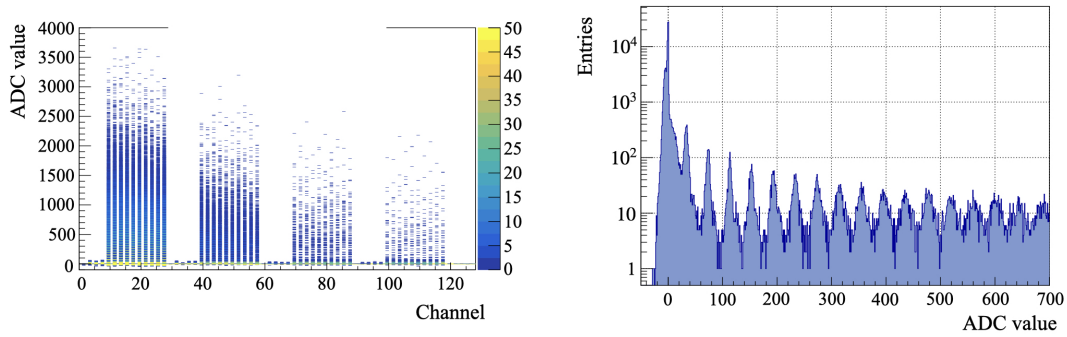

(a) (b)

Figure 5.10 – Single amplitude histogram for a data acquisition where the electron gun is centred at die 1. The four dice are clearly distinguishable in (a). As the dice are only bonded on one side, the ten channels are only connected to even channels on the flex PCB. The projection of one channel in (b) is the charge amplitude spectrum.

Gain calibration and breakdown voltage determination

The SiPM gain is calculated as the mean value of the distance between photon peaks, and is given in ADC value per photon peak, i.e. ADC/PE. The breakdown voltage is determined by a linear fit of the gain at different bias voltages, which is extrapolated to zero gain.

As particles induce a signal only in a few SiPM channels at a time, most channels will see zero charge per event. The signal amplitude distribution in Fig. 5.10b is far from ideal for a fit. For the gain calibration a laser set at low intensity is therefore used. To ensure a uniform light injection across all ten SiPM channels, the laser is diffused and placed at a large distance. As seen in Fig. 5.11a, the charge amplitude spectrum recorded with a laser allows for an automated fit of the photon peaks. In contrast, the spectrum in Fig. 5.10b recorded with a source requires manual fit parameter adjustments. With an extrapolation of the linear fit of the ADC values against the photoelectron peaks (Fig. 5.11b), the gain is obtained in ADC/PE.

The gain in ADC/PE is then plotted against the bias voltage to determine the breakdown voltage of each channel. The precise knowledge of the breakdown voltage allows to compensate for temperature variations and determines the overvoltage. The breakdown voltage of one die is calculated as the average of the breakdown voltages of all 10-channel SiPMs. The adjustment of V_{bias} is performed with respect to the mean V_{BD} per die. The conversion between ADC and PE is done for every channel and is used for the signal amplitude unit in the offline data analysis (performed in ROOT).

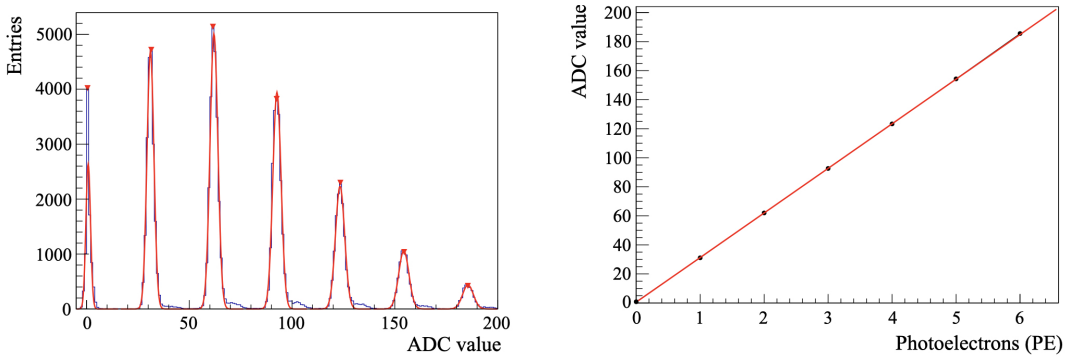

(a) (b)

Figure 5.11 – Gain calibration for one SiPM channel. (a) The photon peaks are each fitted with a Gaussian distribution. (b) The mean ADC value of the Gaussian fit as a function of the number of photoelectrons.

Clustering algorithm

Neighbouring signal channels are grouped into clusters with a clustering algorithm similar to the one described in Sec. 3.5. The algorithm used here profits from an amplitude measurement, i.e. is not only relying on thresholds but uses the amplitude. This allows a performant post-processing of the data with different threshold settings. In a first step, all channels are scanned to determine if they exceed the seed (middle) threshold. In this case, the neighbouring channels are compared to the neighbouring (low) threshold. A cluster is formed if the sum of all its channel signals, i.e. the sum of seed and neighbouring channels, exceeds the sum (high) threshold. This means that also single channel clusters can be formed. The threshold values used for this light yield measurement are $\{\text{seed}, \text{neighbouring}, \text{sum}\} = \{2.5, 1.5, 4.5\}$ PE.

The most probable value (MPV) of the cluster sum distribution, i.e. the total number of photons in a cluster, is the light yield of the detector. The value is fit with a Gaussian distribution around the peak center. An example of the light yield determination for one FBK2019-10ch SiPM is shown in Fig. 5.12. The high number of low cluster sums comes from an edge effect of the cluster, i.e. light that is not detected due to the size of the die.

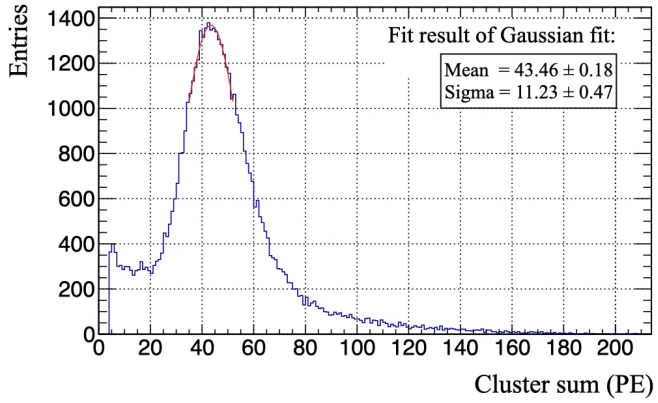

Figure 5.12 – Example of the determination of the light yield for one FBK2019-10ch SiPM at $\Delta V = 3$V. The light yield is given by the most probable value of the distribution of the cluster sum, in this case determined with a Gaussian fit (in red).

Error estimation

Three factors influence the light yield measurement:

- The fit of the V_{BD} determination described above introduces an uncertainty in the range of $\pm 10\,mV$ for all channels. This impacts the ΔV calculation, as well as the gain and the PDE.
- Temperature fluctuations influence the breakdown voltage of the SiPMs, and thus the ΔV, the gain and the PDE. The temperature coefficient of the SiPMs has been measured to be $30\,mV/K$. The operation temperature of the light yield measurements described in the following sections has been constant within $\pm 1°C$, therefore a maximum error of $30\,mV$ on the V_{BD} is assumed. Note that different SiPM types/modules require different temperature coefficients.
- The systematic error of the setup, including inhomogeneity of the fibre mat and differences in the optical coupling, has been determined by measuring the light yield of the same SiPMs (GFF = 82.4%) at two different positions on the fibre mat. It is listed in Table 5.2. A noticeable difference for this systematic estimation between the three surfaces has been detected. Microlens-enhanced SiPMs have the smallest systematic error. They are not as affected by surface flatness variations of the mat as flat or bare dice, because the microlens surface ensures an air gap (touching only at the top of the lens). Furthermore, a smaller systematic error for flat dice compared to bare dice is observed.

The different contributions on the light yield uncertainty are given in Table 5.2. The total relative uncertainty on the light yield is also listed in this table. The total error on the LY is given by the contribution of the combination of V_{BD} and temperature, and the systematics of the setup. The systematic uncertainty is smaller for a higher overvoltage due to the larger number of detected photons and the relative uncertainty on the fit is smaller. The systematics are the determining factor in the final result. Using the average on several independent light yield measurements allows to decrease the systematic error. This was not taken into account for the results in Table 5.2. For the 50.0% samples the systematic error is expected to scale according to the LY, which is given in Table 5.5.

Table 5.2 – Relative uncertainties given by the individual contributions of V_{BD} determination, temperature fluctuations and the systematics of the coupling and the fibre mat. Note that the total uncertainties are calculated with respect to the slope of the SiPMs in Fig. 5.22.

uncertainties	$\Delta V = 1$V	$\Delta V = 3$V
V_{BD}	1.0%	0.25%
Temperature coefficient	3.0%	0.75%
systematics (µL)	2.8%	1.9%
systematics (flat)	4.2%	2.0%
systematics (bare)	5.9%	3.3%
total (µL)	3.6%	2.3%
total (flat)	5.9%	2.2%
total (bare)	7.1%	3.3%

5.5 First prototype iteration

This first prototype production has been crucial for the complete microlens study in this thesis, as it fixed the microlens parameters to the ones described in Sec. 5.2.1. Therefore also the mould design has been fixed, as it has been planned to be reused. This iteration thus also limited the possibilities of the dimensions of the SiPM dice as the mould can only be used for SiPMs with the same layout as the FBK2019-10ch devices. The first microlenses have been produced on five FBK2019-10ch SiPMs with GFF = 82.4% in 2021. The four microlens structures discussed in Sec. 5.2.1 have been implemented on one die and the design of spherical and cylindrical lenses (Fig. 5.5c) on two dice. After the microlens deposition the dice are wire-bonded on a common carrier PCB. The final dice are shown in Fig. 5.13.

Several difficulties have been encountered during the manufacturing process. Air bubbles were present in several regions with deposited microlenses. Moreover, the demoulding of the master mould proved extremely difficult. This was caused by the high density of lenses with a large radius-to-height ratio deposited on a small array, which was completely covered with the microlens substrate [133]. These difficulties resulted in a broken corner of the SiPM with a full microlens coverage (Fig. 5.13a), leaving the sample electrically non-functional. One of the two samples with spherical and cylindrical lenses (Fig. 5.13c) has a very thick residual height of up to $H_{res} = 28$µm, exceeding the requirements. This sample has additionally several non-working channels, and has thus been excluded from the light yield measurement. The flat residual spacer shows delamination effects (Fig. 5.13d), and has additionally two non-working channels. It is thus also excluded from the light yield measurement. This only leaves the reference sample (Fig. 5.13b) with a residual layer thickness of $H_{res} = 20$µm and one sample with spherical and cylindrical microlenses ($H_{res} = 5$µm) for the characterisation

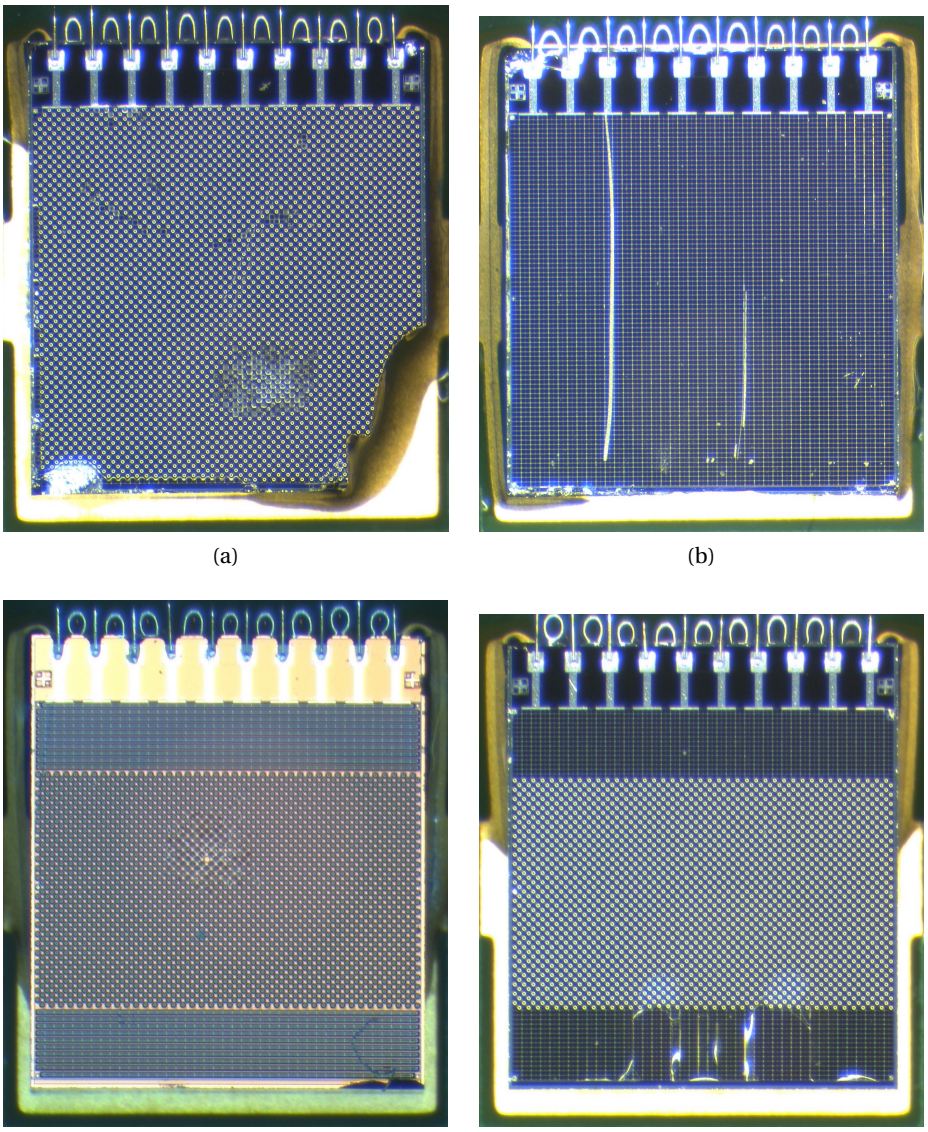

(a) (b)

(c) (d)

Figure 5.13 – The first prototypes of microlens-enhanced SiPMs: (a) full SiPM array covered with spherical lenses, (b) array with a uniform flat spacer, (c) pixels covered with spherical lenses and cylindrical spacers, and (d) pixels covered with spherical lenses and a flat residual spacer. The two samples (a) and (d) have defects due to difficulties in the demoulding procedure (broken corner in (a) and delaminating flat residual layer in (d)). Additionally the samples show several air bubbles.

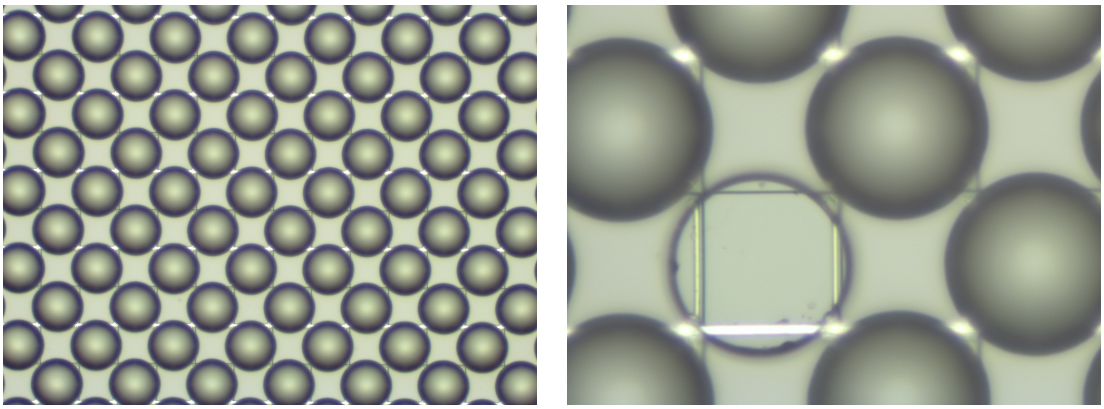

(a) (b)

Figure 5.14 – Zoom on (a) the microlens structure from the first production run and (b) an air bubble, where the misalignment of the microlenses with respect to the pixel can be seen. The air bubble is shifted to the left. The top right corner of the pixel is not covered at all, while the top left corner is fully covered by the air bubble.

measurement. Figure 5.15a shows the close-up of the spherical microlens structure. For all microlens samples a misalignment of the microlenses with respect to the pixels, as shown in Fig. 5.15b, has been observed. Such a misalignment is expected to cause a reduced light yield as the light is not deviated symmetrically towards the pixel centre.

5.5.1 Light yield of the first prototypes

The light yield has been measured for an overvoltage ΔV ranging from 1 V to 2.8 V in steps of 0.3 V. The light yield results are listed in Table 5.3. At low ΔV an improvement of 9% is seen. Nevertheless, the light yield improvement is 1% at high ΔV. In the simulation the improvement for a $H_{\text{res}} = 5\,\mu\text{m}$ thick residual layer and low ΔV amounts to 17% (19%) for the measured (simulated) exit angle distribution. Note that for these simulation results, the lens radius is set to $R_{\text{lens}}/R_{\text{lens,max}} = 95\%$, which is larger than the lenses that are implemented as discussed previously in Sec. 5.2.1.

Possible explanations for the low measured light yield improvement are:

- The fibre exit angle distribution used for the microlens implementation is different than the one used in the simulation. Additionally, the short fibres (14 cm) have a different distribution than the 240 cm-long fibre (see Sec. 4.2.2). At the time of the simulation study, the distribution of a short fibre has not been available. However, taking into account the observed difference of the gain in light yield using the simulated and measured exit angle distributions of 19% and 17%, respectively, this effect is expected to be small.

Table 5.3 – Light yield results for the first iteration of microlens-enhanced SiPMs with GFF = 82.4%.

ΔV (V)	LY reference die (PE)	LY microlens die (PE)	G_{LY}(%)
1.0	26.2	28.6	9
1.3	32.8	34.4	5
1.6	37.9	39.7	5
1.9	42.7	44.5	4
2.2	48.6	49.5	2
2.5	53.1	54.2	2
2.8	59.1	59.5	1

- The dominating effect from the fibre mat is its surface quality. A picture of the cross-section of a non-polished fibre mat (as used for these measurements) is shown in Fig. 5.15. To evaluate the uncertainty on the exit angle distribution as a function of the surface quality a larger campaign is required and could not be performed during the duration of this thesis.
- The alignment between microlenses and pixels will reduce the light yield, as mentioned above.
- Sample-to-sample variations.

The measurement shows that microlenses are effective for low ΔV (9% at $\Delta V = 1$ V), confirming that it is possible to avoid the low-field region. A second prototype iteration has been

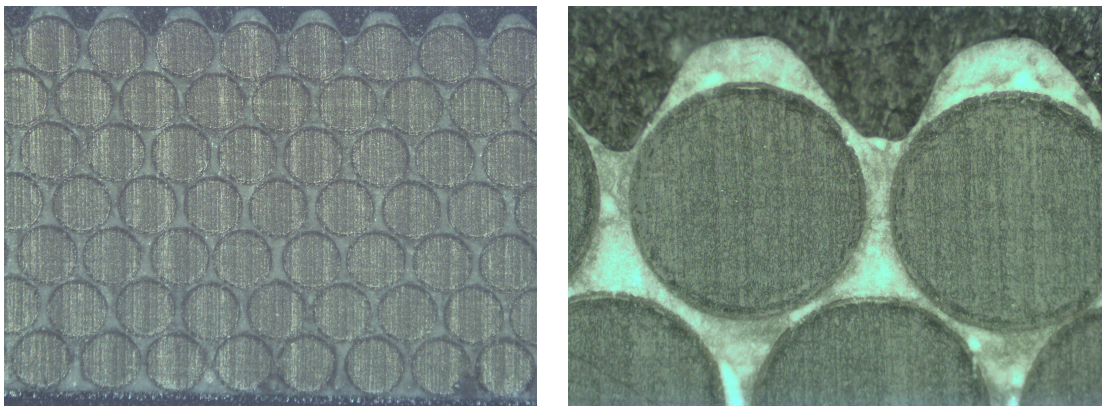

(a) (b)

Figure 5.15 – (a) Cross-section and (b) zoom of a short fibre mat used for the light yield measurements for microlens-enhanced SiPMs.

performed, with a focus on improving the production difficulties, and to produce a larger number of samples.

5.6 Second prototype iteration

The second iteration has been performed in 2022 to increase the number of test samples and improve the alignment of the microlenses with respect to the pixel structure. The second iteration also allowed to achieve a more uniform residual height across all dice, optimising the demoulding procedure to avoid damages on the substrate and minimising the occurrence of air bubbles.

A total of 16 SiPM arrays have been used for this iteration, eight with GFF = 50.0% and eight with GFF = 82.4%. The samples were tested before microlens implementation to reduce the risk of dead channels. For both fill factors, microlenses have been implemented on four dice according to the design in Fig. 5.5c. Two dice have been produced with a flat residual layer and the remaining two dice were left "bare" with only the thin SiO_2 anti-reflective surface coating applied by the manufacturer. The summary of the SiPMs placed on the four used PCBs is given in Table 5.4.

5.6.1 Light yield of samples with 50.0% geometrical fill factor

The light yield has been measured in steps of 0.2 V for an overvoltage ΔV ranging from 1 V to 4 V. A torque screwdriver has been used to ensure all dice were coupled with 2 cNm to the fibre mat.

The light yield of all 16 samples is plotted against the overvoltage in Fig. 5.16. The four microlens samples are shown in orange, the two flat coated samples in blue, and the two bare samples in green. The average light yield of every surface (microlens, flat, bare) has been determined, and is also included in the graph (shown as line of the corresponding surface colour).

Table 5.4 – Prototype assembly of the SiPM chips on the PCB for the second microlens iteration.

PCB no.	GFF (%)	Die 1	Die 2	Die 3	Die 4
1	50.0	flat resin	flat resin	bare (SiO_2)	bare (SiO_2)
2	50.0	microlenses	microlenses	microlenses	microlenses
3	82.4	flat resin	flat resin	bare (SiO_2)	bare (SiO_2)
4	82.4	microlenses	microlenses	microlenses	microlenses

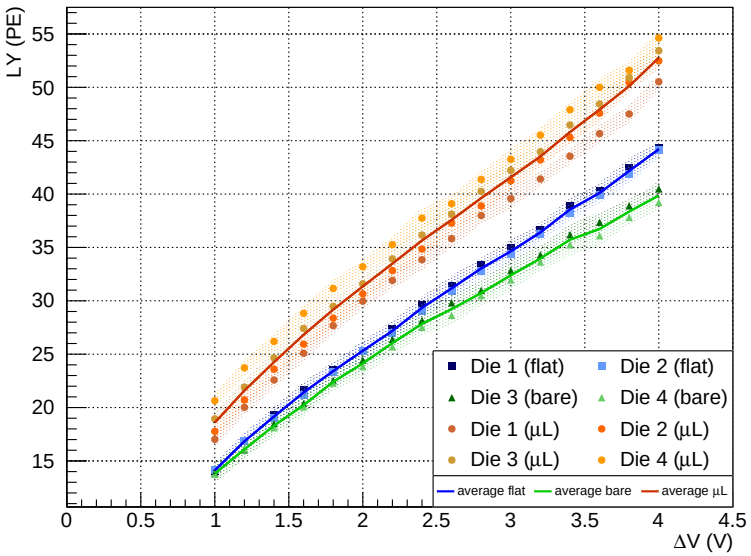

Figure 5.16 – Light yield of FBK2019-10ch with GFF = 50.0%, coupled to the fibre mat with torque of 2 cNm. Three different SiPM surfaces (microlenses, flat, bare) have been evaluated. The microlens-enhanced SiPM shows a clear improvement over flat and bare samples. The shaded regions correspond to the estimated error of each die, and are calculated according to Sec. 5.4.2.

Table 5.5 – Light yield results for SiPMs with GFF = 50.0%, coupled to the fibre mat with torque of 2 cNm.

ΔV (V)	$LY_{\mu L}$ (PE)	LY_{flat} (PE)	LY_{bare} (PE)	$G_{LY,\mu L/flat}$ (%)	$G_{LY,\mu L/bare}$ (%)
1	18.6	14.1	13.8	32	35
2	31.4	25.3	24.1	24	30
3	41.6	34.6	32.4	20	28
4	52.8	44.2	39.9	19	32

A clear difference between the three surfaces is present at all overvoltages. The average light yield at $\Delta V = 1\,V$ of samples with microlenses shows an improvement of approximately 32% (35%) compared to flat (bare) surface, as listed in Table 5.5. With increasing ΔV, the microlens-enhanced dice still reveals an improvement of 19% (32%). Even though the increase at low ΔV is smaller than predicted by the simulation study (which yielded 56% (46%) for measured (simulated) exit angle distribution), it confirms that microlenses are effective to increase the GFF. Possible reasons for the difference are again a slight lens-to-pixel misalignment, the uncertainty of the exit angle distribution of the short fibre mat not introduced in the simulation and dominantly the surface quality of the fibre mat.

To understand and verify assumptions about coating of the silicon, external crosstalk and optical coupling between fibre mat and SiPM, a series of measurements, described in detail below, have been conducted on flat and bare dice. The observed differences are partially a result of the anti-reflective coating, which has been optimised to the refractive index of the top coating (not air) and for which interference can occur due to the structured layer, depending on the angle of the incoming photon [139]. Additionally, external crosstalk (photons reflected on the resin surface back into the SiPM) can potentially be the second reason for the observed difference.

The coupling has been varied between a large air gap and the smallest possible with a high torque of 6 cNm, and the light yield has been measured for both types of coupling. A voltage scan has been performed to evaluate the crosstalk using the ratio of the number of events exceeding the DCR threshold of 0.5 PE and the two-photon threshold of 1.5 PE. The results are shown in Fig. 5.17. External crosstalk is present for the flat die and can partially explain the difference between the two curves seen in Fig. 5.16. At high ΔV the external crosstalk amounts to approximately 3.4%. The "quadratic" increase is due to the higher crosstalk (which has a linear behaviour) and the higher PDE which increases with ΔV. Inefficiency of the anti-reflective coating is likely the second effect that causes the difference between flat and bare.

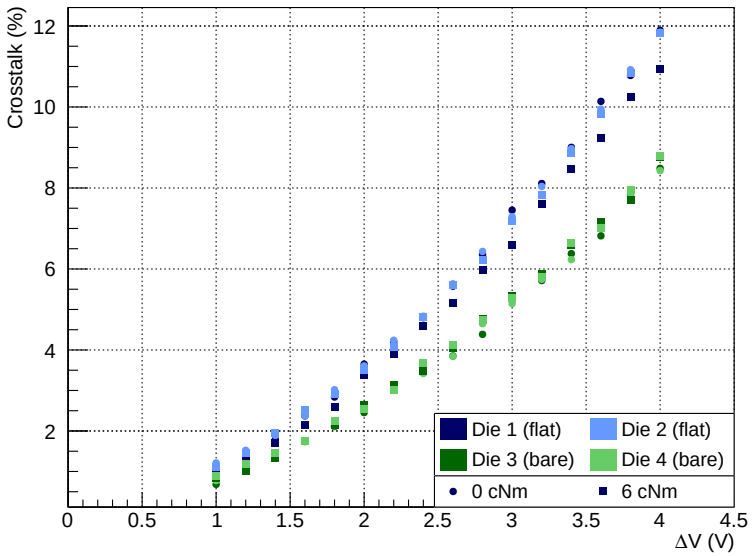

Figure 5.17 – External crosstalk evaluation for flat and bare surfaces, with an air gap between SiPMs and fibre mat (0 cNm) and the highest torque applied (6 cNm). Note the sample-to-sample variation.

5.6.2 Change in cluster size

The cluster size of a SiPM represents the light spread across several SiPM channels. A small cluster size allows to operate the detector at higher track density. An example of the cluster size of a microlens-enhanced die biased at $\Delta V = 3\,\mathrm{V}$ is shown in Fig. 5.18a. The cluster size is influenced by the light yield, the particle type, the optical coupling and the channel width. In Fig. 5.18b, the cluster size is plotted against the weighted mean cluster position. Small cluster sizes occur most often for clusters with a weighted mean position at the border (channel 0 and channel 9). This is because these border clusters consist of fewer channels as light is spread across the not instrumented regions, and thus have a lower light yield.

A small variation of the distance between the fibre mat and the SiPM is introduced when comparing the bare (0µm), flat (15µm) and microlens (40µm) samples. However, with such a small distance no deterioration of the cluster sizes at the same light yield can be detected (Fig. 5.19). This leads to the conclusion that microlenses do not increase the cluster size, but do not improve it either. Note that the cluster size depends highly on the applied thresholds, and therefore the evaluation of the error is difficult.

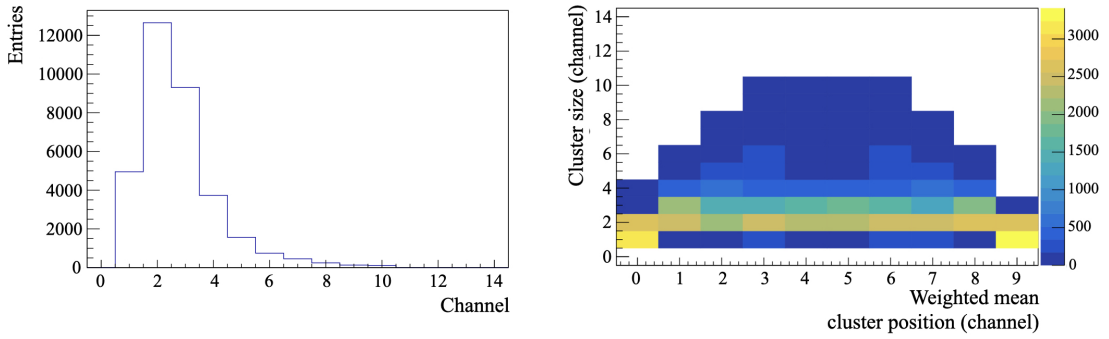

(a) (b)

Figure 5.18 – Example of the cluster size distribution at $\Delta V = 2\,\mathrm{V}$ for (a) a full microlens-enhanced FBK2019-10ch die and (b) the cluster size as a function of the weighted mean cluster position. Small channel sizes occur most often for clusters with a weighted mean position at the borders of the die (channels 0 and 9). For these channels the cluster consists of fewer channels due to missed light outside the active detector region.

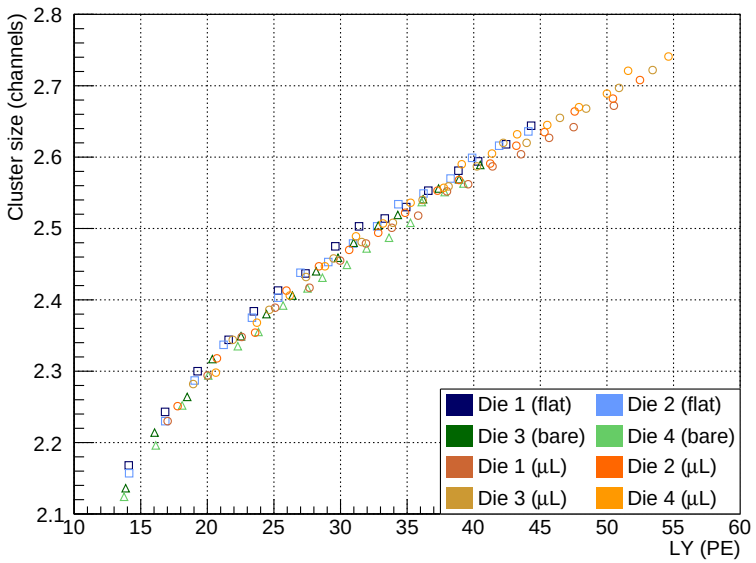

Figure 5.19 – Average cluster size as a function of the light yield for FBK2019-10ch SiPMs with GFF = 50.0%, coupled to the fibre mat with a torque of 2 cNm. No difference is observed between the different samples.

5.6.3 Coupling tests of samples with 50.0% geometrical fill factor

The coupling between SiPM and fibre mat could influence the light yield because of different coupling media and different reflectivity (e.g. ARC coating on the silicon). To study this, different torque values have been applied. Already at 2 cNm, which corresponds to a typical torque applied to these small size screws, the SiPMs are in firm contact with the fibre mat. The torque was increased beyond this to $\{3,4,6\}$ cNm.

For the microlenses, neither light yield (Fig. 5.20) nor cluster size (Fig. 5.21) are significantly affected by the varying pressure. This leads to the conclusion that the microlenses are not deformed and can withstand the applied force without the need of cylindrical spacers. This study also confirms that the measurement is reproducible without any significant statistical variations. Note that the results for $\{2,3,4,6\}$ cNm are completely overlapping.

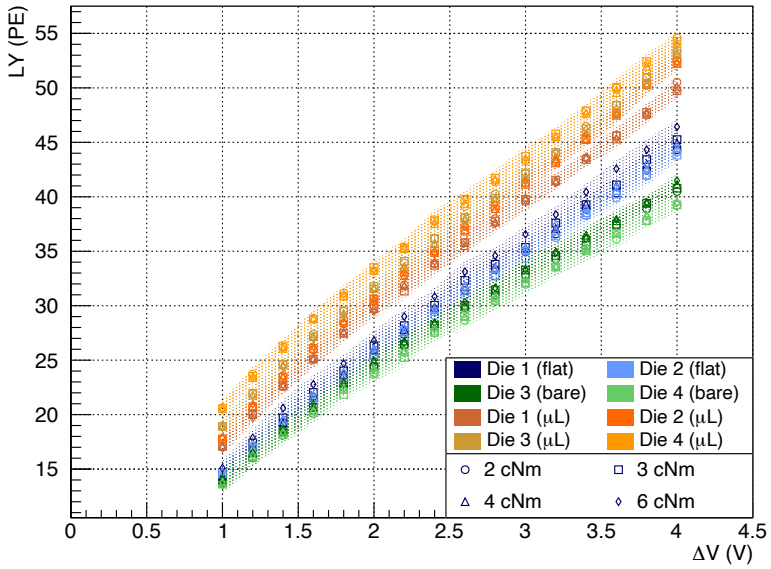

Figure 5.20 – Light yield of SiPMs with GFF = 50.0% coupled to the fibre mat with different torque values. The shaded regions correspond to the estimated error of each die, and are calculated according to Sec. 5.4.2. The light yield remains constant within the systematic uncertainties.

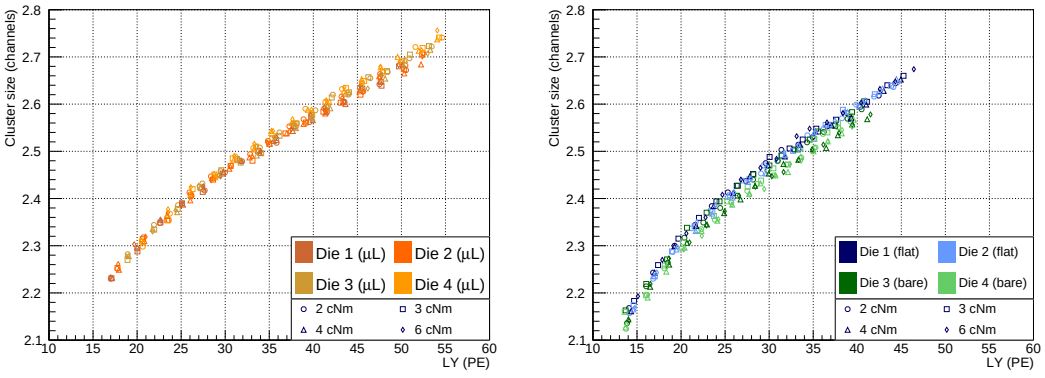

(a) (b)

Figure 5.21 – Cluster size for torque values of {2,3,4,6} cNm for (a) microlens-enhanced and (b) flat and bare SiPMs. Note that the cluster sizes are completely overlapping for different torques.

5.6.4 Light yield of samples with 82.4% geometrical fill factor

The light yield of samples with GFF = 82.4% has been measured following the same procedure as in Sec. 5.6.1, but is limited to a maximal overvoltage of $\Delta V = 3\,\mathrm{V}$. The results are listed in Table 5.6 and shown in Fig. 5.22.

As these samples have a much larger crosstalk than the samples with GFF = 50.0% ones, as discussed in Sec. 5.1.1, the difference in detected light yield between flat and bare samples is increased. Additionally, the larger internal and external crosstalk will lead to a higher light yield, which is confirmed by the measurements and confirms that the difference between flat and bare is indeed partially due to external crosstalk. Within the precision of the measurement, no significant improvement of microlens-enhanced over flat resin samples is observed. The simulation with GFF = 82.4% and the measured exit angle distribution predicts an improvement of 23% ($\varepsilon_{\mathrm{LFR}} = 60\%$) and 17% ($\varepsilon_{\mathrm{LFR}} = 100\%$). Possible explanations for this difference are:

- The sample-to-sample variations for this measurement are much larger than for the GFF = 50.0%, and amount to ±5% at $\Delta V = 2\,\mathrm{V}$.
- The misalignment between microlenses and pixels is more important than for the GFF = 50.0% and reduces the gain significantly. This is due to the fact that a small shift in the microlens position results in a greater area not covered for a larger fill factor.
- The uncertainty of the short fibre mat, including the slightly different exit angle distribution, but more dominantly the effect of the non-polished fibre mat surface will result in a lower improvement.

Therefore, the obtained result of the first prototype iteration (Sec. 5.5) of 9% cannot be confirmed.

However, with the dedicated production of SiPMs (described in Sec. 6.3) with pixel sizes of 31 µm × 31 µm and 42 µm × 42 µm, the GFF will reach approximately 75.0% and 81.5%, respectively. With this technology the sample-to-sample variations are expected to be smaller, which will help to draw a conclusion about the improvement of microlens-enhanced SiPMs with higher fill factor.

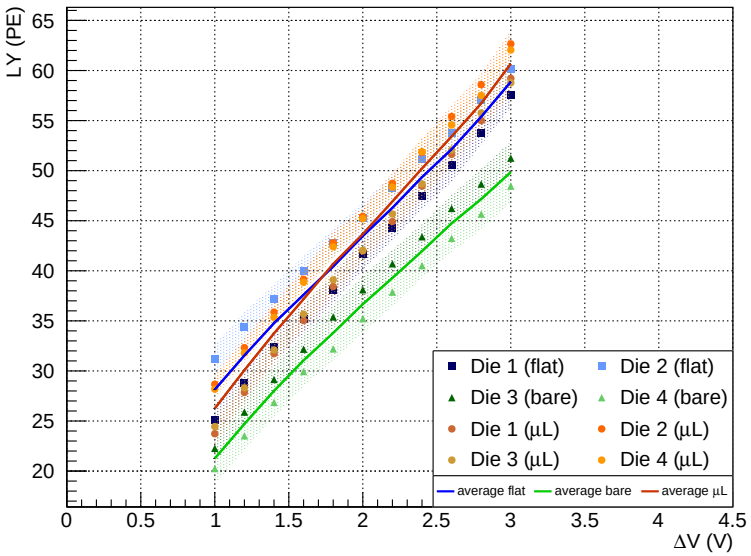

Figure 5.22 – Light yield of FBK2019-10ch with GFF = 82.4%, coupled to the fibre mat with torque of 2 cNm. Three different SiPM surfaces (microlenses, flat, bare) have been evaluated. The microlens-enhanced and flat SiPMs show clear improvement over bare samples. However, an improvement between microlens-enhanced and flat dice is not seen. The shaded regions correspond to the estimated error of each die, and are calculated according to Sec. 5.4.2.

Table 5.6 – Light yield results for SiPMs with GFF = 82.4%, coupled to the fibre mat with torque of 2 cNm.

ΔV	$LY_{\mu L}$ (PE)	LY_{flat} (PE)	LY_{bare} (PE)	$Gain_{LY,\mu L/flat}$ (%)	$Gain_{LY,\mu L/bare}$ (%)
1	26.3	28.1	21.3	-7	23
2	43.7	43.5	36.7	0	19
3	60.7	58.9	49.9	3	22

6 SciFi technology development for Upgrade II

For the LHCb Upgrade II, the instantaneous luminosity will increase by one order of magnitude, leading to more than 50 visible interactions per bunch crossing. This increase in occupancy poses a major challenge for the SciFi Tracker, as it leads to overlapping hits in space, and the separation of hits from different particles is compromised. Already in the current data taking period the reconstruction of the SciFi tracks requires intensive computing due to the crossing of the particles through the magnetic field. With the future Upgrade II, the tracking will become even more complex. One possibility to improve the track reconstruction efficiency is by adding timing information. The time information allows narrower search windows in the tracking algorithms, speeding up track finding and reducing ghost tracks. A testbeam campaign has been performed in 2019 to investigate the time resolution of a beam telescope made of short fibre mats, described in detail in Sec. 6.1.

In addition to the higher occupancy, the radiation environment will also increase approximately a factor of five in Run 5. A possibility to decrease the neutron fluence at the position of the SiPMs is to locally improve the shielding. Dedicated studies are needed to show the benefits of such a shielding and the possible options, and are not the focus of this thesis. Moreover, an improved shielding would be insufficient to keep the DCR of the SiPMs at the acceptable maximal level of 10 MHz, therefore other solutions are required to operate the tracker in this higher radiation environment compared to Run 3 and 4. As the radiation hardness of SiPMs has not improved during the past years, cryogenic cooling is proposed as the most effective way to keep the SiPMs' DCR at an acceptable level. A first measurement of the DCR of irradiated samples has led to encouraging results, and is described in Sec. 6.2. Additionally with the help of new technologies, SiPMs are now available with smaller pixel sizes and high GFF, and can reach a PDE higher than for the H2017 SiPMs. A dedicated prototyping run has been performed with FBK to produce SiPMs suitable for cryogenic operation and with a high PDE, a fast recharge time and low correlated noise due to a new trench technology [103]. This

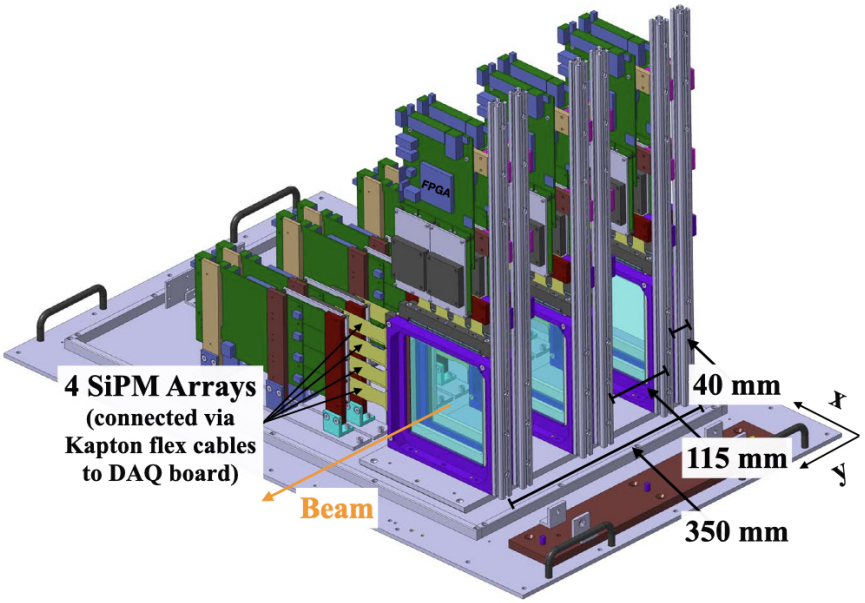

Figure 6.1 – The telescope consists of six x-y tracking stations of scintillating fibres in the vertical and horizontal directions, mounted on a common support structure.

potentially allows to operate the photodetector at higher ΔV and therefore increasing the PDE. A description of the design and preliminary results are found in Sec. 6.3.

6.1 SciFi Tracker with timing information

The SciFi technology can be improved by adding time information to the spatial information, which will reduce the number of ghost tracks and speed-up the tracking algorithm by minimising the track search window. For R&D purposes a beam telescope, shown in Fig. 6.1, has been built within the thesis. It consists of six tracking stations, where each is composed of two fibre mats oriented in x and y-direction. The 133 mm $\times$ 133 mm mat is made of seven fibre layers and is identical to the one used in Sec. 5.4. Four 128-channel SiPMs (H2017) per fibre mat are connected with Kapton flex cables to the readout boards. A light injection system, pulsed with a VCSEL diode and a light-leaking optical fibre to illuminate the fibre mat, is placed on the further end of the fibre mat. It is used for the time calibration of every SiPM channel in order to eliminate time offsets.

The signal of the SiPMs is read out by the STiC3 ASIC [140]. This chip allows the measurement of the signal time and amplitude, and uses two thresholds: the timing threshold (TTH) and the energy threshold (ETH). The timing trigger (T-Trigger) is the digital signal obtained from

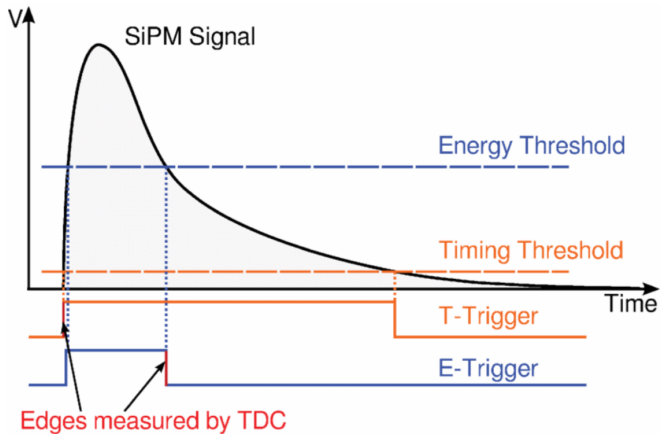

Figure 6.2 – Illustration of timing (TTH) and energy (ETH) thresholds of the STIC3 ASIC. *Picture taken from Ref. [141].*

the rising edge of the signal once it crosses TTH. The time-over-threshold (ToT), which is the difference between the rising and falling edges of the signal when crossing the ETH, gives the energy trigger (E-Trigger) (see Fig. 6.2). The final time-to-digital-converter (TDC) signal is the difference between the falling edge of the E-Trigger and the rising edge of the T-Trigger. The timestamp of a hit is given by the sum of the coarse and fine times. The TDC frequency runs on a coarse time frequency of 540 MHz, corresponding to a coarse time of 1.85 ns. A phase-locked-loop (PLL) is used to interpolate in 32 steps, and like this a fine timestamp of 57.5 ps is achieved.

Hit detection efficiency

The hit detection efficiency ε of each layer has been determined to characterise the detector. It is defined as the ratio between the number of clusters detected N at a reconstructed position over the total number of tracks N_{tot}. The reconstructed position is computed by reconstructing a track, where one layer is excluded (DUT), using only the remaining layers as reference.

The telescope has been tested during a testbeam campaign at the Test Beam Facility at DESY Hamburg (Germany) [142] in 2019 using electrons with an energy between 2 GeV and 6 GeV. The telescope has been moved to five positions (centre of the plane, referred to as Position 0, and the centre of four quadrants, starting top left and going anti-clockwise) with respect to the beam axis. The overvoltage has been varied between 3.5 V and 6.5 V.

A strict event selection is applied for the track reconstruction requiring only one cluster per layer. The spatial resolution is given by the standard deviation of the residual R, which is defined as the difference between the hit position (with a standard deviation σ_{hit}) and the

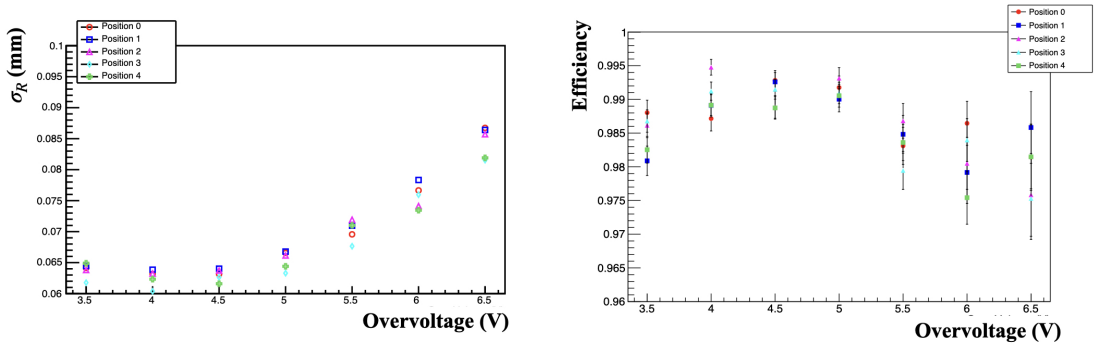

(a) (b)

Figure 6.3 – (a) Resolution and (b) efficiency of a telescope layer with data from a testbeam campaign at DESY. The efficiency is calculated for five different positions of the telescope with respect to the beam axis.

reconstructed hit position (with a standard deviation $\sigma_{\text{hit, reco}}$). Therefore the resolution is given by:

$$\sigma_R = \sqrt{\sigma^2_{\text{hit}} + \sigma^2_{\text{hit, reco}}}. \tag{6.1}$$

If several clusters are detected, the one closest to the reconstructed position is chosen. The detected hit is accepted if it is within $10\sigma_{\text{R}}$ of the reconstructed hit. An example plot of the resolution σ_{R} and the efficiency as a function of ΔV is shown in Fig. 6.3. The efficiency increases with ΔV due to the increase in PDE. At $\Delta V = 3.5\text{V}$ the efficiency is at 98.1% at Position 1 and at 98.8% for Position 0. At $\Delta V = 5\text{V}$ an efficiency of 99% is reached for all boards. The uncertainty of the efficiency is estimated with the binomial distribution $\sigma^2_{\text{N}} = N_{\text{total}} \cdot \varepsilon \cdot (1-\varepsilon)$ [143]. For the shown example, at position 0 and $\Delta V = 5\text{V}$ the number of reconstructed tracks equals 9031 tracks, which leads to an error of 1‰. At a higher ΔV the efficiency decreases due to a cut on the cluster size.

Coincidence time resolution

The coincidence time resolution (CTR) of two planes is given by the width of the distribution of the time difference between two detected hits. For a system with two identical scintillators, Eq. 2.13 can be applied, which states that CTR $\propto \sqrt{\tau_{\text{d}}}$, where τ_{d} is the scintillator decay time, and CTR $\propto \frac{1}{\sqrt{N_{\text{ph}}}}$, where N_{ph} is the number of detected direct photons. The rise time τ_{r} of the SCSF-78MJ fibre has been measured to be 75 ps, and the number of direct photons for a

short fibre module is assumed to be $N_{\text{ph}} = 25$ [144]. This yields a time resolution σ of:

$$\sigma = \frac{\text{CTR}_{\text{1st ph}}}{\sqrt{2}} = 141\,\text{ps}. \tag{6.2}$$

The time resolution is measured for single clusters per layer. The measurement requires several calibration and correction steps (described in detail in Refs. [145, 146]):

1. A board-to-board offset is applied after evaluating the hit time distribution of each layer.
2. A correction is applied to account for the light propagation time in the fibres.
3. A channel offset is extracted from the injection calibration. To further improve this offset, an iterative algorithm is applied using the cluster time information of all layers for a single track.

Applying these offsets, the best measured time resolution of the SciFi Tracker is 208 ps [145, 146].

The time resolution for the long fibre mats at LHCb is expected to be larger than the one measured with this telescope setup. The number of direct photons is much smaller for the long fibre mats (in average 6 to 10) and the propagation in the fibre will deteriorate the time resolution as the propagation path for larger angles is longer for long fibres. For LHCb, the circuit that is required to measure the time can be done with a fast clock instead of a dedicated TDC. This will the power consumption at an acceptable level. A time binning of 1/16 of the LHC bunch crossing (1.62 ns) could be used.

6.2 Cryogenic SiPM operation

With the increase of the radiation environment by a factor of five in Run 5 (2034–2039) the SiPM's DCR will drastically increase. One possible way to mitigate the ageing effect is to employ cryogenic cooling. Cooling to −40 °C is already done for the current data taking runs to keep the DCR at an acceptable level of 10 MHz per channel after the irradiation of 4.1×10^{11} 1 MeV $n_{\text{eq}}/\text{cm}^2$ expected at the end of lifetime of the detector [110]. This level of DCR could be achieved in Run 5 by cooling the detector to −80 °C. However, this type of cooling is not conventional (no vacuum insulation). Cryogenic cooling on the other hand will not only allow to have a detector that is free of noise (with an expected DCR at the level of tens of kHz per channel at 2×10^{12} 1 MeV $n_{\text{eq}}/\text{cm}^2$) but will also allow the operation at a higher ΔV and therefore a significantly higher PDE.

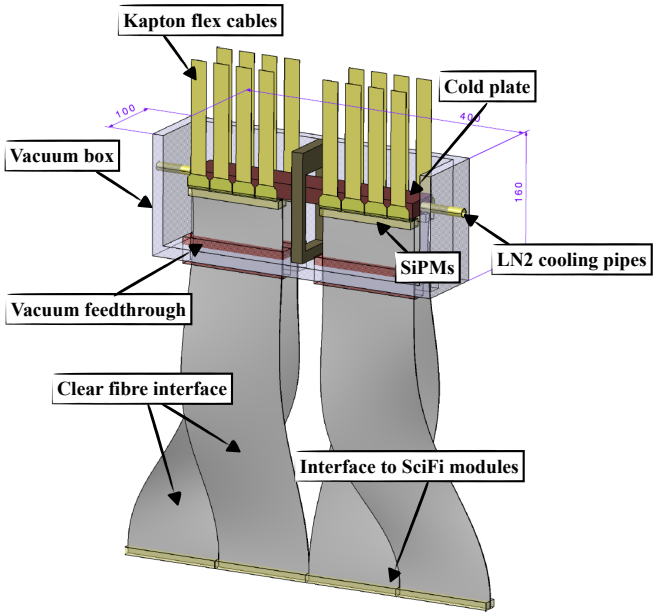

Figure 6.4 – Drawing of a possible thermal vacuum insulation envisaged for the cryogenic cooling of the SiPMs with LN2. The SiPMs will be connected via a clear fibre interface to the SciFi modules. *Picture taken from Ref. [149].*

In the past, the operation of SiPMs at cryogenic temperatures has been compromised because of the high afterpulse probability which increases with decreasing temperature due to the larger de-trap time of charge carriers. However, new afterpulse-suppressing technologies have been developed, e.g. by FBK [129] and Hamamatsu [147], keeping the afterpulse below a few percent even at liquid nitrogen (LN2) temperature (−196 °C). This technology has been mainly developed for dark matter experiments such as DUNE [148] and DarkSide-20k [100]. In these experiments, the SiPMs are fully submerged in liquid argon or xenon. In contrast, for the usage at LHCb the SiPMs would be placed in vacuum to ensure thermal insulation, as shown in Fig. 6.4. In this case, the SiPMs are in contact with a cold plate and cooled by liquid nitrogen. This configuration requires a clear fibre interface to connect the SiPMs to the fibre mats outside the vacuum box. This optical interface will cause an additional decrease in light yield of approximately 20% [53]. Another possibility is to directly couple the fibre mats to the SiPMs using a vacuum feed-through. In this case, even though a longer fibre mat (at least 15 cm) is needed, the reduction for the light yield is expected to be insignificant.

To evaluate the feasibility of cryogenic cooling at LHCb, a measurement of irradiated SiPMs has been performed in the framework of an irradiation campaign performed by FBK [150,151]. The temperature dependence of five irradiated and one non-irradiated SiPMs has been studied. The 1 mm × 1 mm SiPMs are of the NUV-HD-RH type, characterised by a low field and a fast recharge time, with a pixel size of 15 µm × 15 µm. Note that such a small pixel size has

Table 6.1 – The irradiated SiPMs with their corresponding irradiation level. The fluence expected at the end of LHCb Run 5 is approximately 4×10^{12} 1 MeV $n_{\mathrm{eq}}/\mathrm{cm}^2$.

SiPM no.	Fluence (1 MeV $n_{\mathrm{eq}}/\mathrm{cm}^2$)
1	0.0×10^{0}
2	1.3×10^{10}
3	1.2×10^{11}
4	2.3×10^{12}
5	1.5×10^{13}
6	1.1×10^{14}

a significantly lower PDE due to the small GFF, and is therefore not suitable for the LHCb SciFi Tracker. The samples have been previously irradiated at different proton fluences, as listed in Table 6.1. The fluence is generally not better known than ±50% as the proton current estimation is extremely difficult due to the production of secondaries inside the collimator volume, which influences the final output current*. As the following sections describe a comparison study of irradiated and non-irradiated samples, the absolute dose values are less important than the relative ones.

6.2.1 Fluence dependence of V_{BD} and of the activation energy

As a first step, the breakdown voltage temperature coefficient $K_{V_{\mathrm{bd}}}$ has been measured using the current-voltage characteristics at different temperatures, ranging from +60 °C to −60 °C. In Fig. 6.5, the breakdown voltage as a function of the temperature and the fluence dependence of $K_{V_{\mathrm{bd}}}$ are shown. The maximum error on the V_{BD} estimation is ±0.15 V, while the temperature was stable within ±0.5 °C. The spread of $K_{V_{\mathrm{bd}}}$ within 32.7 mV and 30.2 mV is determined by several factors such as the different thermal couplings for each sample, variable self-heating power due to DCR variation, and the V_{BD} determination uncertainty. The observed difference is therefore most likely due to sample-to-sample variation, as no trend between fluences is observed.

The activation energy (E_{a}), i.e. the energy needed for electrons to generate charge carrier pairs, has been determined by studying the reverse current at different temperatures $I(T)$, and is extracted according to the relation [150]

$$I(T) \propto \mathrm{e}^{\frac{E_{\mathrm{a}}}{k_{\mathrm{B}}T}}, \tag{6.3}$$

*The output current is given by the difference between the synchrotron proton current and the current absorbed by the collimator.

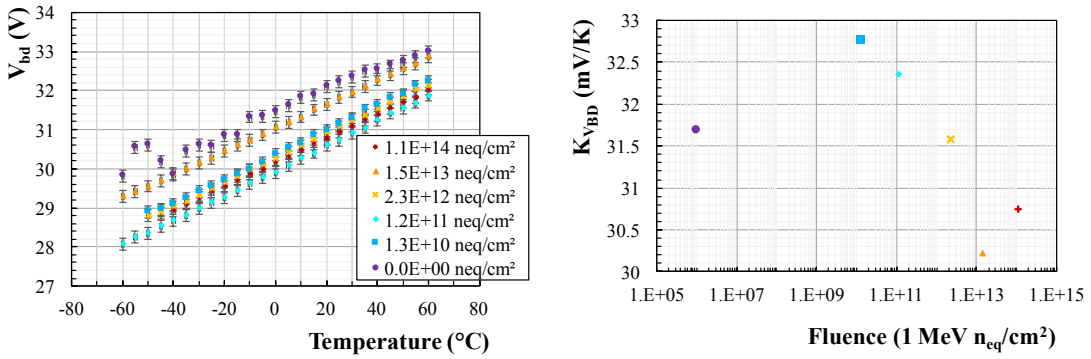

(a) (b)

Figure 6.5 – (a) The V_{BD} as a function of the temperature. (b) the fluence dependence of $K_{V_{\mathrm{bd}}}$. Note that in (b) the non-irradiated sample was drawn at a fluence of 1.E + 06 for illustration.

where k_{B} is the Boltzmann constant. The activation energy has been determined in a temperature range between –10 °C and 20 °C to ensure thermal generation of charge carriers is dominating over tunnelling. The result for three overvoltages is shown in Fig. 6.6. A clear difference between non-irradiated $E_{\mathrm{a}} = 0.63\,\mathrm{eV}$ and irradiated $E_{\mathrm{a}} = 0.37\,\mathrm{eV}$ is seen, which can be understood as a direct consequence of the domination of thermal DCR generation for irradiated SiPMs [150, 151]. Note that for Sample 6 current saturation occurred in this temperature range, and thus the E_{a} could not be determined.

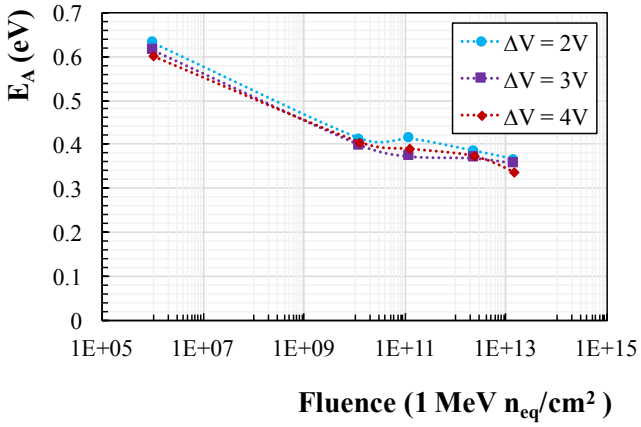

Figure 6.6 – Fluence dependence of the activation energy at three overvoltages. E_{a} reduces for irradiated samples. Note that the non-irradiated sample was drawn at a fluence of 1.E + 06 for illustration.

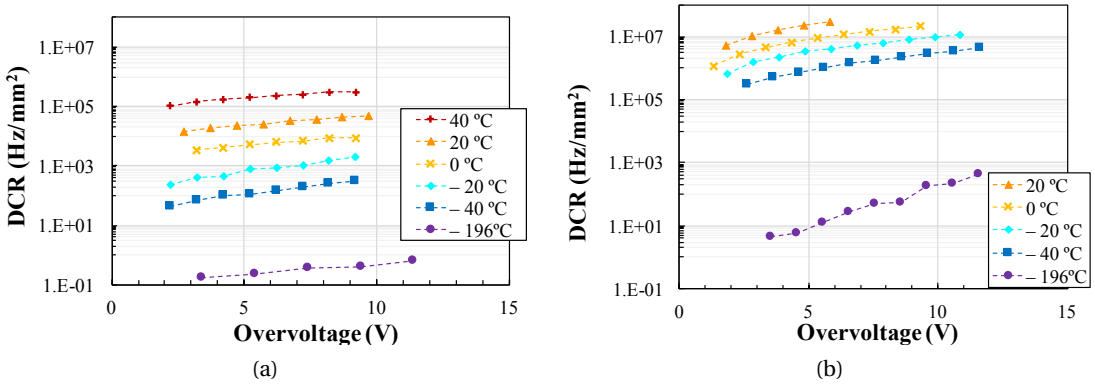

Figure 6.7 – DCR with respect to the overvoltage of (a) a non-irradiated and (b) an irradiated sample with fluence 1.2×10^{11} 1 MeV n_{eq}/cm^2. The DCR decreases drastically with the temperature. At $-196°C$ the irradiated sample shows a lower DCR than the non-irradiated one at $-40°C$.

6.2.2 Fluence and temperature dependence of DCR

The temperature dependence of the DCR at different irradiation levels is one of the most crucial aspects for the use at LHCb. The DCR has been measured in a temperature range from +40 °C to −40 °C and at LN2, using a waveform analysis (which is described in Ref. [91]). The samples have been submerged in the liquid nitrogen for the measurement at –196 °C.

The DCR plotted against the overvoltage for the non-irradiated Sample 1 and for Sample 3 is shown in Fig. 6.7. The DCR of the irradiated sample at $\Delta V = 5$ V decreases from 2×10^7 Hz/mm^2 at $T = 20$ °C to 7×10^0 Hz/mm^2 at $T = -196$ °C. It follows the same approximate decrease as mentioned in Sec. 2.4.5, and thus the DCR is reduced by a factor of two for every ten degrees of cooling.

The DCR has also been studied with respect to the fluence at overvoltages of $\Delta V = 4$ V and $\Delta V = 6$ V (see Fig. 6.8). For both lower fluence samples, the decrease in DCR amounts to approximately five orders of magnitude at both overvoltages, going from –40 °C to –196 °C. At the high fluence of 1.1×10^{14} 1 MeV n_{eq}/cm^2 the DCR is 1.14 MHz at $\Delta V = 4$ V. For $\Delta V = 6$ V the DCR is likely higher than the measured value due to saturation at rates above 10 MHz. Sample 4 is either defective, or has received a lower dose than was estimated, and is excluded from further analyses.

In Fig. 6.9, the temperature dependence of the DCR at $\Delta V = 4$ V is shown. The DCR values are obtained with the waveform analysis (represented as points) and independently from the IV-measurement (shown as dotted lines). For the latter, the DCR has been calculated using the gain of the non-irradiated sample at $\Delta V = 4$ V at 0 °C, which has been determined with the

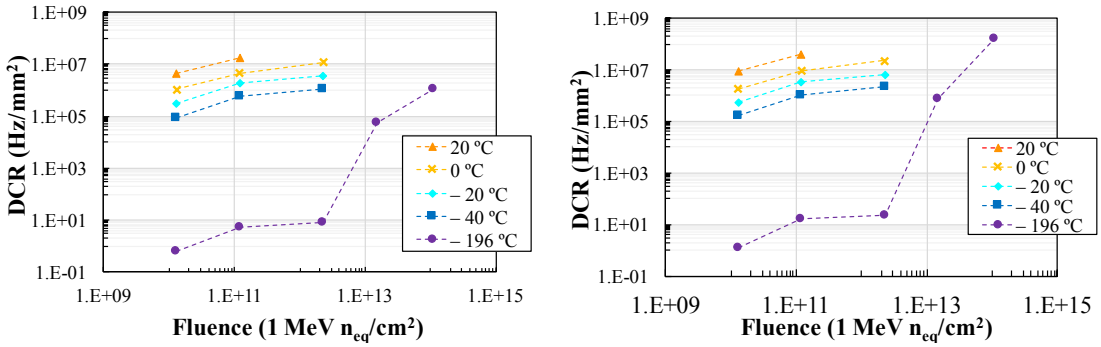

Figure 6.8 – DCR with respect to the fluence for different temperatures at an overvoltage of (a) $\Delta V = 4\,\mathrm{V}$ and (b) $\Delta V = 6\,\mathrm{V}$. Both plots show that Sample 4 is either defective or received a different dose than was estimated.

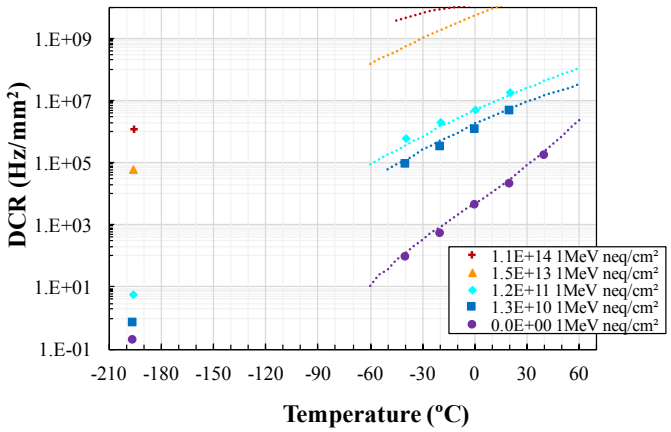

Figure 6.9 – DCR as a function of temperature at $\Delta V = 4\,\mathrm{V}$. The DCR values are obtained with two independent measurements: once with the waveform analysis (shown as points) and once via the IV-measurement (shown as dotted line). The DCR of the two samples with higher fluences is only measured at LN2 temperature.

waveform analysis. The obtained DCR values of both methods are in very good agreement. The difference in the slopes of the non-irradiated and the irradiated samples is explainable due to the change in activation energy from 0.63 eV to 0.37 eV, and the fact that for irradiated samples thermal generation of charge carriers dominates over tunnelling generation [151]. Sample 1 reaches the tunnelling plateau around −100 °C, which is a similar behaviour to the standard-field sample previously shown in Fig. 2.17, where the tunnelling plateau is reached at around −100 °C at a similar DCR level. For the irradiated samples, the linear extrapolation connects to the measured value at –196 °C . For non-irradiated samples, tunnelling is expected to dominate at LN2 temperatures.

Table 6.2 – Comparison of the characteristics and the measured properties between irradiated H2017 and FBK-NUV-HD-RH detectors.

Property	H2017 (Hamamatsu)	NUV-HD-RH (FBK)
area	$0.4\,\mathrm{mm}^2$	$1\,\mathrm{mm}^2$
pixel size	$(60\,\mu\mathrm{m})^2$	$(15\,\mu\mathrm{m})^2$
temperature	$-40\,^\circ\mathrm{C}$	$-40\,^\circ\mathrm{C}$
ΔV	3.5 V	3.5 V
fluence	6×10^{11} 1 MeV $n_{\mathrm{eq}}/\mathrm{cm}^2$	1.3×10^{11} 1 MeV $n_{\mathrm{eq}}/\mathrm{cm}^2$
measured DCR	14 MHz	500 kHz
scaled DCR		2 MHz

Prospects at LHCb

The characteristics of H2017 and FBK-NUV-HD-RH SiPMs are given in Table 6.2. Some scaling of the detector channel area, the geometrical fill factor (GFF) and the fluence is necessary to compare the two technologies for radiation hardness. The scaled DCR of the FBK-NUV-HD-RH sample is expected to be in the order of 2 MHz, leading to the conclusion that the technology of FBK-NUV-HD-RH results in a seven times lower DCR compared to H2017. Note that the large difference in pixel size (GFF) favours the FBK technology, but the results are still very encouraging.

The obtained results support the prospects of implementing cryogenically cooled SiPMs in a future high-radiation run at LHCb. The implementation of cryogenic cooling at LHCb with an additional clear fibre interface will reduce the light yield by 20%, and therefore the usage of microlens-enhanced SiPMs to compensate this loss is strongly encouraged.

6.2.3 Fluence and temperature dependence of gain and correlated noise

The other important properties to study are the gain and the correlated noise of the detectors. From the measurements of irradiated samples described in Refs. [150, 151], these properties are not affected by radiation up to a level of 10^{13} 1 MeV $n_{\mathrm{eq}}/\mathrm{cm}^2$.

For the gain this observation is confirmed in the temperature range from $+40\,^\circ\mathrm{C}$ to $-40\,^\circ\mathrm{C}$ (Fig. 6.10a). The large spread at LN2 temperatures is partially due to the increase of R_{Q} and a resulting change of the pulse shape. In addition, an instability of the amplifier has been observed, causing oscillations. This also occurred for the measurements of the crosstalk and afterpulse, and thus these data points have been excluded. Therefore, only the non-irradiated and the two low-fluence samples have been characterised in terms of correlated noise. The

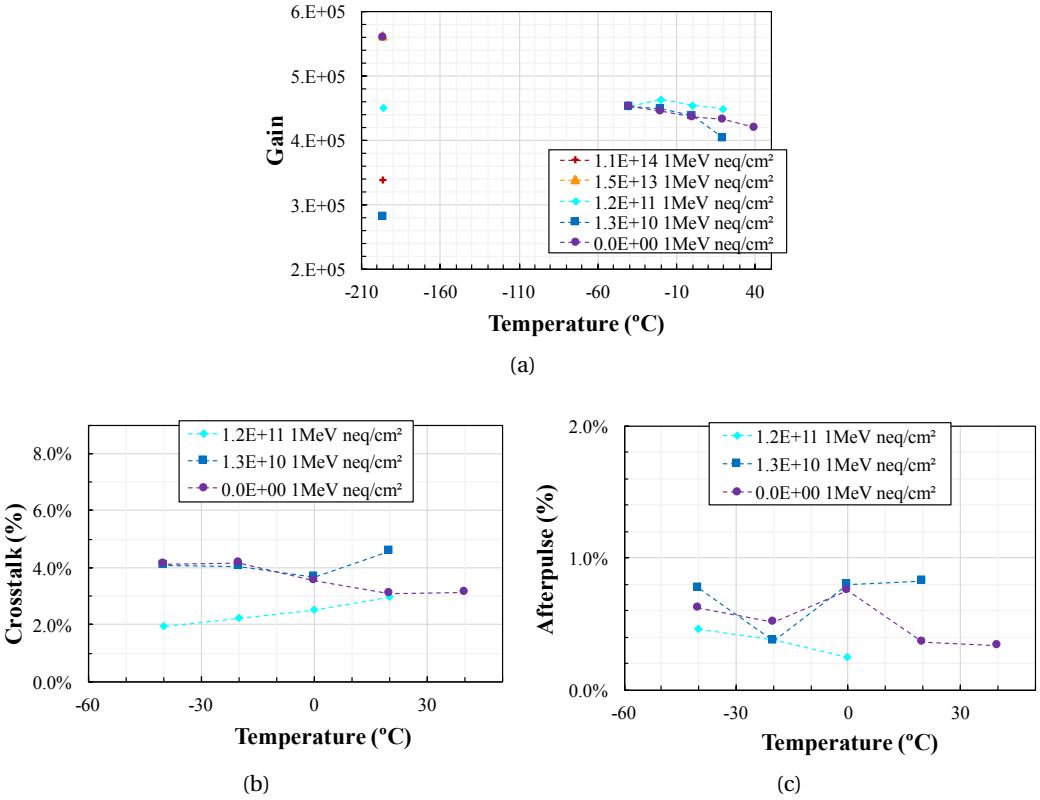

Figure 6.10 – (a) The (a) SiPM gain, (b) total crosstalk and (c) afterpulse probability as a function of the temperature for different fluences at an overvoltage $\Delta V = 4$V. Gain and crosstalk remain constant with temperature and fluence.

crosstalk, shown in Fig. 6.10b, remains unchanged. Note that the crosstalk for these samples is low due to the small pixel size (thus the small gain), and the systematic error is in the order of the observed variation. The afterpulse remains stable within the temperatures from +40 °C to −40 °C as shown in Fig. 6.10c. As these samples have been developed for cryogenic applications, the afterpulse probability should show only a minor increase even at −196 °C.

6.3 FBK2022 customised SiPM arrays

For Upgrade II the project requires a close collaboration with SiPM manufacturers to work towards a suitable SiPM complying to the requirements, i.e. achieving a high single hit detection efficiency (therefore having a high signal-to-noise ratio and small dead time of the SiPMs), and the operation at the expected higher fluence levels. All these improvements require a combination of several SiPM technologies. The SiPM technologies from FBK has greatly advanced since the production of H2017 SiPMs for the LHCb SciFi Tracker by Hamamatsu.

The improvements include:

- a high GFF even with small pixel sizes, improving in turn the PDE ,
- thin insulation trench technology with efficient crosstalk suppression ,
- increased stable operation range ,
- cryogenic operation with low afterpulse, recovery time and DCR ,
- and low V_{BD} spread .

All these improvements comply with the requirements for a future SiPM used in the LHCb SciFi Tracker. Therefore, a dedicated prototype series, referred to as FBK2022, has been designed based on the results obtained during this thesis and has been produced by FBK. The new prototypes take advantage of the aforementioned improvements in technologies, combining a high PDE with cryogenic applications (afterpulse suppression) and the novel metal-in-trench technology [103] for low correlated noise.

One single die is a 64-channel device and has a die size of 16.2 mm × 3.2 mm and a channel size of 1.66 mm × 0.25 mm channels. The design foresees two pixel sizes of 31.3 µm × 31.3 µm (referred to as 31 µm) and 41.7 µm × 41.7 µm (referred to as 42 µm). The detectors are equipped with alignment markers dedicated for microlens implementation to support precise microlens-to-pixel alignment. The large die height of 3.2 mm has been designed such that potential spacers can be implemented, and to have enough room to accommodate the bond wires when the SiPMs are coupled to a fibre mat, as previously shown in Fig. 5.6b. An additional die has been designed with a channel surface of 16.2 mm × 3.2 mm and 15.65 µm × 15.65 µm (referred to as 16 µm) pixels, and is dedicated to readout thicker SciFi mats.

A full silicon wafer, depicted in Fig. 6.11a, is split into 120 so-called shots with one 16 µm, two 31 µm and one 42 µm arrays, plus additional 1 mm × 1 mm test structures. A close-up of a partial shot is shown in Fig. 6.11b. Wafer splitting has been used to vary the electric field and the implant dose.

A quench resistor of $R_Q = 500\,k\Omega$ is implemented in all designs. The second version of the 31 µm pixels has an additional capacitance in form of a metal mask (in parallel to R_Q) implemented, which enhances the fast peak of the cell recharge amplitude. The mask is also implemented for the 42 µm pixel arrays.

Preliminary results ot the DCR, PDE, crosstalk and recovery time of one channel for all pixel layouts are shown in Fig. 6.12. The DCR stays within the expected range, and for the 16 µm pixel

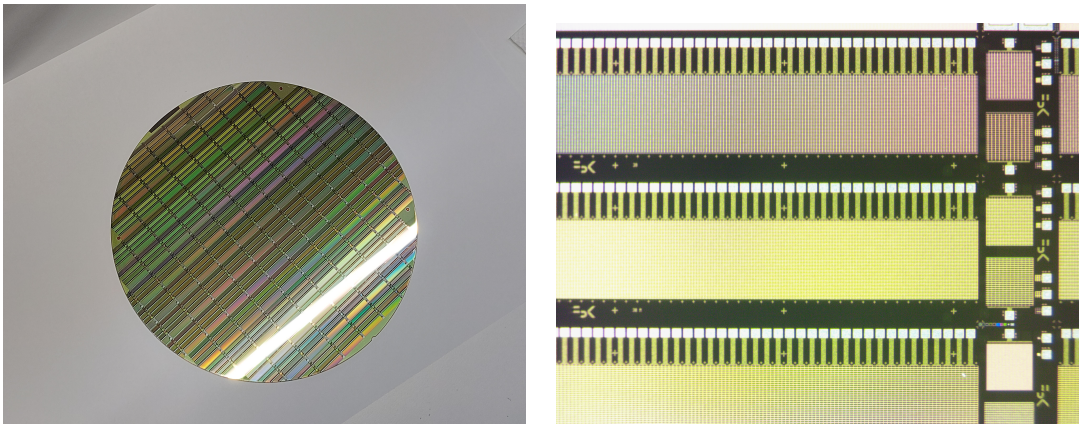

(a) (b)

Figure 6.11 – (a) View of the 11 inch wafer with 120 shots. (b) A shot consisting of four arrays and additional test structures. The arrays' layouts have a square pixel size of 15.65 µm, 31.3 µm, 31.3 µm (with mask) and 41.7 µm (top to bottom). *Pictures taken from Ref. [152].*

is similar to the DCR measured for Sample 1 in Fig. 6.7. The PDE reaches very high values of up to 60% for 42 µm pixels at the peak wavelength (420 nm) at high overvoltage $\Delta V = 10\,\mathrm{V}$. At the same conditions, the crosstalk probability stays below 2.5% for 42 µm pixels. The recovery time is approximately $\tau_{\mathrm{rec}} = \{60\,\mathrm{ns}, 35\,\mathrm{ns}, 30\,\mathrm{ns}, 10\,\mathrm{ns}\}$ for {42 µm, 31 µm (mask), 31 µm, 16 µm} pixels. From these measurements it seems that the pixel masking have a higher recovery time than expected, and further tests need to be conducted for better understanding. Note that the recovery time is expected to increase due to an increase in R_{Q} of 40% going from +20 °C to –40 °C [153].

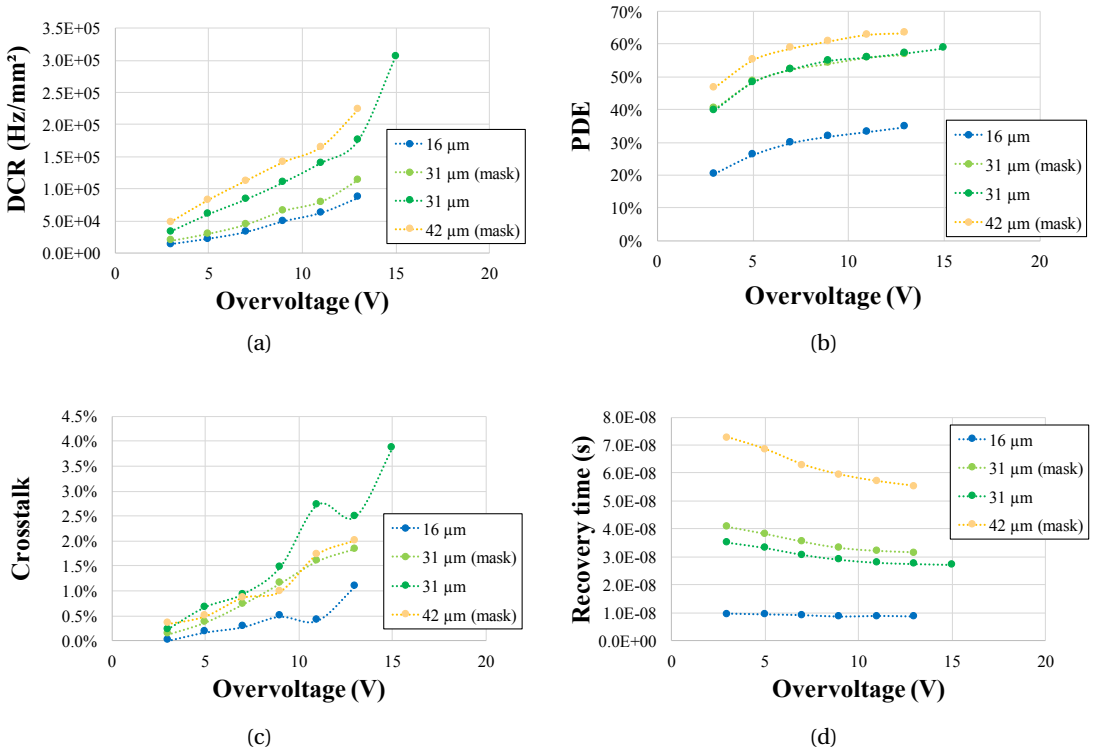

Figure 6.12 – First characterisation results of 1 mm × 1 mm test structures of (a) DCR, (b) PDE, (c) crosstalk and (d) recovery time. The samples show excellent characteristics: high PDE, remarkably low crosstalk probabilities at very high ΔV, and a high operation range. The recovery time of unmasked samples is as expected, whereas for the masked SiPM the recovery time is higher than expected. *Pictures replotted from Ref. [153].*

Conclusion and outlook

The SciFi Tracker technology, consisting of scintillating fibres and a SiPM readout, has been studied in detail during this PhD work, with a focus on improving the detection efficiency of the photodetectors. Microlenses have been successfully implemented in a checkerboard structure and evaluated on 40 µm × 40 µm pixel devices (as described in Chapter 5). For SiPMs with a geometrical fill factor (GFF) of 50.0% a light yield improvement of 32% is achieved at $\Delta V = 1\,\mathrm{V}$ and of 19% at a higher $\Delta V = 4\,\mathrm{V}$. This confirms that microlenses can be used to avoid the low-field pixel region, present at low overvoltage. With a higher fill factor of 82.4% no improvement was seen. The GFF of this detector has been pushed to the limit and cannot be operated in a large operation range thus reducing the PDE. A next step is to produce a new iteration on customised, dedicated silicon. The effect of a better microlens-to-pixel alignment and the exit angle distribution of long fibre mats has to be studied on a larger number of samples to compensate sample-to-sample variations.

The developed microlens simulation described in Chapter 4 has been validated by a commercial ray-tracing tool at CSEM, as well as with the results of the GFF = 50.0% samples. For these, the simulation predicted an improvement of up to 56%. The difference between the simulated 56% and the measured 32% can be due to the uncertainty of the exit angle distribution, the difference between long and short fibres, the fibre mat surface quality, the misalignment of microlenses to the pixel structure, the geometry uncertainty of the low-field region, and sample-to-sample variations of the SiPMs. For the samples with GFF = 82.4% no improvement is seen. The possible reasons are the larger sample-to-sample variations, the lens-to-pixel misalignment, which becomes more important for higher fill factors, and the exit angle distribution.

In view of Upgrade II, several objectives were studied. The measurements with irradiated SiPMs optimised for cryogenic applications from FBK confirm a drastic reduction in DCR at liquid nitrogen (LN2) temperatures. Compared to the measured DCR at an operation temperature of –40 °C the DCR at LN2 is reduced by a factor of up to five orders of magnitude. Furthermore, the gain, crosstalk, afterpulse and recovery time remain unchanged up to Upgrade II radiation levels.

Customised SiPM arrays (FBK2022, refer to Sec. 6.3) based on the most advanced technology were produced and the first results presented. These SiPMs are available in two pixel sizes of 31.3 µm × 31.3 µm (GFF = 75%) and 41.7 µm × 41.7 µm (GFF = 81.5%), such that a high PDE can be reached while keeping the correlated noise, recovery time, gain and DCR at a minimum. Indeed, at $\Delta V = 10$ V the samples with 42 µm square pixels show extraordinary low crosstalk and high PDE of respectively 2.5% and 60%. For Upgrade II this performance is required to mitigate a loss in light yield of the fibres cause by the higher radiation environment. Bigger pixel sizes lead to self-heating due to larger gain, have a longer recovery time, larger crosstalk and only a small improvement in PDE. Smaller pixels are expected to perform better after radiation exposure, but have not been pursued because of their lower PDE.

Finally, a telescope with short fibre mats with an active area of 133 mm × 133 mm was built to evaluate the time resolution in a testbeam campaign using a commercial readout ASIC (STiC3). The achieved time resolution of one layer is 210 ps.

For Upgrade II, an encoded timestamp in addition to the spatial information of a hit is foreseen to minimise the search window of the tracking algorithm. Incorporating timing in LHCb SciFi requires further studies on long fibre modules and the development of a suitable front-end chip for low-light applications. For long modules a deterioration of the time resolution due to the longer travel path (diffusion) and the lower number of direct photons is expected, with an expected value between 1 ns and 2 ns.

In addition to timing studies, dedicated irradiation studies using the newly developed SiPM arrays (FBK2022) are foreseen. The measurements will be performed in a large temperature range, covering also temperatures between −40 °C and LN2, and at several fluences up to 10^{13} 1 MeV $n_{\mathrm{eq}}/\mathrm{cm}^2$ to validate the results from the initial study described in Sec. 6.2. These measurements will provide precise information on the dominating DCR contributions for irradiated and non-irradiated samples. Conclusions on the best doping and electric field profile for the radiation environment at LHCb are expected from the results, such that a possible dedicated production for Upgrade II can be launched.

Additionally, another iteration of microlens-enhanced SiPMs will be started in the near future to have a larger number of devices and achieve better statistics. This will allow to evaluate the effects of microlenses on pixels with different fill factors, which has not been possible due to the observed high sample-to-sample variation. The expected gain in light yield of microlenses-enhanced over flat coated SiPMs amounts to approximately 15%. For these samples an additional anti-reflective coating on top of the microlens material is planned to reduce Fresnel reflections on the air-polymer interface. The light yield comparison will be examined on polished, long fibre mats to study the effect of the exit angle distribution. A quality assurance of the optical surface of the fibre mat needs to be performed.

A First measurement of the scintillating fibre exit angle distribution

The exit angle of the scintillating fibre SCSF-78MJ was first measured in 2019 [122]. The measurement was performed using the same measurement setup as described in Sec. 4.2.2 without an additional aperture. The fibre was excited using a UV-LED at a distance of 200 cm from the fibre end. The exit angle distribution shown in Fig. A.1 has been used to determine the parameters for the first microlens implementation. The linear increase and sharp drop at 45° is the result of a saturation of the camera. Therefore, this exit angle distribution was remeasured during the course of this thesis (see Sec. 4.2.2). For a future microlens implementation, the new result will be used to determine the lens parameters.

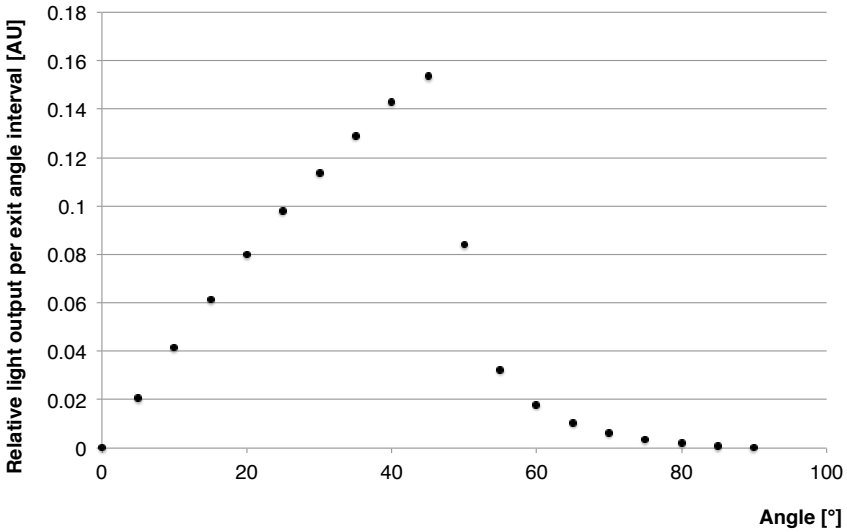

Figure A.1 – The exit angle distribution of the scintillating fibre SCSF-78MJ measured in 2019. The mean value is 34.8°. *Picture taken from Ref. [122].*

Bibliography

[1] R. Brun and F. Rademakers, *ROOT—An object oriented data analysis framework*, Nucl. Instrum. Methods Phys. Res. A **389** (1997) 81.

[2] Fondazione Bruno Kessler - Sensors and Devices, Trento, Italy. https://sd.fbk.eu/en/.

[3] Hamamatsu Photonics K. K. , Japan. https://www.hamamatsu.com/jp/en.html.

[4] E. Lopienska, *The CERN accelerator complex layout in 2022, General Photo*, https://cds.cern.ch/record/2800984, 2022. last accessed: 2023-02-04.

[5] ATLAS collaboration, *Letter of intent for a general purpose p p experiment at the Large Hadron Collider at CERN*, CERN-LHCC-92-004, CERN, Geneva, 1992.

[6] CMS collaboration, M. Della Negra *et al.*, *CMS: letter of intent by the CMS Collaboration for a general purpose detector at LHC*, CERN-LHCC-92-003, CERN, Geneva, 1992.

[7] ALICE collaboration, N. Antoniou *et al.*, *Letter of intent for A Large Ion Collider Experiment*, CERN-LHCC-093-16, CERN, Geneva, 1993.

[8] LHCb collaboration, *Letter of intent*, CERN-LHCC-95-5. LHCC-I-8, CERN, Geneva, 1995.

[9] TOTEM collaboration, W. Kienzle *et al.*, *Total cross section: elastic scattering and diffraction dissociation at the LHC*, CERN-LHCC-97-049, CERN, Geneva, 1997.

[10] LHCf collaboration, D. A. Faus *et al.*, *Measurement of photons and neutral pions in the very forward region of the LHC*, CERN-LHCC-2003-057, CERN, Geneva, 2003.

[11] V. Mitsou (on behalf of the MoEDAL Collaboration), *MoEDAL, MAPP and future endeavours*, PoS **DISCRETE2020-2021** (2022) 017.

[12] FASER collaboration, A. Ariga *et al.*, *Letter of intent for FASER: ForwArd Search ExpeRiment at the LHC*, CERN-LHCC-2018-030, CERN, Geneva, 2018.

[13] SND@LHC collaboration, *Scattering and Neutrino Detector at the LHC*, CERN-LHCC-2020-013, CERN, Geneva, 2020.

[14] S. Dris, *Performance of the CMS tracker optical links and future upgrade using bandwidth efficient digital modulation*, PhD thesis, Imperial College, London, 2010, arXiv:1004.5574, CERN-THESIS-2007-015.

[15] LHCb collaboration, R. Aaij *et al.*, *Observation of $J/\psi p$ resonances consistent with pentaquark states in $\Lambda_b^0 \to J/\psi p K^-$ decays*, Phys. Rev. Lett. **115** (2015) 072001, arXiv:1507.03414.

[16] LHCb collaboration, R. Aaij *et al.*, *Measurement of the CKM angle γ with $B^\mp \to D[K^\pm\pi^\mp\pi^\mp\pi^\pm]h^\mp$ decays using a binned phase-space approach*, arXiv:2209.03692, submitted to JHEP.

[17] ATLAS collaboration, G. Aad *et al.*, *Observation of a new particle in the search for the Standard Model Higgs boson with the ATLAS detector at the LHC*, Phys. Lett. B **716** (2012) 1, arXiv:1207.7214.

[18] CMS collaboration, S. Chatrchyan *et al.*, *Observation of a new boson at a mass of 125 GeV with the CMS experiment at the LHC*, Phys. Lett. B **716** (2012) 30, arXiv:1207.7235.

[19] O. M. Gomez, *Five mysteries the Standard Model can't explain*, https://www.symmetrymagazine.org/article/five-mysteries-the-standard-model-cant-explain, 2018. last accessed: 2023-02-15.

[20] J. S. Farnes, *A unifying theory of dark energy and dark matter: Negative masses and matter creation within a modified ΛCDM framework*, Astronomy & Astrophysics **620** (2018) A92.

[21] G. Bellini, L. Ludhova, G. Ranucci, and F. Villante, *Neutrino oscillations*, Advances in High Energy Physics **2014** (2014) 1.

[22] FASER collaboration, H. Abreu *et al.*, *Technical Proposal: FASERnu*, CERN-LHCC-2019-017, CERN, Geneva, 2019.

[23] A. Achterberg *et al.*, *First year performance of the IceCube neutrino telescope*, Astroparticle Physics **26** (2006) 155, arXiv:astro-ph/0604450.

[24] S. Fukuda *et al.*, *The Super-Kamiokande detector*, Nucl. Instrum. Methods Phys. Res. A **501** (2003) 418.

[25] A. Einstein, *The field equations of gravitation*, Sitzungsber. Preuss. Akad. Wiss. Berlin (Math. Phys.) **1915** (1915) 844.

[26] L. Canetti, M. Drewes, and M. Shaposhnikov, *Matter and antimatter in the universe*, New Journal of Physics **14** (2012) 095012.

[27] A. A. Alves Jr *et al.*, *The LHCb detector at the LHC*, Journal of instrumentation **3** (2008) S08005.

[28] LHCb collaboration, *LHCb Tracker Upgrade Technical Design Report*, CERN-LHCC-2014-001, CERN, Geneva, 2014.

[29] LHCb collaboration, *Framework TDR for the LHCb Upgrade: Technical Design Report*, CERN-LHCC-2012-007, CERN, Geneva, 2012.

[30] LHCb collaboration, C. Elsässer, *$\overline{b}b$ production angle plots*, https://lhcb.web.cern.ch/lhcb/speakersbureau/html/bb_ProductionAngles.html. last accessed: 2023-02-02.

[31] M. Palutan (on behalf of the LHCb collaboration), *LHCb Upgrade II Framework TDR*, https://indico.cern.ch/event/1160084/contributions/4889591/attachments/2464173/4227713/LHCbweek_upgrade2_Junel2022.pdf, 2022. last accessed: 2022-10-04.

[32] R. Aaij *et al.*, *A comparison of CPU and GPU implementations for the LHCb experiment Run 3 trigger*, Comput. Softw. Big Sci. **6** (2022) 1, arXiv:2105.04031.

[33] LHCb collaboration, *LHCb VELO Upgrade Technical Design Report*, CERN-LHCC-2013-021, CERN, Geneva, 2013.

[34] LHCb collaboration, *LHCb PID Upgrade Technical Design Report*, CERN-LHCC-2013-022, CERN, Geneva, 2013.

[35] LHCb collaboration, *LHCb PLUME: Probe for Luminosity Measurement*, CERN-LHCC-2021-002, CERN, Geneva, 2021.

[36] LHCb collaboration, *LHCb Trigger and Online Upgrade Technical Design Report*, CERN-LHCC-2014-016, CERN, Geneva, 2014.

[37] D. H. C. Pérez, N. Neufeld, and A. R. Núñez, *Search by triplet: An efficient local track reconstruction algorithm for parallel architectures*, Journal of Computational Science **54** (2021) 101422.

[38] A. Lechner, *Cern: Particle interactions with matter*, CERN Yellow Rep. School Proc. **5** (2018) 47.

[39] M. Huhtinen, *Simulation of non-ionising energy loss and defect formation in silicon*, Nucl. Instrum. Methods Phys. Res. A **491** (2002) 194.

[40] E. Garutti and Y. Musienko, *Radiation damage of SiPMs*, Nucl. Instrum. Methods Phys. Res. A **926** (2019) 69, arXiv:1809.06361.

[41] I. Dawson, F. Faccio, M. Moll, and A. Weidberg, *Overview of radiation effects on detector systems*, CERN Yellow Reports: Monographs **1** (2021) 3.

[42] M. Moll, *The NIEL project*, https://indico.cern.ch/event/979793/contributions/4127788/attachments/2156198/3636946/NIEL%20project_201204v1.pdf, 2020. last accessed: 2023-02-15.

[43] G. Lindström, *Radiation damage in silicon detectors*, Nucl. Instrum. Methods Phys. Res. A **512** (2003) 30.

[44] G. P. Summers *et al.*, *Damage correlations in semiconductors exposed to gamma, electron and proton radiations*, IEEE Transactions on Nuclear Science **40** (1993) 1372.

[45] M. Huhtinen and P. Aarnio, *Pion induced displacement damage in silicon devices*, Nucl. Instrum. Methods Phys. Res. A **335** (1993) 580.

[46] P. J. Griffin, J. G. Kelly, T. F. Luera, and J. VanDenburg, *SNL RML recommended dosimetry cross section compendium*, SAND-92-0094, Sandia National Labs., Albuquerque, NM (United States), 1993.

[47] A. Y. Konobeyev, Y. A. Korovin, and V. Sosnin, *Neutron displacement cross-sections for structural materials below 800 MeV*, Journal of nuclear materials **186** (1992) 117.

[48] A. Ulyanov *et al.*, *Radiation damage study of SensL J-series silicon photomultipliers using 101.4 MeV protons*, Nucl. Instrum. Methods Phys. Res. A **976** (2020) 164203, arXiv:2007.10919.

[49] G. Battistoni *et al.*, *Overview of the FLUKA code*, Annals of Nuclear Energy **82** (2015) 10.

[50] C. Ahdida *et al.*, *New capabilities of the FLUKA multi-purpose code*, Front. Phys. **9** (2022) 788253.

[51] M. Calvo Gomez *et al.*, *Studies of a neutron shielding for the upgraded LHCb detector*, CERN-LHCb-INT-2017-014, CERN, Geneva, 2017.

[52] M. Karacson, *Evaluation of the radiation environment of the LHCb experiment*, PhD thesis, Technische Universität Wien (Atominstitut), 2016, CERN-THESIS-2016-246.

[53] LHCb collaboration, *Framework TDR for the LHCb Upgrade II — Opportunities in flavour physics, and beyond, in the HL-LHC era*, CERN-LHCC-2021-012, CERN, Geneva, 2021.

[54] H. Augustin *et al.*, *MuPix10: first results from the final design*, Proceedings of the 29th International Workshop on Vertex Detectors (VERTEX2020) (2021) 010012, arXiv:2012.05868.

[55] M. Prathapan *et al.*, *ATLASpix3: A high voltage CMOS sensor chip designed for ATLAS Inner Tracker*, PoS (TWEPP2019) **390** (2020) 010.

[56] D. Murray, *Developing silicon pixel detectors for LHCb: constructing the VELO Upgrade and developing a MAPS-based tracking detector*, PhD thesis, Manchester U., 2022, CERN-THESIS-2021-325.

[57] P. Križan and S. Korpar, *Photodetectors in particle physics experiments*, Annual Review of Nuclear and Particle Science **63** (2013) 329.

[58] W. Zheng, L. Jia, and F. Huang, *Vacuum-ultraviolet photon detections*, iScience **23** (2020) 101145.

[59] F. Acerbi *et al.*, *Silicon photomultipliers and single-photon avalanche diodes with enhanced NIR detection efficiency at FBK*, Nucl. Instrum. Methods Phys. Res. A **912** (2018) 309.

[60] Y. Musienko, *Photodetectors*, https://indico.cern.ch/event/111710/attachments/37206/53770/Musienko-for-EDIT-2010-Photodetectors.pdf, 2010. last accessed: 2023-04-14.

[61] R. Paschotta (for RP Photonics), *Photoelectric effect*, https://www.rp-photonics.com/photoelectric_effect.html. last accessed: 2023-02-15.

[62] A. Buzulutskov, *Gaseous photodetectors with solid photocathodes*, Physics of Particles and Nuclei **39** (2008) 424.

[63] J. L. Gauci *et al.*, *Preparing the ALICE-HMPID RICH for the high-luminosity LHC period 2021–2023*, Nucl. Instrum. Methods Phys. Res. A **952** (2020) 161798.

[64] N. Dinu *et al.*, *Photo-detection: principles, performance and limitations*, https://indico.cern.ch/event/124395/contributions/94140/attachments/74612/107017/Photodetection_Basics.pdf, 2011. last accessed: 2022-02-05.

[65] K. Arisaka, *New trends in vacuum-based photon detectors*, Nucl. Instrum. Methods Phys. Res. A **442** (2000) 80.

[66] Hamamatsu Photonics K. K. , *Photomultiplier Tubes - Basics and Applications, fourth edition*, https://www.hamamatsu.com/content/dam/hamamatsu-photonics/sites/documents/99_SALES_LIBRARY/etd/PMT_handbook_v4E.pdf, 2017. last accessed: 2022-11-05.

[67] Hamamatsu Photonics K. K. , *Photomultiplier Tubes and Assemblies for scintillation counting and high energy physics*, https://www.hamamatsu.com/content/dam/

hamamatsu-photonics/sites/documents/99_SALES_LIBRARY/etd/High_energy_PMT_TPMZ0003E.pdf, 2017. last accessed: 2022-11-05.

[68] P. Wagner, G. P. Reischl, and G. Steiner, *Einführung in die Physik*, Facultas. wuv, 2014.

[69] E. Rosencher and B. Vinter, *Optoelectronics*, Cambridge University Press, 2002.

[70] Y. Peter and M. Cardona, *Fundamentals of semiconductors: physics and materials properties*, Springer Science & Business Media, 2010.

[71] S. M. Sze, Y. Li, and K. K. Ng, *Physics of semiconductor devices*, John wiley & sons, 2021.

[72] W. Boeglin, *Energy band diagram for a p-n junction*, https://wanda.fiu.edu/boeglinw/courses/Modern_lab_manual3/pn_junction.html, 2022. last accessed: 2023-02-05.

[73] C. Honsberg and S. Bowden, *Photovoltaics education website: "P-N junction diodes"*, https://www.pveducation.org, 2019. last accessed: 2023-05-02.

[74] J. Stiles, *The p-n junction diode (open circuit)*, http://www.ittc.ku.edu/~jstiles/312/handouts/The%20pn%20Junction%20Diode.pdf. last accessed: 2023-04-14.

[75] G. Collazuol, *The SiPM physics and technology - a review*, https://indico.cern.ch/event/164917/contributions/1417121/attachments/198512/278663/PhotoDet12_-_collazuol_-_v3.pdf, 2012. last accessed: 2023-01-22.

[76] S. Gundacker and A. Heering, *The silicon photomultiplier: fundamentals and applications of a modern solid-state photon detector*, Phys. Med. Biol. **65** (2020) 17TR01.

[77] PhysicsOpenLab, *Si-pin photodiode β detector*, https://physicsopenlab.org/2017/04/28/si-pin-photodiode-%ce%b2-detector/, 2017. last accessed: 2023-02-05.

[78] A. Kuzmin, *Electromagnetic calorimeter of Belle II*, Nucl. Instrum. Methods Phys. Res. A **958** (2020) 162235.

[79] C. Cooke, *Upgrade of the CMS barrel electromagnetic calorimeter for the high luminosity LHC*, Instruments **6** (2022) 29.

[80] Hamamatsu Photonics K. K. , *Si APD*, https://www.hamamatsu.com/content/dam/hamamatsu-photonics/sites/documents/99_SALES_LIBRARY/ssd/si-apd_kapd9007e.pdf, 2021. last accessed: 2023-02-05.

[81] F. Acerbi and S. Gundacker, *Understanding and simulating SiPMs*, Nucl. Instrum. Methods Phys. Res. A **926** (2019) 16.

[82] P. Lecoq and S. Gundacker, *SiPM applications in positron emission tomography: toward ultimate PET time-of-flight resolution*, Euro. Phys. J. Plus **136** (2021) 292.

[83] F. Zappa, S. Tisa, A. Tosi, and S. Cova, *Principles and features of single-photon avalanche diode arrays*, Sensors and Actuators A **140** (2007) 103.

[84] S. Cova *et al.*, *Avalanche photodiodes and quenching circuits for single-photon detection*, Applied optics **35** (1996) 1956.

[85] O. G. Girard, *Development of the scintillating fibre tracker technology for the LHCb upgrade and the LHC beam profile monitoring system*, PhD thesis, EPFL, 2018, CERN-THESIS-2018-232.

[86] D. Renker and E. Lorenz, *Advances in solid state photon detectors*, Journal of Instrumentation **4** (2009) P04004.

[87] R. N. Hall, *Electron-hole recombination in germanium*, Phys. Rev. **87** (1952) 387.

[88] A. Gola *et al.*, *NUV-sensitive silicon photomultiplier technologies developed at Fondazione Bruno Kessler*, Sensors **19** (2019) 308.

[89] S. Merzi, *Novel applications of FBK SiPMs in the detection of low energy ionizing radiation*, PhD thesis, University of Trento, 2020, DOI: 10.15168/11572_276309.

[90] N. Akil *et al.*, *A multimechanism model for photon generation by silicon junctions in avalanche breakdown*, IEEE Transactions on Electron Devices **46** (1999) 1022.

[91] C. Piemonte *et al.*, *Development of an automatic procedure for the characterization of silicon photomultipliers*, in *2012 IEEE Nuclear Science Symposium and Medical Imaging Conference Record (NSS/MIC)*, 428–432, IEEE, 2012.

[92] N. Kratochwil, S. Gundacker, and E. Auffray, *A roadmap for sole Cherenkov radiators with SiPMs in TOF-PET*, Phys. Med. Biol. **66** (2021) 195001.

[93] F. Villa, F. Severini, F. Madonini, and F. Zappa, *SPADs and SiPMs arrays for long-range high-speed light detection and ranging (LiDAR)*, Sensors **21** (2021) 3839.

[94] R. Yang *et al.*, *A method of range walk error correction in SiPM LiDAR with photon threshold detection*, Photonics **9** (2022) 24.

[95] S. Gundacker *et al.*, *Experimental time resolution limits of modern SiPMs and TOF-PET detectors exploring different scintillators and Cherenkov emission*, Phys. Med. Biol. **65** (2020) 025001.

[96] S. Gundacker, *Time resolution in scintillator based detectors for positron emission tomography*, PhD thesis, Technische Universität Wien, 2014, CERN-THESIS-2014-034.

[97] A. Kuonen, *Development and characterisation of silicon photomultiplier multichannel arrays for the readout of a large scale scintillating fibre tracker*, PhD thesis, EPFL, 2018, EPFL-THESIS-8842.

[98] S. S. Majos *et al.*, *Noise and radiation damage in silicon photomultipliers exposed to electromagnetic and hadronic radiation*, Nucl. Instrum. Methods Phys. Res. A **602** (2009) 506.

[99] Y. Musienko *et al.*, *Radiation damage studies of multipixel Geiger-mode avalanche photodiodes*, Nucl. Instrum. Methods Phys. Res. A **581** (2007) 433.

[100] C. E. Aalseth *et al.*, *DarkSide-20k: A 20 tonne two-phase LAr TPC for direct dark matter detection at LNGS*, Euro. Phys. J. Plus **133** (2018) 1, arXiv:1707.08145.

[101] M. Capasso *et al.*, *FBK VUV-sensitive Silicon Photomultipliers for cryogenic temperatures*, Nuclear Instruments and Methods in Physics Research Section A: Accelerators, Spectrometers, Detectors and Associated Equipment **982** (2020) 164478.

[102] A. Baldini *et al.*, *The design of the MEG II experiment*, Euro. Phys. J. C **78** (2018) 1, arXiv:1801.04688.

[103] A. Gola, *Status and perspectives of SiPMs*, https://indico.cern.ch/event/1094055/contributions/4974926/attachments/2508774/4312531/2022-09-15%20-%20Alberto%20Gola%20-%20SiPM%20roadmap%20-%20RICH%202022%20-%20v4%20-%20share.pdf, 2022. last accessed: 2023-02-5.

[104] J. Kuraray Co.L̃td. Tokyo. http://kuraraypsf.jp/psf/.

[105] B. D. Leverington, *The LHCb upgrade scintillating fibre tracker*, PoS **213** (2015) 113.

[106] C. D'Ambrosio *et al.*, *Organic scintillators with large Stokes shifts dissolved in polystyrene*, Nucl. Instrum. Methods Phys. Res. A **307** (1991) 430.

[107] M. Deckenhoff, *Scintillating fibre and silicon photomultiplier studies for the LHCb upgrade*, PhD thesis, Technische Universität Dortmund, 2016, CERN-THESIS-2015-318.

[108] C. Joram *et al.*, *Lhcb scintillating fibre tracker engineering design review report: Fibres, mats and modules* , CERN, Geneva, 2015. CERN-LHCb-PUB-2015-008.

[109] T. Colombo *et al.*, *Flit-level InfiniBand network simulations of the DAQ system of the LHCb experiment for Run-3*, IEEE Transactions on Nuclear Science **66** (2019) 1159.

[110] O. G. Girard, G. Haefeli, A. K. Kuonen, and M. E. Stramaglia, *Read-out of irradiated SiPMs attached to short scintillating fibre module*, CERN-LHCb-INT-2017-009, CERN, Geneva, 2017.

[111] LHCb collaboration, *Dark count rate measurement for SciFi - LHCb commissioning 2022*, LHCb-FIGURE-2023-005, CERN, Geneva, 2023.

[112] F. Gargano, *The High Energy cosmic-Radiation Detection (HERD) facility on board the Chinese Space Station: hunting for high-energy cosmic rays*, Proceedings of 37th International Cosmic Ray Conference — PoS(ICRC2021) **395** (2021) 026.

[113] C. Perrina *et al.*, *FIT: the scintillating fiber tracker of the HERD space mission*, **395** 067, 2021.

[114] K. Arndt *et al.*, *Technical design of the phase I Mu3e experiment*, Nucl. Instrum. Methods Phys. Res. A **1014** (2021) 165679.

[115] A. Bravar *et al.*, *Development of the scintillating fiber timing detector for the Mu3e experiment*, `arXiv:2208.09906`.

[116] C. A. Mack, *Field guide to optical lithography*, SPIE Bellingham, 2006.

[117] S. O. Kasap, *Optoelectronics and photonics: principles and practices*, Prentice-Hall, Inc., 2001.

[118] J. M. Pavia, M. Wolf, and E. Charbon, *Measurement and modeling of microlenses fabricated on single-photon avalanche diode arrays for fill factor recovery*, Optics express **22** (2014) 4202.

[119] A. B. Cavalcante, *private communication* , EPFL, 2020.

[120] S. Agostinelli *et al.*, *GEANT4—a simulation toolkit*, Nucl. Instrum. Methods Phys. Res. A **506** (2003) 250.

[121] J. Allison *et al.*, *Geant4 developments and applications*, IEEE Transactions on nuclear science **53** (2006) 270.

[122] M. E. Stragmalia, *private communication* , EPFL, 2019.

[123] *Astrolumina QHY5L-II*, https://www.astrolumina.de/kamerasysteme/alccd-qhy/alccd-qhy-5l-ii-c.php, 2023. last access: 2023-01-29.

[124] S. Nieswand, *Measurement of the exit characteristics of light from optical multimode plastic fibres* , Master thesis, RWTH Aachen U., 2014. CERN-THESIS-2014-414.

[125] *Microlens simulation for LHCb SciFi SiPMs*, https://gitlab.cern.ch/ctrippl/microlenssimulation.git, 2023.

[126] Z. Majercik, in *Ray tracing gems II: next generation real-time rendering with DXR, Vulkan, and OptiX*, pp. 109–114, Apress, Berkeley, CA, 2021.

[127] Centre Suisse d'Electronique et de Microtechnique, Muttenz/Basel, Switzerland. https://www.csem.ch/Home.

[128] *Zemax OpticStudio*, https://www.zemax.com/pages/opticstudio, 2023. last access: 2023-04-11.

[129] C. Piemonte *et al.*, *Performance of NUV-HD silicon photomultiplier technology*, IEEE Transactions on Electron Devices **63** (2016) 1111.

[130] G. Zappalà *et al.*, *Set-up and methods for SiPM photo-detection efficiency measurements*, Journal of Instrumentation **11** (2016) P08014.

[131] H. Ottevaere *et al.*, *Comparing glass and plastic refractive microlenses fabricated with different technologies*, Journal of Optics A: Pure and Applied Optics **8** (2006) S407.

[132] F. Zanella, *private communication* , CSEM, 2019.

[133] F. Zanella, *private communication* , CSEM, 2023.

[134] F. Zanella, *Technical drawing* , CSEM, 2020.

[135] J. Anders *et al.*, *A facility for radiation hardness studies based on the bern medical cyclotron*, `arXiv:1803.01939`.

[136] M. Berger *et al.*, *Stopping-power and range tables for electrons, protons and helium ions*, https://www.nist.gov/pml/stopping-power-range-tables-electrons-protons-and-helium-ions. last accessed: 2023-02-06.

[137] F. Zanella, *private communication* , CSEM, 2022.

[138] M. G. Bagliesi *et al.*, *A custom front-end ASIC for the readout and timing of 64 SiPM photosensors*, Nucl. Phys. B Proc. Suppl. **215** (2011) 344.

[139] Y. Tao, A. Rajapakse, and A. Erickson, *Advanced antireflection for back-illuminated silicon photomultipliers to detect faint light*, Scientific Reports **12** (2022) 1.

[140] T. Harion *et al.*, *STiC—a mixed mode silicon photomultiplier readout ASIC for time-of-flight applications*, Journal of Instrumentation **9** (2014) C02003.

[141] H. Chen *et al.*, *A dedicated readout ASIC for time-of-flight positron emission tomography using silicon photomultiplier (SiPM)*, in *2014 IEEE nuclear science symposium and medical imaging conference (Nss/Mic)*, 1–5, IEEE, 2014.

[142] R. Diener *et al.*, *The DESY II test beam facility*, Nucl. Instrum. Methods Phys. Res. A **922** (2019) 265.

[143] M. Paterno, *Calculating efficiencies and their uncertainties*, FERMILAB-TM-2286-CD (2004) .

[144] G. Häfeli, *private communication* , EPFL, 2023.

[145] J. M. Frieden, *Time calibration for the SciFi Tracker at SND@LHC using DESY testbeam data* , Master project, EPFL, 2020. http://infoscience.epfl.ch/record/301960?&ln=en.

[146] G. Räuber, *Time calibration of the SciFi tracker based on track time information* , Master project, EPFL, 2020. http://infoscience.epfl.ch/record/301961?&ln=en.

[147] T. Wang *et al.*, *Characterization of two SiPM arrays from Hamamatsu and Onsemi for liquid argon detector*, `arXiv:2210.15970`.

[148] A. Falcone, *The DUNE Photon Detection System*, PoS **NuFact2021** (2022) 191.

[149] G. Häfeli and F. Bernard, *Technical design study* , EPFL, 2022.

[150] A. R. Altamura *et al.*, *Characterization of Silicon Photomultipliers after proton irradiation up to* $10^{14}\,n_{eq}/cm^2$, Nucl. Instrum. Methods Phys. Res. A **1040** (2022) 167284.

[151] F. Acerbi *et al.*, *Radiation damage effects of protons and X-rays on silicon photomultipliers*, Nucl. Instrum. Methods Phys. Res. A **1047** (2023) 167791.

[152] S. Merzi, *private communication* , FBK, 2023.

[153] S. Merzi and L. Niggli, *Functional characterization report (private)* , FBK, 2023.

Carina Trippl, MSc

Curriculum Vitae

+41 78 321 87 88
carina.trippl@epfl.ch

PERSONAL INFORMATION

Full Name	Carina Antonia Trippl
Date of Birth	16th September 1993
Nationality	Austria
Current Residential Address	Boulevard de Charmontey 3 1800 Vevey Switzerland
ORCID ID	0000-0003-3664-1240

EDUCATION

Feb. 2019 - now — **Doctor of Philosophy (PhD)** in Physics
École Polytechnique Fédérale de Lausanne, Switzerland

- Doctoral Thesis: *Development of microlens-enhanced SiPMs for a radiation-hard scintillating fibre tracker at LHCb*
  Supervisor: Prof. Olivier Schneider
  Co-Supervisor: Dr. Guido Häfeli

Apr. 2016 - Oct. 2018 — **Master of Science (MSc)** in Physics
University of Vienna, Austria

- Master's Thesis: *Preparation of a High-precision X-ray Detector for Kaonic Atom Measurements at J-PARC and DAΦNE*
  Supervisor: Dr. Johann Zmeskal

Oct. 2012 - Apr. 2016 — **Bachelor of Science (BSc)** in Physics
University of Vienna, Austria

EMPLOYMENT HISTORY

Feb. 2019- now — **École Polytechnique Fédérale de Lausanne**
PhD student

- Prototyping microlens enhanced silicon photomultipliers to enhance light collection efficiency for the LHCb scintillating fibre tracker
- Participation in test beam campaign (Oct 2019) of scintillating fibre tracker with timing information
- Teaching assistant for courses at bachelor and master level as well as specialisation project assistant for master students

Nov. 2021 - Jan. 2022 **Fondazione Bruno Kessler**
Guest PhD Student

- Characterisation of novel silicon photomultiplier technologies for the LHCb scintillating fibre tracker

June 2017- Aug. 2018 **Stefan Meyer Institute for Subatomic Physics**
Master student

- Performed test measurements of Silicon Drift Detectors (SDDs)
- Attended kaonic helium E62 beam time at J-PARC and carried out the SDD stability analysis of the E62 data

Aug. 2016 **Stefan Meyer Institute for Subatomic Physics**
Scientific Internship: Silicon Drift Detector test measurements

Oct. 2015- Feb. 2016 **University of Vienna**
Tutor for "Introduction to Computational Methods in Physics"

CONFERENCES AND WORKSHOPS

Feb. 2022 **Vienna Conference on Instrumentation (VCI)**
Vienna University of Technology, Vienna, Austria
Recorded Presentation: "Microlens-enhanced silicon photomultiplier arrays for LHCb SciFi Tracker Upgrade Ib"

- Award for **best recorded presentation**

Aug. - Sep. 2021 **Joint Annual Meeting** of the Swiss and Austrian Physical Society
Swiss and Austrian Physical Society, Innsbruck, Austria
Oral Contribution: "Micro-lens enhanced SiPMs for the LHCb SciFi Tracker"

June 2021 **CHIPP Plenary** Annual meeting
CHIPP (Swiss Institute of Particle Physics), Spiez, Switzerland
Invited Flash Talk: "LHCb Detector Upgrade"
Poster Contribution: "Micro-lens-enhanced SiPMs for future LHCb SciFi Tracker Upgrades"

Oct. 2019 **SiPM Workshop:** from fundamental research to industrial applications
Università di Bari, Bari, Italy
Poster Contribution: "Characterisation of SiPMs for the LHCb Scintillating Fibre Tracker"

Sep. 2018 **68th Annual Meeting** of the Austrian Physical Society
Austrian Physical Society, Graz, Austria
Oral Contribution: *"A New High-precision Silicon Drift Detector System for Kaonic Atom Measurements at J-PARC and DAFNE"*

PROFESSIONAL AND PERSONAL ADVANCEMENT

June 2022 Attendance of **International School of Trigger and Data Acquisition**

May 2022 Attendance of **Thematic CERN School of Computation: Scientific Software for Heterogeneous Architectures**

July 2021 Attendance of **Seventh Machine Learning in High Energy Physics Summer School**

Mar. 2021 Successful completion of **TinyML: Fundamentals of TinyML** (verified certificate) on edX

Oct. 2020 Participation of **HEP C++ Course and Hands-on Training** organised by CERN

2010-2011 **Academic year abroad** at *Weymouth College*, UK
successfully concluded AS-levels in Mathematics and Physics

AWARDS AND FELLOWSHIPS

2022 Receiver of the **SNSF postdoc.mobility** fellowship grant (start date: June 2023)

Feb. 2022 Winner of NIMA junior researcher award for **best recorded presentation** at the Vienna Conference of Instrumentation (VCI)

OUTREACH ACTIVITIES

2022-now Member of the manager team of the official **LHCb Instragram account**

July 2022 Member of the LHCb team for the CERN live event **"Join us for the first collisions for physics at 13.6 TeV!"**

2019-2022 Participation in **outreach activities** at CERN

Apr. 2018 Participation in the **Long Night of Research** in Vienna

2017-2018 Participation in **outreach projects** for women and children in Vienna

PUBLICATIONS

- more than 100 publications as member of the LHCb collaboration

Proceedings

- "Microlens-enhanced silicon photomultiplier arrays for LHCb SciFi Tracker Upgrade 1b **C. Trippl**, G. Haefeli, O. Schneider and E. Zaffaroni, NIMA **1040** (2022) 167216
- "A New Silicon Drift Detector for Kaonic Deuterium Measurements" C. Trippl and J. Zmeskal, EPJ Web of Conferences **181** (2018) 01035
- "Silicon Drift Detector Tests for Kaonic Atom Measurements" C Trippl *et al*, J. Phys.: Conf. Ser. **1138** (2018) 012013

PERSONAL SKILLS

- **Languages:**

German:	Native speaker						
English:	Speaking	●●●●◐	Reading	●●●●●	Listening	●●●●●	Writing	●●●●◐
French:	Speaking	●●◐○○	Reading	●●●◐○	Listening	●●●○○	Writing	●●◐○○

- **Hardware experience:**
  I am specialised in the characterisation and usage of **silicon photomultipliers** and **scintillating fibres**, and I have acquired experience with other common particle detector technologies (e.g. **SDDs**, **PMTs**, **PIN diodes**, etc.). Furthermore, I am proficient with different instrumentation technologies following the major electronics standards (**NIM, CAMAC** and **VME**), in **triggering** techniques and in the **read-out of analogue and digital** signals.

- **Programming experience:**
  I am fluent in the use of the most common programming languages used in scientific research (**C++**, **Python**, etc.). Moreover, I am competent in the use of several different project-specific frameworks and software packages, i.e. data analysis (**ROOT**, **NumPy**), but also for detector simulation (**GEANT-4**), machine learning (**Keras**, **TensorFlow**), web publishing (**WordPress**) and text editing (**Latex**). I can install and maintain **linux-based** systems.